5. TESTING

5.1 Test Planning

The basic objectives of the PCCV test were specified by NUPEC in the Master Project Plan [34]. The stated objective of this plan was to… "investigate the ultimate behavior of PCCV under pressure beyond the design basis accident and to prove the pressure retaining capacity of PCCV." NUPEC originally specified a series of five tests, illustrated in Figure 5.1: 1) trial pressurization to 0.4 kg_f/cm^2 (5.7 psig or 0.1 P_d), 2) structural integrity and integrated leak rate tests to 4.5 and 3.6 kg_f/cm^2 (64.1 and 51.2 psig or 1.125 and 0.9 P_d), respectively, 3) two design pressure tests to 4.0 kg_f/cm^2 (57 psig or 1.0 P_d), and 4) a Limit State Test (LST) terminating with excessive leakage or structural failure.

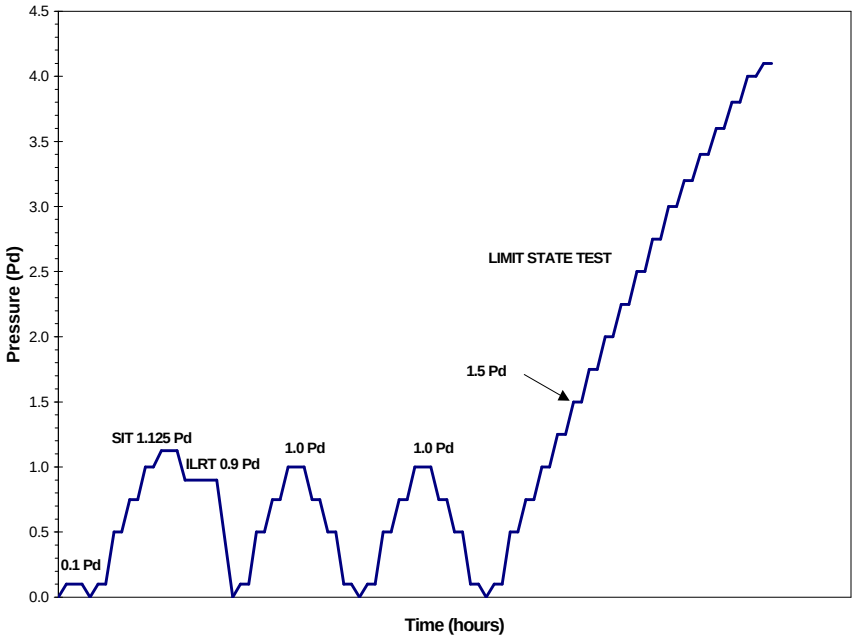

Figure 5.1 Original Pressurization and Depressurization Sequence [34]

After extensive discussions between NUPEC, the NRC and SNL, a detailed Test Plan [35] was developed by SNL to describe the conduct of the PCCV model's pressurization tests. Additional procedures that addressed the safe conduct of the tests were defined in the Operating Procedure [36]. The Test Plan includes:

- procedures to be conducted prior to tests to assure that all systems are ready;
- a list of test personnel required to conduct the tests and an outline of functions and checklists assigned to each person;
- procedures to be followed during the tests, including the general test philosophy;
- procedures to be conducted after pressure tests are completed.

Detailed checklists were prepared to ensure that all test operations were conducted as planned and completed in the appropriate sequence. Detailed procedural logs, stored in the project files, were generated to document the conduct of each test. A summary of the test plan is included in this chapter.

A final series of three tests were agreed upon. These tests are defined as follows and are illustrated in Figure 5.2.

1. A leak check and System Functionality Test (SFT) at 0.5 P_d (2.0 kg_f/cm^2 or 28.4 psig)

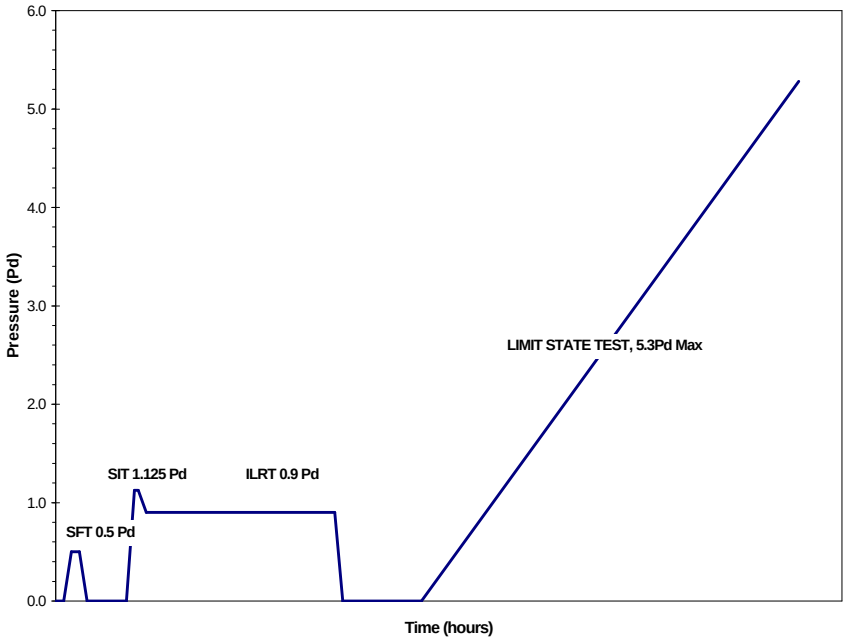

Figure 5.2 Final Pressurization Plan

2. A Structural Integrity Test (SIT) at 1.125 P_d followed by an Integrated Leak Rate Test (ILRT) at 0.9 P_d
3. An Limit State Test (LST) to the static pressure capacity of the PCCV model (or the pressurization system, whichever comes first)

A fourth test was added to the test program after the conclusion of the LST. After careful evaluation of the LST results, NUPEC, the NRC, SNL, and their technical advisors concluded that not all of the program's objectives were met after the LST. SNL was tasked with designing and conducting a test that would allow the PCCV model to be pressurized beyond the level reached during the LST in an attempt to observe greater inelastic response of the model and, hopefully, generate a structural failure mode. This Structural Failure Mode Test (SFMT) is described in Section 5.2.4.

5.1.1 Pressurization System Design and Operation

The pressurization system for the PCCV model test consisted of a pressure source, a valve gallery (consisting of several valves, a flow meter, and several sensors) used to control the flow of nitrogen, a programmable logic controller (PLC), control computer, and high pressure piping which interconnects all the components. A schematic of the pressurization system is shown in Figure 5.3

For the SFT, SIT/ILRT, and SFMT, the pressure source consisted of a pressurized nitrogen tube trailer. The trailer was located adjacent to the PCCV model, next to the valve gallery with a short flexible hose connecting them. For the LST, the pressure source consisted of a truck with liquid nitrogen that was gasified and regulated to a constant pressure and temperature. This source was located more than 600 m (2000') away from the PCCV model for safety reasons, near Building 9950. The pressurized nitrogen gas was piped aboveground onto the CTTF site and into the valve gallery.

In addition to the temperature being controlled at the source location during the pressure testing, the gas was heated in the piping prior to entering the PCCV model. These heaters helped increase the temperature of the gas prior to entering the PCCV model. Several additional heaters were located inside the model to help maintain temperatures to within ±5 degree C of the average ambient temperature (~15° C) outside the PCCV model.

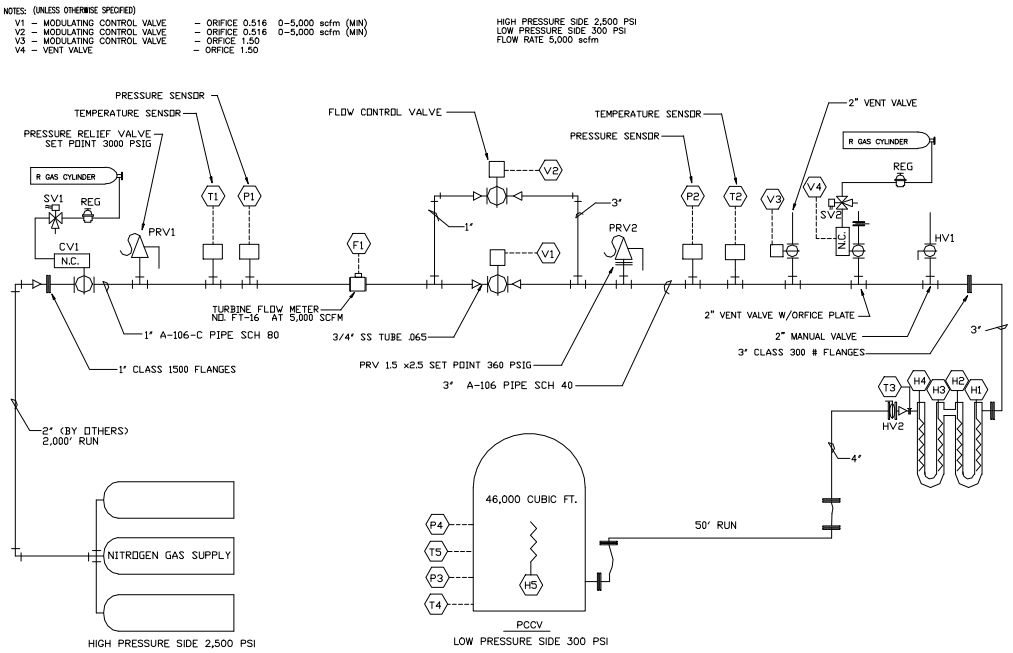

Figure 5.3 Pressurization System Schematic

The pressurization system was controlled by the PLC, which was located on the valve gallery skid next to the PCCV model. Communication with the PLC was performed by the control computer located in Building 9950. A more detailed description of the entire pressurization system is provided in the PCCV Pressurization System Data Package [37].

The entire pressurization system was designed and fabricated by an outside contractor (Rupert Plumbing and Heating Company, Inc., Albuquerque, NM). Initial testing of the system (primarily the valve gallery and heaters) was performed by the contractor prior to delivery to the CTTF site. After the system was installed at the site, the system was tested again before connecting to the PCCV model and conducting the pressure tests of the model.

The system tests performed by the contractor were approved by SNL personnel and encompassed all possible conditions the system might have to deal with during both the low- and high-pressure testing. These system tests checked all wiring, valve functionality, instrument functionality, and the control hardware and software.

After the system was installed and tested, the piping into the PCCV model was hooked up. All pressure lines connected to the valve gallery and the PCCV model were clean and dry before they were connected. Before the flex hose and flange were connected to the PCCV model, the line was "blown out" to clean it. The pressure source line up to the valve gallery was also blown out prior to the final hook-up.

5.2 Test Operations

The over-pressurization tests of the PCCV model were conducted at the CTTF-W, shown in Figure 1.3.

Building 9950, an ancillary facility for the test site (shown in the background in Figure 2.11), was the headquarters for conducting the pressure tests. It housed the control room and the observation room. During the test, key project members were inside the control room to execute the test plan and monitor the response of the model. Visitors observed the test progress and received periodic information on test status in the observation room.

The basic test team for each test is shown in Figure 5.4. The test team was only fully staffed for the LST and the SFMT. Test staffing for prestressing and the low-pressure tests is shown in Table 5.1.

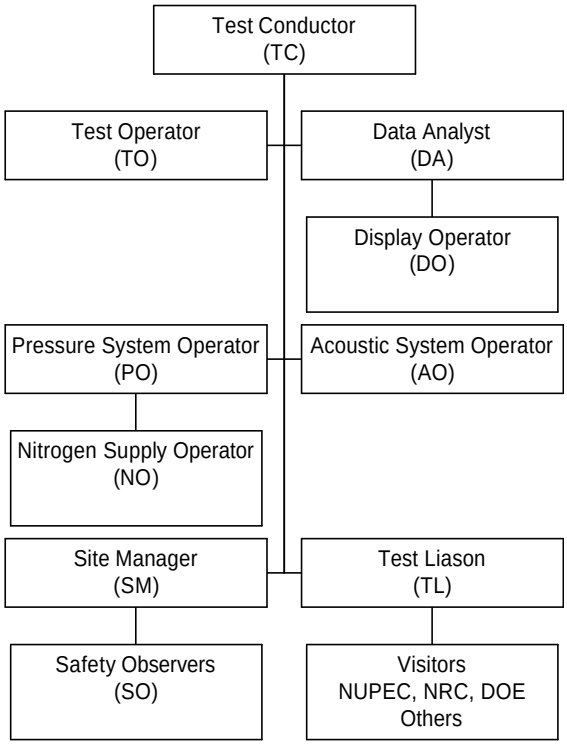

Figure 5.4 PCCV Test Organization

Table 5.1 PCCV Test Personnel Matrix

Position	Prestressing	SFT	SIT/ILRT	LST	SFMT
Test Conductor	X*	X	X	X	X
Test Operator	X	X	X	X	X
Data Analyst				X	X
Display Operator			X	X	X
Pressure System Operator		X	X	X	X
Acoustic System Operator	X	X	X	X	X
Site Manager	X	X	X	X	X
Safety Observers			X	X	X
Nitrogen Supply Operators		X	X	X	X
Test Liaison			X	X	
Visitors			X	X	X

*Part-time

5.2.1 System Functionality Test

The system functionality test and leak check was designed to verify the functionality of all the systems (instrumentation, data aquisition, pressurization, etc.) and the initial leak-tightness of the PCCV model (especially the sealing of the penetrations) prior to the performance of the pressure tests. Controlled leak tests were included to determine the accuracy of the leak detection instrumentation during the ILRT and LST.

The SFT was conducted beginning approximately 9:00 AM, July 18, 2000. The model was pressurized using nitrogen to 0.5 P_d (0.2 MPa or 28.4 psig) in three increments holding pressure for one hour or longer at each step, depending on the duration needed to perform all system functionality and leak checks. The model was then isolated and a leak rate check was performed by monitoring the model pressure and temperature for approximately 18 hours. After 18 hours, the calculated leak rate was 0.15% mass/day, which confirmed that the model was leak-tight. After the model leak rate check, the model was allowed to depressurize through a pair of orifice plates calibrated to leak rates of 1% and 10% mass/day to perform a calibration test on the leak rate measurement instrumentation. The calculated leak rates for each test were 0.87% and 7.86%, respectively, indicating that the leak rate instrumentation accurately detected a leak of 1% mass per day, which is the goal specified for the ILRT. The SFT was concluded on July 20 by opening the vent valve, allowing the model to depressurize. The SFT pressure time history and leak rates are shown in Figures 5.5 and 5.6.

5.2.2 Structural Integrity Test and Integrated Leak Rate Test

The SIT and the ILRT were conducted on September 12-14, 2000 as a combined test, with the ILRT following immediately after the SIT. The SIT/ILRT reproduced the preoperational tests conducted at the prototype plant and allows for a comparison of the model's elastic response characteristics and leak behavior with the prototype and pretest analyses. The pressure and average temperature time histories measured during the test are shown in Figure 5.7.

5.2.2.1 Structural Integrity Test

The SIT followed the procedures specified by Japanese Standard JEAC 4203-1994 [38] and the ASME Boiler and Pressure Vessel Code, Section III, Division 2, Article CC-6000, " Structural Integrity Test of Concrete Containments." [9]

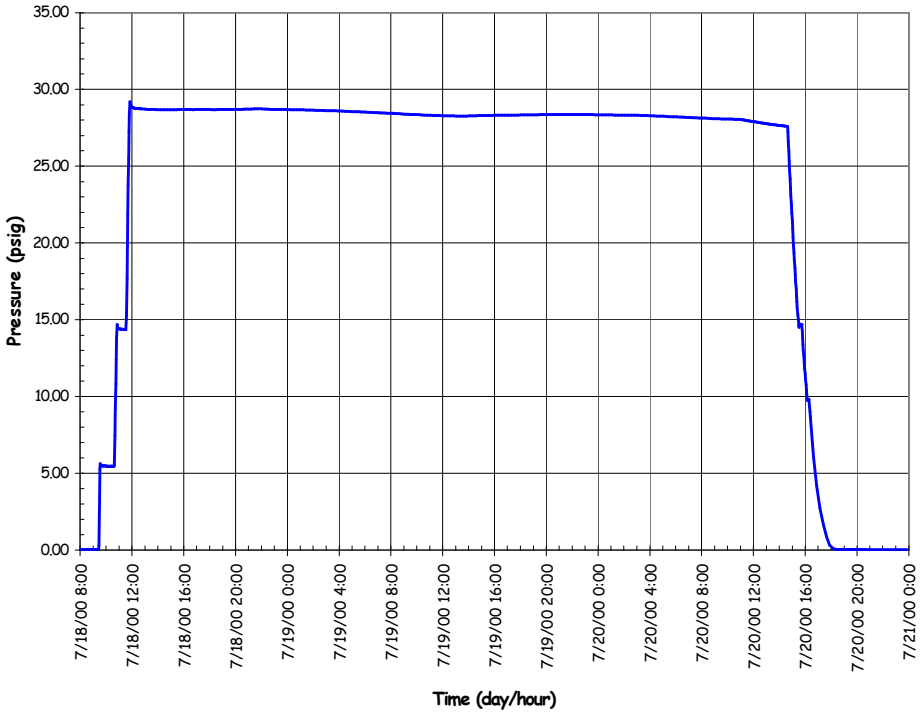

Figure 5.5 System Functionality Test Pressure Time History

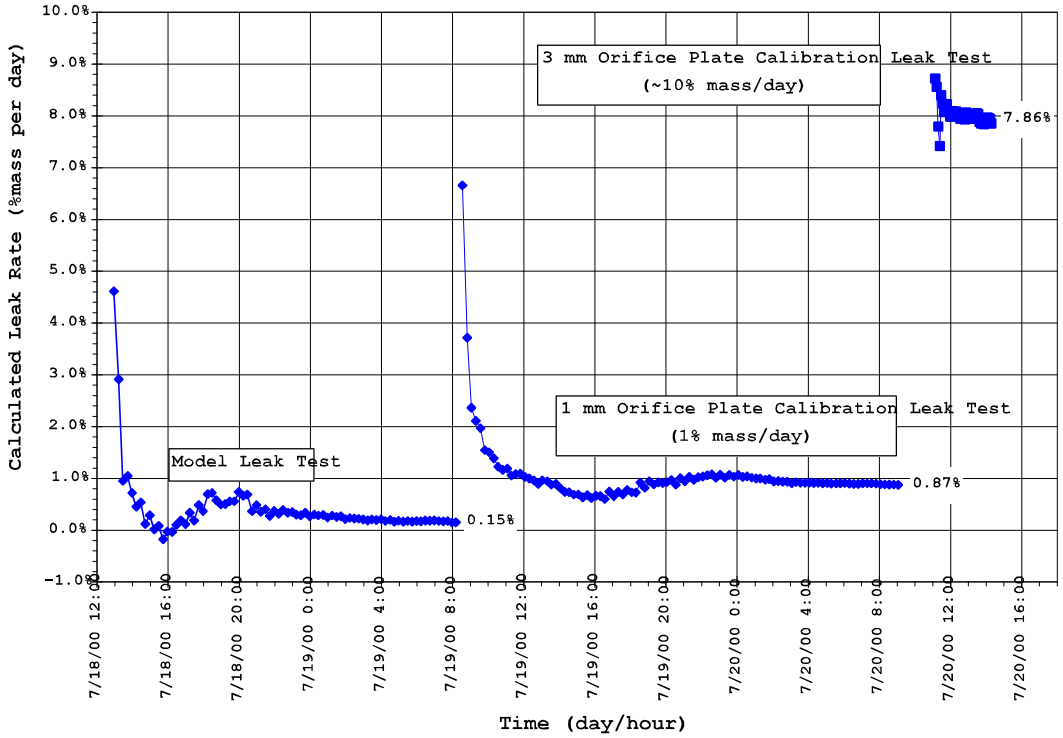

Figure 5.6 System Functionality Test Leak Rates

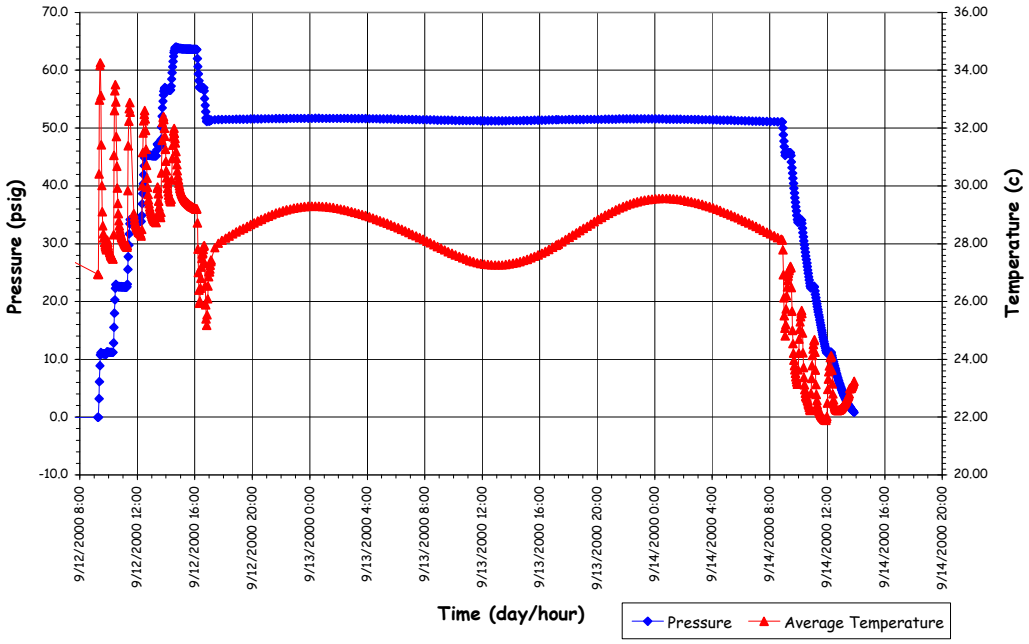

Figure 5.7 Structural Integrity and ILRT Pressure and Temperature Time Histories

Per MITI Code 501, Article 104 [39], the SIT test pressure, P_{SIT}, was 1.125 P_d (0.44 MPa or 64 psig). The PCCV model was pressurized in five equal increments at a rate of 20% of the test pressure per hour. (CC-6110 requires pressurization to 1.5 P_d.) Per CC-6340, the response of the model was recorded at each pressure step (including 0 P_d). Data of Record (DOR) was recorded when the following stability criterion was achieved:

$$\frac{Q_t - Q_{t-\Delta t}}{Q_{t-\Delta t}} \leq 0.02 \tag{5.1}$$

where Q_t and $Q_{t-\Delta t}$ are the data at the current and the previous time interval, respectively. The next pressure increment followed only after this criterion was satisfied or the total step duration reached one hour.

All active gages in or on the model were recorded at each step. The locations of the gages were selected to allow for direct comparison of the PCCV model response to the prototype at the SIT pressure in addition to the primary objective of monitoring the response of the model to ultimate pressure. Table 5.2 summarizes the ASME code requirements for SIT measurements.

Table 5.2 Summary of ASME B&PV Code SIT Instrumentation Requirements

	Measurements	Accuracy/Range	Pressure	Acceptance Criteria
Cracking	**CC-6350** Cracks > 0.01"x 6" @ specified locations	**CC-6225** >0.005" @ 0.003"	**CC-6350** Before test @P_{SIT} After test	**CC-6420** Review by Designer
Strains	**CC-6370: (Concrete Strains)** @Wall/Slab @E/H @Shell Discontinuites @Restraints @Steel/Concrete Trans.	**CC-6224** ±5%ε_{max} or 10με Gage Length > 4"	**CC-6371** 1. Baseline-Continuously for 24 hrs prior to test **CC-6340** 2. @P_0 (Atmospheric press.) 3. During pressurization @ 20%P_{SIT} 40%P_{SIT} 60%P_{SIT} 80%P_{SIT} 100%P_{SIT} 4. @PSIT + 1 hour 5. During depressurization @ 80%P_{SIT} 60%P_{SIT} 40%P_{SIT} 20%P_{SIT} @P_0	**CC-6410** (a) No rebar yielding (b) No visible liner or concrete damage
Displacements	**CC-6361:** δ_R@20%H & 0°, 90°, 180°, 270° δ_R@40%H & 0°, 90°, 180°, 270° δ_R@60%H & 0°, 90°, 180°, 270° δ_R@80%H & 0°, 90°, 180°, 270° δ_R@100%H & 0°, 90°, 180°, 270° δ_R@E/H (12 points) δ_V@ Springline & 0°, 90°, 180°, 270° δ_V@ Apex δ_V@ two pts. Bet. Apex & Springline	**CC-6223** ±5%δ_{max} or 0.01"		(c-2) Residual displacements: @ Pts of Max. δ_R & δ_V : δ_{res} < 20% δ_{max}* @ P_{SIT} + 0.01" (*measured or predicted) Avg. δ_R @ each elevation: δ_{res} < 20% δ_{max}* @ P_{SIT} + 0.01"
Temperature	**CC-6380** Concrete @ Specified locations for Strain Correction Gas @ Interior & Exterior	**CC-6226** ±2°F Range: Expected temp.		
Pressure		**CC-6222:** ±2%P_{SIT} Range < 4 P_{SIT}		

In general, the model instrumentation satisfied all of the requirements summarized in Table 5.2 with the following exceptions or modifications.

- The entire surface of the cylinder was mapped for cracks prior to the test; however, crack widths were not measured. No crack mapping was performed during the SIT. After the SIT, additional cracks within selected areas of the cylinder wall were identified but the widths were not measured. The crack map grid is shown in Figure 5.8

- Model strains were measured primarily using the gages mounted directly to the rebar and liner. Only a limited number of concrete strains were measured directly.

- Displacements were measured at all specified locations with the exception of the points around the largest penetration (i.e. the E/H)

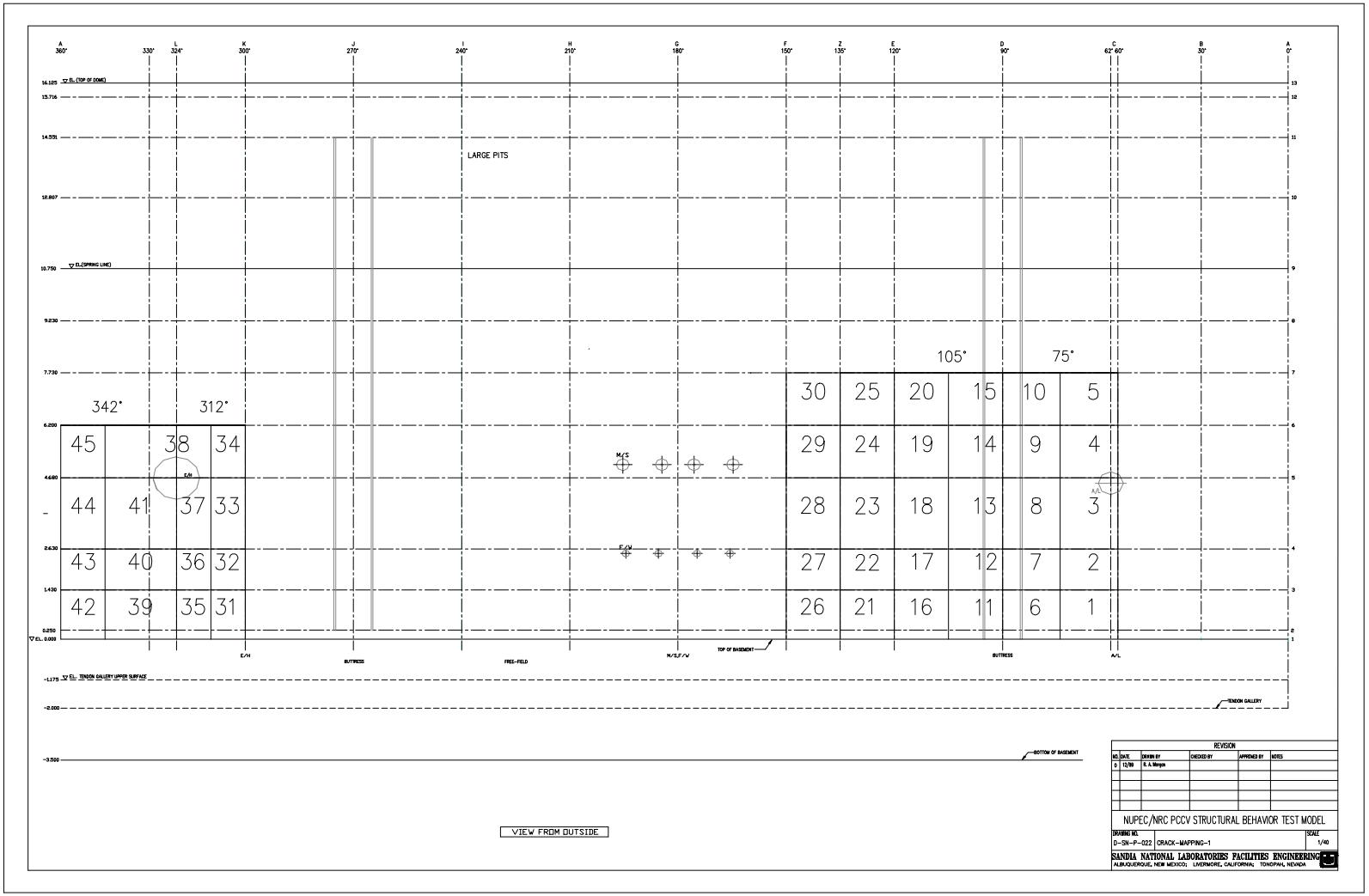

Figure 5.8 Concrete Crack Map Grid

After the SIT pressure was maintained for the required minimum of one hour per CC-6320, the PCCV model was depressurized to the ILRT pressure. First, the model was depressurized to Pd, for comparison with the pressurization phase, before depressurizing to the ILRT pressure (0.9Pd).

The temperature inside the model was specified to be maintained at approximately 25 °C (77 °F) during the test with a maximum range of 10 °C to 38 °C (50 °F to 100 °F). The average temperature during the SIT, recorded by the RTDs, was closer to 30 °C (86 °F). The ambient air temperature outside the model was measured near the base of the model.

5.2.2.2 Integrated Leak Rate Test

The ILRT requirements for Japanese containments are specified in JEAC 4203-1994 [38]. The ILRT requirements for U.S. containment vessels are specified in 10CFR50, Appendix J "Primary Reactor Containment Leakage Testing for Water-Cooled Power Reactors," [40] which references the tests procedures in American National Standards ANSI/ANS N45.2-1974 "Leakage Rate Testing of Containment Structures for Nuclear Reactors [41] and ANSI/ANS N56.9-1987 "Containment System Leakage Testing Requirements." [42]

The ILRT for the PCCV model was a hybrid of these procedures. The ILRT pressure, P_{ILRT} , was 0.9 Pd (0.35 MPa or 51.2 psig) based on JEAC 4203 and the Absolute Method for a Type A Test per ANSI/ANS N56.9 (Section 5.0) was followed. After depressurizing from the P_{SIT} to P_{ILRT}, the model was held at P_{ILRT} for approximately one hour to allow the model atmosphere to stabilize before the start of the leakage rate test. The ILRT commenced after all stabilization criteria were achieved and the duration of the test was "sufficient to enable adequate data to be accumulated and statistically analyzed so that a leakage rate … can be accurately determined" but no less than 24 hours. Data was collected at least once every hour. The measured leakage rate at P_{ILRT}, L_{tm}, was determined using both the (a) total time analysis and (b) point-to-point analysis techniques. The nominal atmospheric pressure at the elevation of the test site (verified by checking the Sandia Photovoltaics Weather Station reading) was used for leak rate calculations. The calculated leak rate after 24 hours at 0.9 P_d, was 0.059% mass/day.

After the ILRT was completed, the model was initially depressurized by venting through the 1mm orifice plate, calibrated for a leak rate of 1% mass/day. After approximately 16 hours, a stable leak rate of 0.996% mass per day was calculated, again confirming the accuracy of the leak rate instrumentation.

The calculated leak rates during and after the ILRT are shown in Figure 5.9.

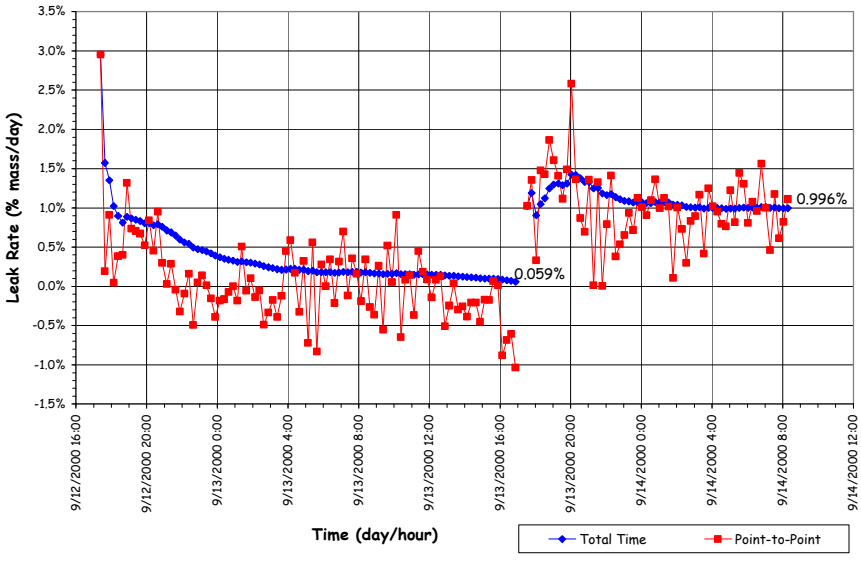

Figure 5.9 Integrated Leak Rate Test Leak Rates

Per JEAC 4203, the maximum leak rate at the ILRT pressure should be less than 0.1% mass/day. Similarly, per 10 CFR 50, the specified maximum allowable leak rate, L_a, at the design accident pressure, P_d, for the prototype containment is 0.1% mass/day. The maximum leak rate at the ILRT pressure level, L_t, is

$$L_t = L_a (P_{ILRT}/P_d) = 0.09\% \text{ mass/day}$$

Normally, the measured leak rate, L_{tm}, should be less than 0.75Lt (0.07% mass/day). For the PCCV model, this translates into measuring a change in pressure of approximately 0.001 kg_f/cm^2 (0.02 psi), which is beyond the capability of the instrumentation to resolve. While the calculated leak rates are within the limits specified in the standards, the accuracy of these leak rate estimates is questionable. Using the instruments selected for the high pressure test, however, the PCCV model exhibited a leak rate which was less than 1% mass/day, which corresponds to a pressure drop of 0.004 MPa (0.6 psi) over 24 hours.

While holding at the ILRT pressure, a limited amount of crack mapping was performed. This was accomplished by tracing all new cracks in predetermined areas and taking still photos of these areas. Cracks in the area to the left of the E/H prior to the SIT were traced in black and are shown in Figure 5.10. New cracks, traced in blue during the ILRT, are shown in Figure 5.11. Cracks widths were not measured.

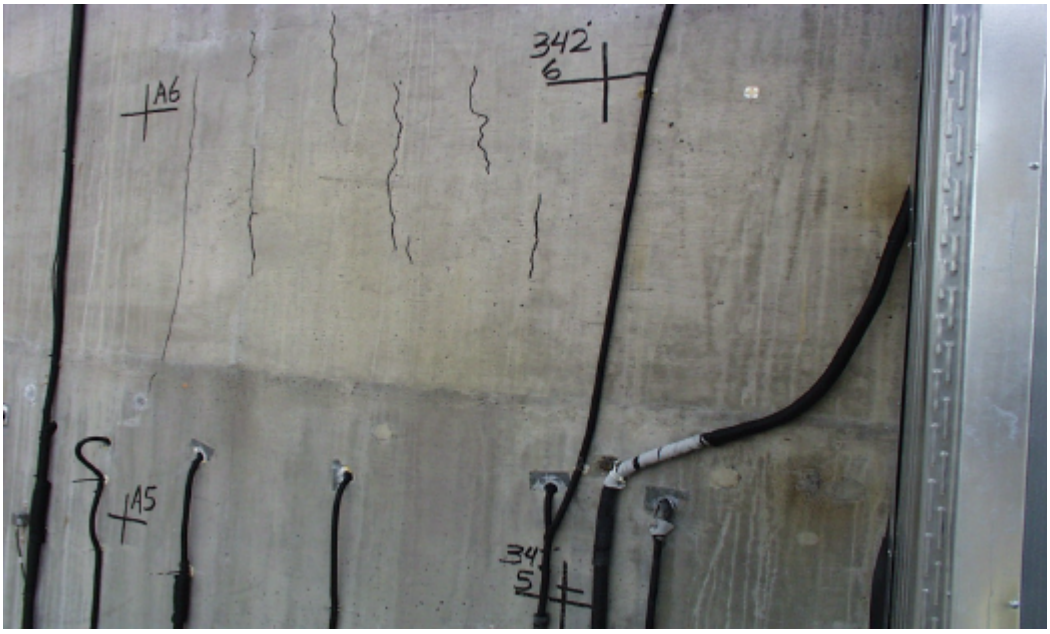

Figure 5.10 Pre-SIT Cracks at Azimuth. 350 degrees, Elev. 4680 to 6200 (Grid 45)

Model response data was also recorded during and after the SIT/ILRT. Figures 5.12 and 5.13 show the radial and vertical displacement of the model as a function of time.

The initial displacements represent the net effect of prestressing, creep, shrinkage, etc. from the 'zero' reading in March to the start of the SIT in September. The cyclic response during the ILRT is an indication of the model's response to variation in ambient temperature and direct heating.

After the leak rate calibration, the PCCV model was depressurized at approximately the same rate and increments as the initial pressurization phase to compare the responses at the same pressure levels.

An exclusion zone was established for the SIT, consisting of a circular area with radius of 600 m (2,000'), centered at the PCCV model. The exclusion zone, as shown in Figure 5.14, was marked, and signs were posted to identify this area. The safety observers monitored the exclusion zone at all times during the test to make sure that no intruder entered this area. No exclusion zone was required for the ILRT because the model pressure was below the design pressure (0.9Pd).

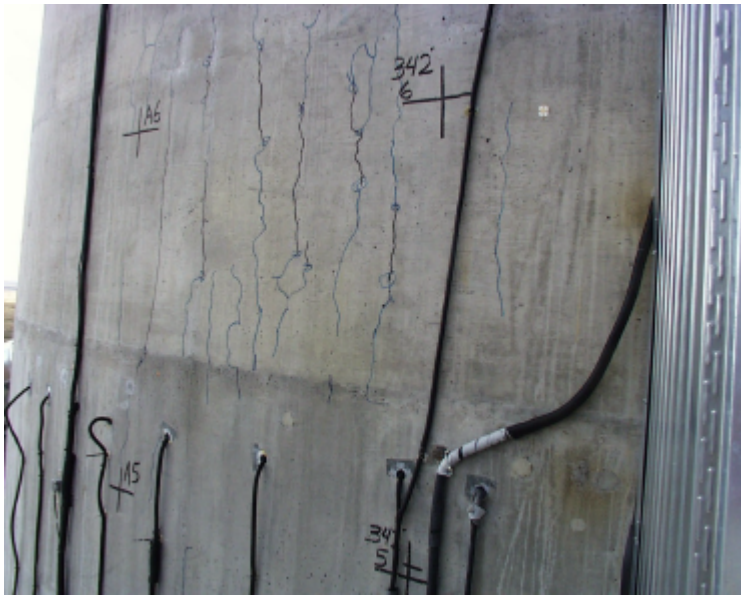

Figure 5.11 Post-SIT Cracks at Azimuth. 350 degrees, Elev. 4680 to 6200 (Grid 45)

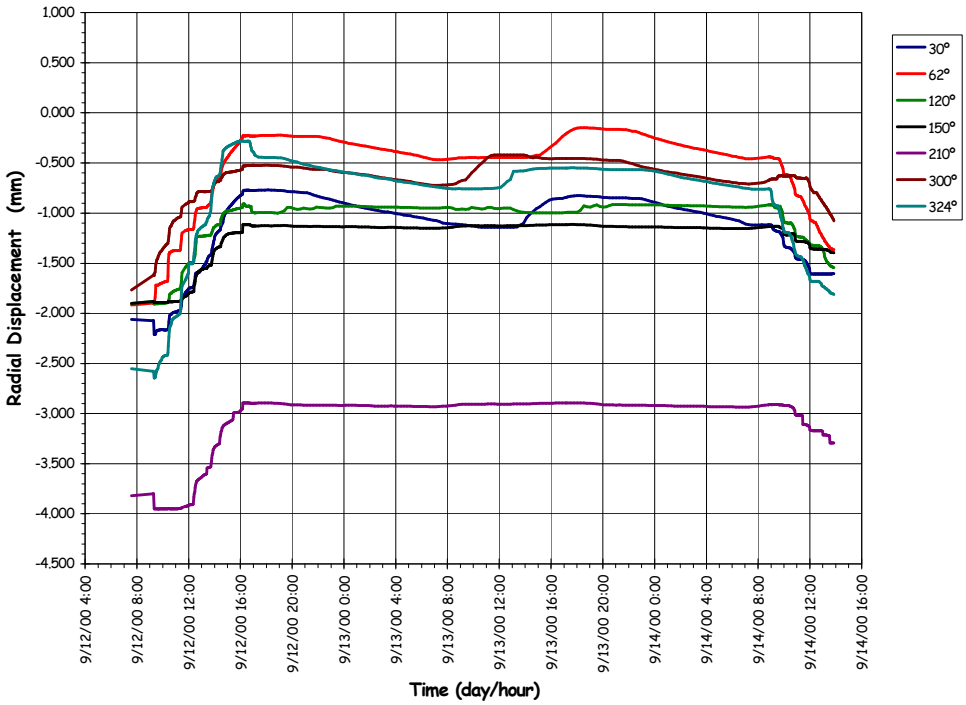

Figure 5.12 SIT/ILRT Radial Displacements at Cylinder Midheight (Elev. 4680)

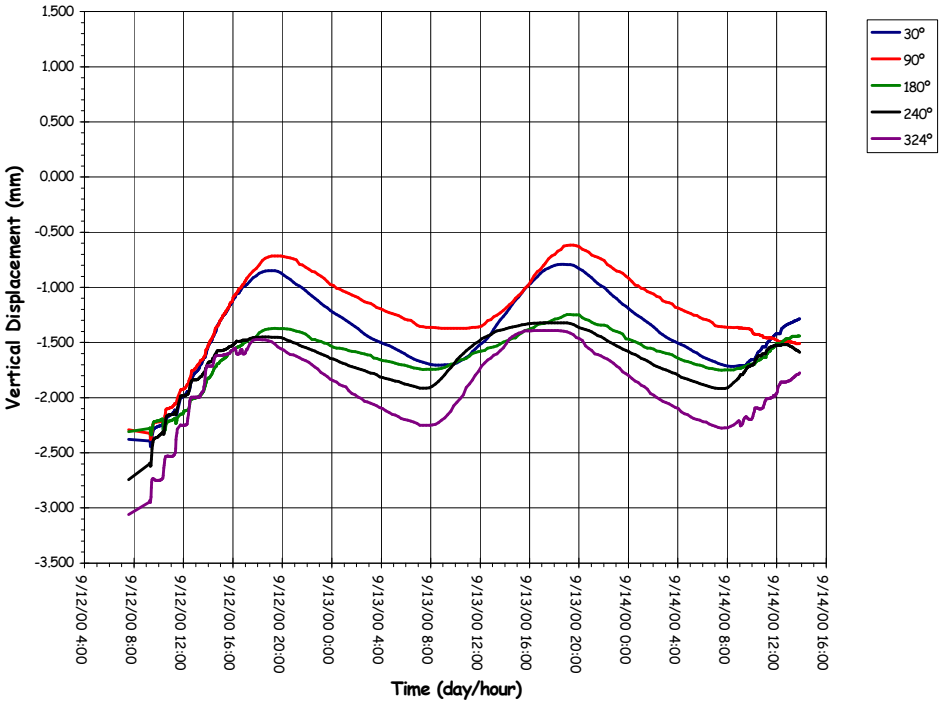

Figure 5.13 SIT/ILRT Vertical Displacements at Springline (Elev. 10750)

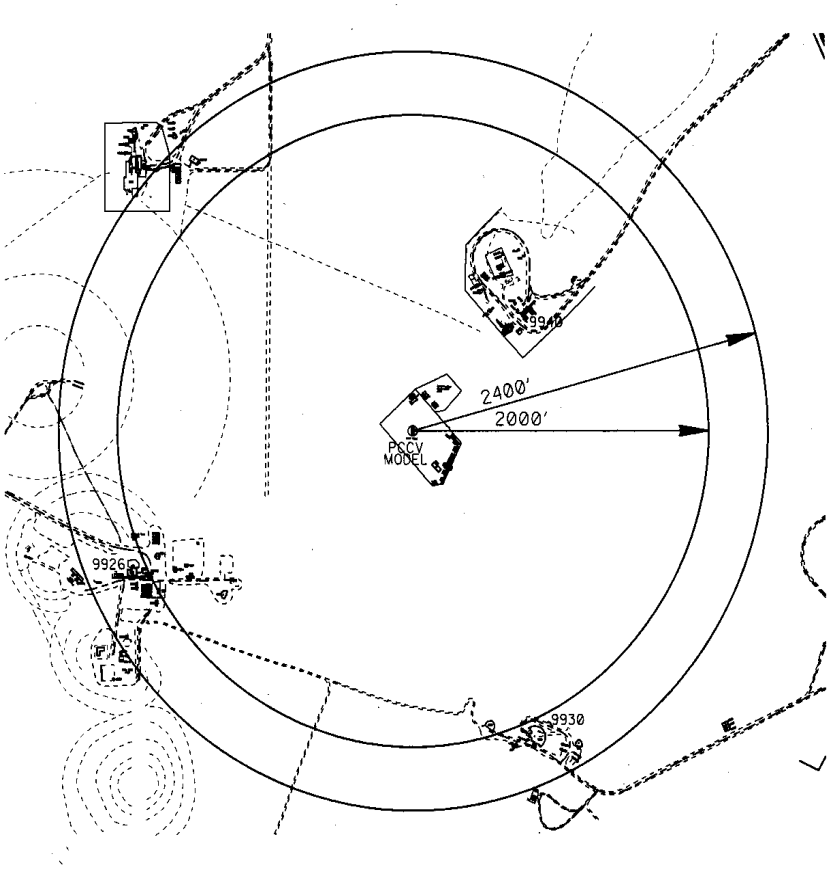

Figure 5.14 PCCV SIT/ILRT, LST, SFMT Exclusion Zone

Personnel were permitted to approach the model after the pressure has stabilized and the test conductor (TC) determined that it was safe to approach the model.

5.2.3 Limit State Test

The LST was designed to fulfill the primary objectives of the PCCV test program, i.e. to investigate the response of representative models of nuclear containment structures to pressure loading beyond the design basis accident and to compare analytical predictions to measured behavior. The LST was conducted after the SIT and ILRT were completed and the data from these tests evaluated. The PCCV model was depressurized between the SIT/ILRT and the LST. The LST began at 10:00 AM, Tuesday, September, 26, 2000, and continued, without depressurization, until the test was terminated just before 5:00 PM on Wednesday, September 27.

The exclusion zone for the LST covered the same circular area of radius 600 m (2,000'), centered at the PCCV model, as shown in Figure 5.14. At this radius, the estimated peak free-field overpressure due to a sudden burst at an internal pressure 2.1 MPa or 300 psig [34] is 1.66 kPa (0.24 psi). This is below the free-field allowable whole body exposure of 3.4 kPa (0.5psi) specified by SNL Environmental Safety and Health (ES&H) regulations. The safety observers monitored the exclusion zone at all times during the LST to make sure no intruder entered this area. In addition, the safety observers monitored the area above the model for aircraft. If an aircraft had approached the exclusion zone, pressurization of the model would have been suspended or held until the aircraft cleared the exclusion zone.

The pressure and average temperature time histories during the LST, including depressurization, are plotted in Figure 5.15. The LST followed the planned pressurization sequence up to the point where the model began leaking.

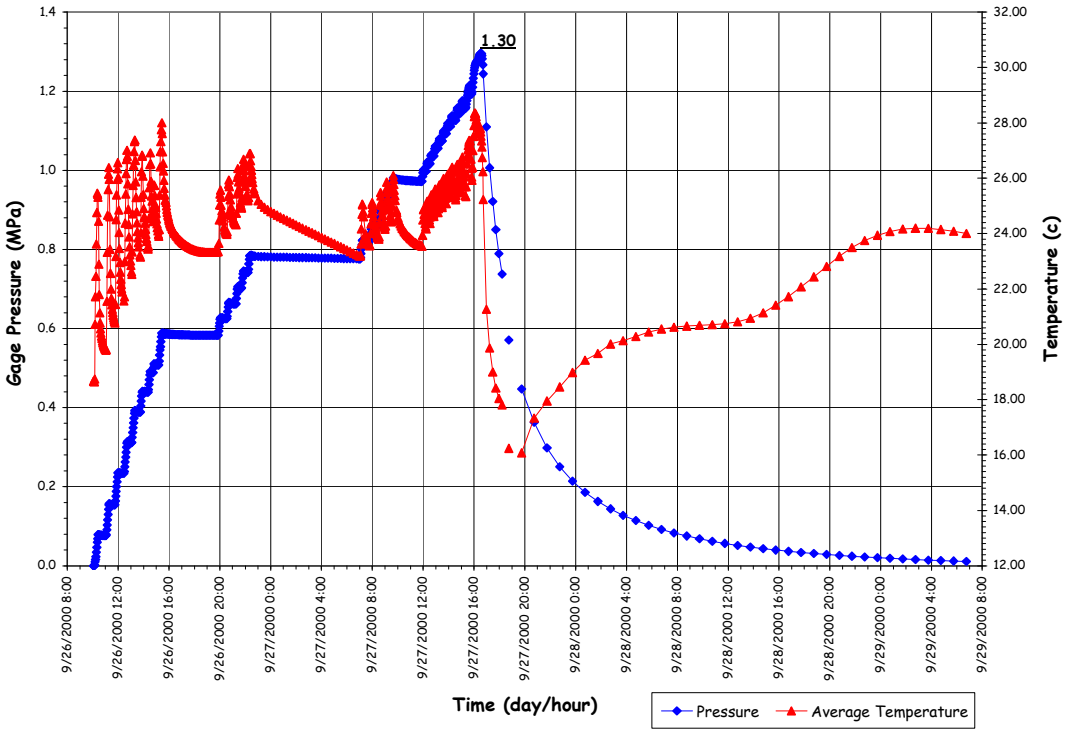

Figure 5.15 Limit State Test Pressure and Average Temperature

Initially, the model pressurization sequence matched the pressurization steps followed for the SIT to allow for comparison of the model response to two identical cycles of loading. The gage stability criteria used during the SIT (i.e. Equation 5.1) was also applied during the LST. Pressurization continued in increments of approximately $0.2P_d$ until a pressure of 1.5 P_d (6.0 kg_f/cm^2 or 85.3 psig) was reached at approximately 4:30 PM. At this pressure, the first planned leak check was conducted by isolating the model and monitoring the temperature and pressure. After approximately three hours, a leak rate of 0.48% mass/day was calculated. Considering previous experience from the ILRT, which

demonstrated that thermal expansion of the model during the day yielded apparent leak rates in this range, the results were interpreted to indicate that the PCCV model was leak-tight.

Pressurization of the model continued in increments of approximately $0.1P_d$ until a pressure of $2.0P_d$ ($8.0\ kg_f/cm^2$ or 113.8 psig) was reached at approximately 11:00 PM. At this pressure the model was again isolated to perform a planned leak check. This leak check was also planned to be held for 8 hours to allow the test team to partially stand down for a rest period. A 'skeleton crew' consisting of the TC, Data Acquisition System Operator (DO), and Nitrogen Supply Operator (NO) continued to monitor the response of the model and all other systems until approximately 7:00 AM on September 27. This pressure hold and leak check was also selected below the lower bound prediction for the onset of structural yielding (i.e. yielding of the rebar or tendons) to ensure the model would remain relatively stable during this period. After approximately eight hours, the calculated leak rate was 0.003%, i.e., essentially zero. This confirmed the interpretation of the leak check results at 1.5 P_d and also demonstrated the greater accuracy of the leak rate results when the model is thermally stable.

Pressurization of the model resumed at 7:00 AM in increments of $0.1P_d$, with increasing dwell time between pressure steps (~30 minutes) required to meet the gage stability criteria. As the pressure was increased to the next planned leak check at $2.5P_d$, liner strain gages in the vicinity of the E/H (LSI-C-K5-12) began registering rapidly increasing strains in excess of 1%. At $2.4P_d$, the acoustic system operator (AO) reported hearing a change in the acoustic output which might indicate that "something had happened." At approximately 10:00 AM at a pressure of $2.5P_d$ ($10.0\ kg_f/cm^2$ or 142.2 psig), the model was isolated for the third planned leak check. After approximately 1-1/2 hours, a fairly stable leak rate of 1.628% mass per day was calculated. The leak rate calculations at 1.5, 2.0, and $2.5P_d$ are plotted in Figure 5.16. Coupled with the acoustic data that continued to confirm some new event had occurred, it became clear that the model was leaking, most likely from a tear in the liner in the vicinity of the E/H. Plots of the output of the four internal acoustic sensors surrounding the E/H at 2.3, 2.4, and 2.5 P_d are shown in Figure 5.17.

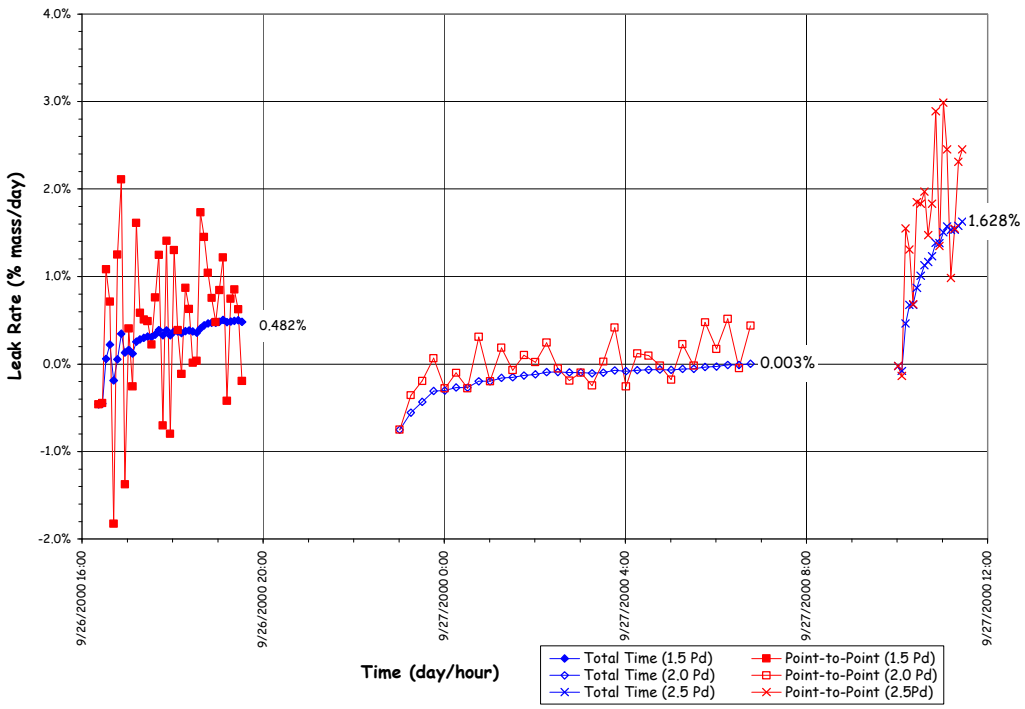

Figure 5.16 LST Calculated Leak Rates at 1.5, 2.0 and 2.5 P_d

After consulting with NUPEC and the NRC, the TC concluded that the model had functionally failed between 2.4 and 2.5 P_d and directed a change in the pressurization plan. Since the model was leaking, the next goal was to pressurize the model as highly as possible to collect data on the inelastic response of the structure and to observe, if possible, a structural failure mode. Pressurization continued in increments of 0.05 P_d, as planned. However, the gage stability criteria was abandoned and the hold time at each pressure step was reduced to less than 10 minutes.

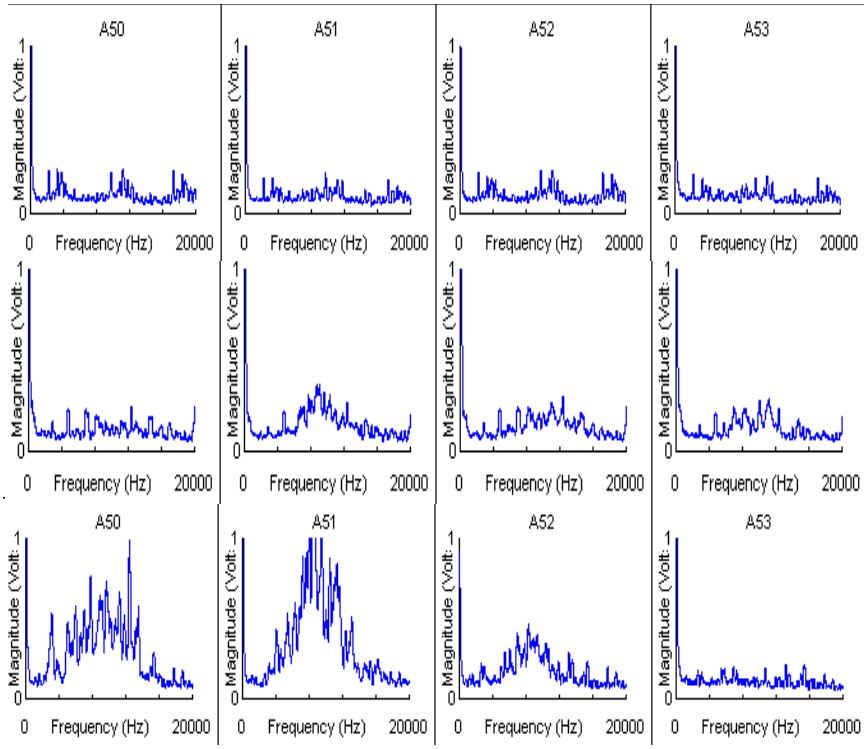

Figure 5.17 Internal Acoustic Sensor Signals at the E/H

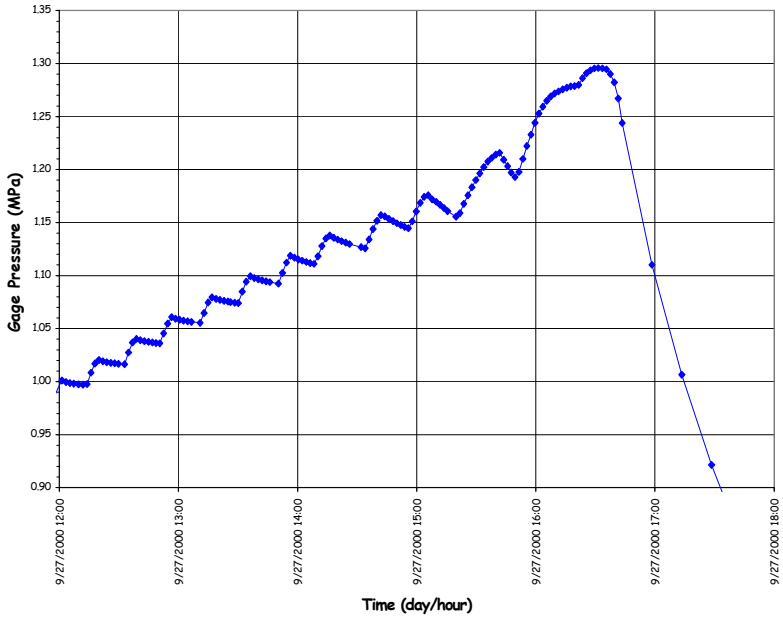

Figure 5.18 LST Pressure Time History, 2.5 to 3.3 P_d

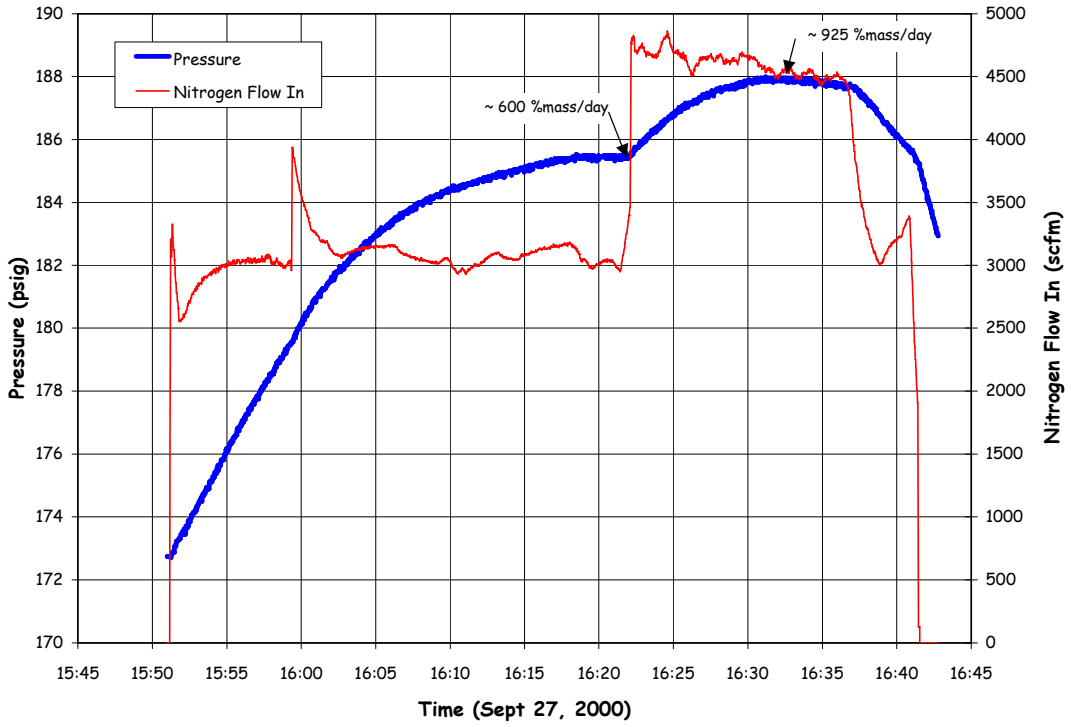

Figure 5.19 LST Pressure and Flow Rates at Maximum Pressure

The PCCV model was pressurized to approximately $3.0P_d$, with increasing evidence of leakage and increasing liner strains. At $3.0P_d$, it became increasingly difficult to pressurize the model, and the nitrogen flow rate was increased to 99 std.m^3/min (3500 scfm). At this flow rate, the pressure in the model was increase to $3.1P_d$. However, the pressure dropped steadily after reaching this pressure. The leak rate at this point was estimated to be 100%.

The nitrogen flow rate was increased to the maximum capacity of the pressurization system, 142 std.m^3/min (5000 scfm), and the pressure was increased to slightly over 3.3 P_d before the leak rate exceeded the capacity of the pressurization system. The pressure time history and flow rates during the final phase of the test are shown in Figures 5.18 and 5.19. Since it was no longer possible to increase the pressure in the model and the supply of nitrogen was nearly exhausted, the TC decided to begin terminating the test.

The isolation valve was closed and the model was allowed to depressurize on its own. The terminal leak rate was estimated to be on the order of 900% mass/day. (The maximum flow rate of nitrogen, 5000 scfm, is equivalent to a leak rate of 1000% mass/day.) Estimated leak rates during the final pressurization and depressurization phases are shown in Figures 5.20 and 5.21.

After the model pressure was reduced to 1.0 P_d, test personnel were able to inspect the model close-up. Nitrogen gas was observed (heard and felt) escaping through many small cracks in the concrete around the penetration sleeves and at the tendon anchors. It was speculated that the liner acted as a leak chase, allowing nitrogen gas escaping through a tear or tears in the liner to travel between the liner and the concrete until it found an exit path through a crack in the concrete or a conduit in the tendon duct.

At maximum pressure, local liner strains of up to 6.5% were recorded and global hoop strains (computed from the radial displacement) at the mid-height of the cylinder averaged 0.4%. While large liner strains were observed, causing suspicion that the liner might have torn in several locations, the remainder of the structure appeared to suffer very little damage with the exception of more extensive concrete cracking at some locations. The largest crack was observed to the left of the E/H, shown in Figure 5.22. This is the same location as the crack photos shown in Figures 5.10 and 5.11. There was no indication of tendon or rebar failure. The detailed results of the LST are discussed in Section 5.3.2.1.

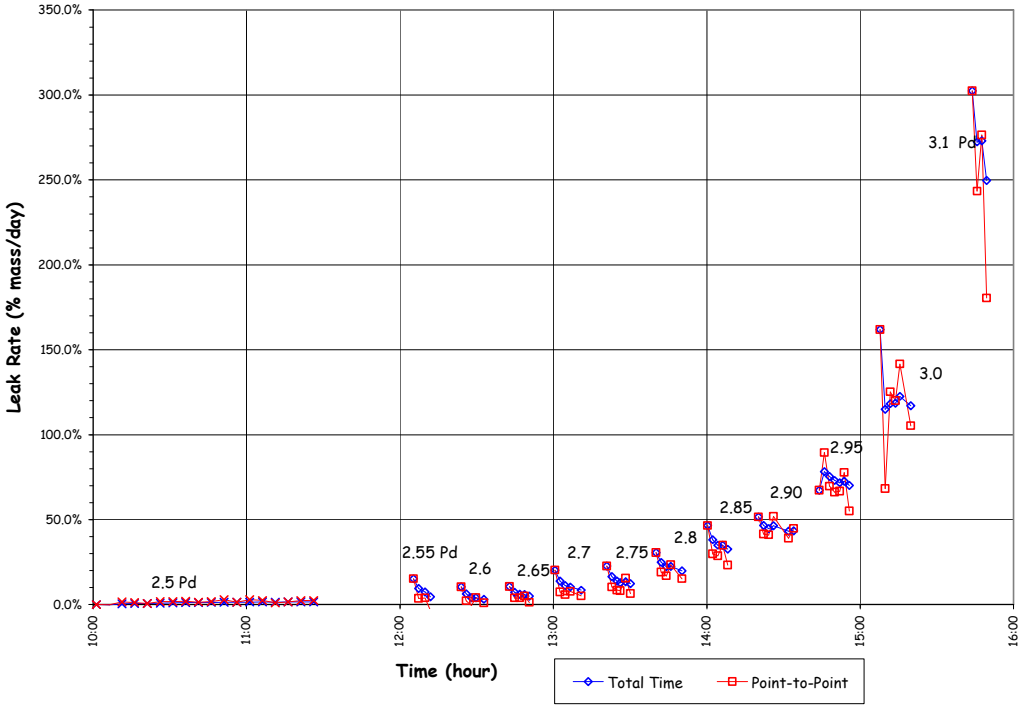

Figure 5-20. LST - Estimated Leak Rates (2.5-3.1 P_d)

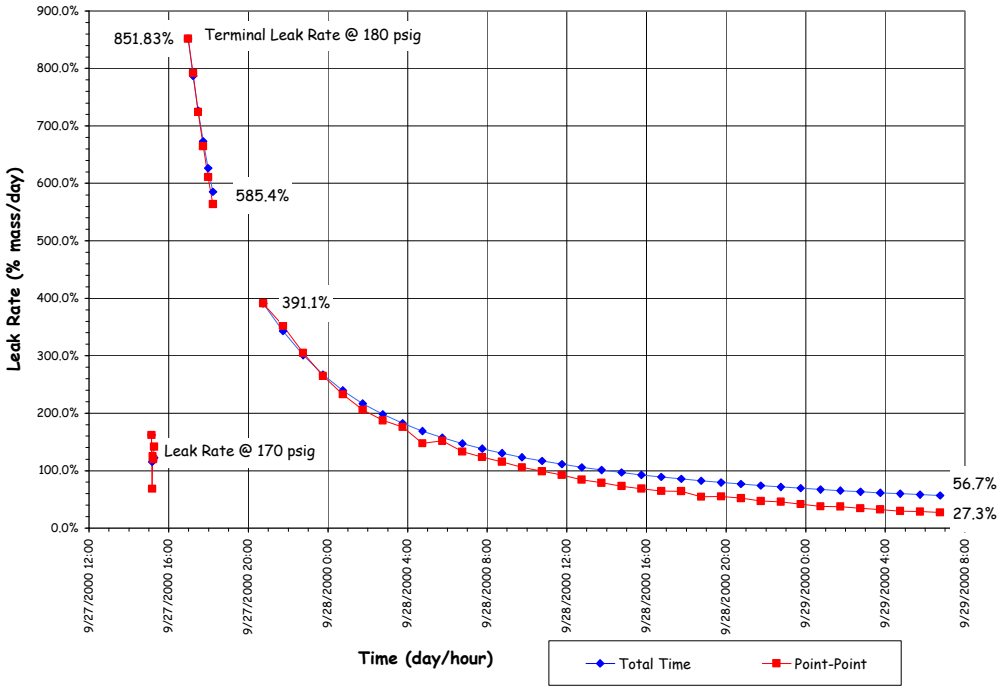

Figure 5.21 LST Estimated Terminal Leak Rates

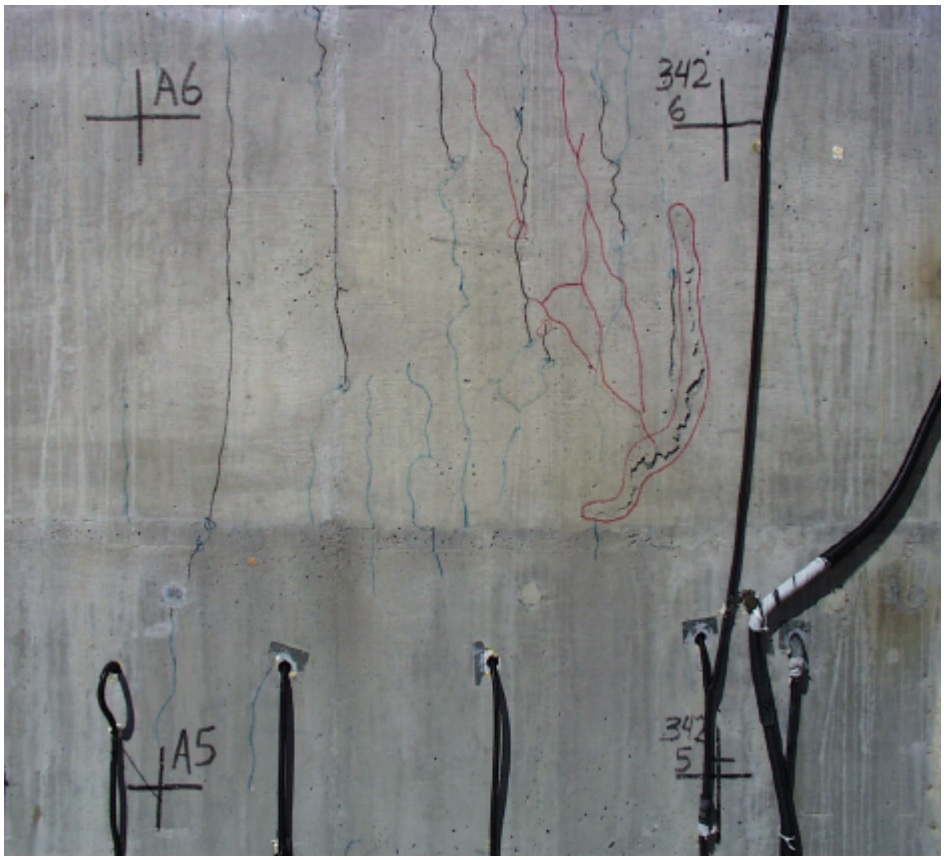

Figure 5.22 Post-LST Cracks at Azimuth 350 degrees, Elev. 4680 to 6200 (Grid 45)

After the model had completely depressurized, it was purged with fresh air, the E/H was removed, and detailed posttest inspection of the inside of the model began. A cursory inspection of the model identified 26 discrete tears at 18 separate locations. A detailed posttest inspection plan was developed, and the results of this inspection are described in Section 5.3.2.1

5.2.4 Structural Failure Mode Test

Almost immediately after the completion of the LST, it was recognized that while the PCCV model had demonstrated its capacity to resist pressures well above the design pressure and confirmed, arguably, liner tearing and leaking as the functional failure mode, the test objectives were not fully met with respect to observing large inelastic deformations for comparison with analyses, and witnessing the structural failure mode of the PCCV model. SNL was tasked by NUPEC and the NRC with investigating the possibility of conducting a second LST.

Two issues needed to be addressed to determine the technical feasibility of reloading the PCCV model. First was the question of whether the LST had caused damage to the structure such that any data obtained by reloading the structure would be compromised and of limited value for comparison with analytical results. The LST data was thoroughly reviewed and, with the exception of the liner and cracking of the concrete, there was no evidence of excessive structural damage. There was also no indication that the tendons had been strained beyond their yield limit and, except for a few isolated measurements, the same was true for the rebar. (Only 27 of the rebar gages registered strains in excess of 0.4% with a maximum of 1.7%–which likely reflects the local perturbation caused by the presence of the gage.) Comparing the radial displacement at the mid-height of the cylinder to the pretest Round Robin predictions in Figure 5.23 clearly illustrates that the structure was on the verge of global yielding but had not undergone a significant amount of inelastic

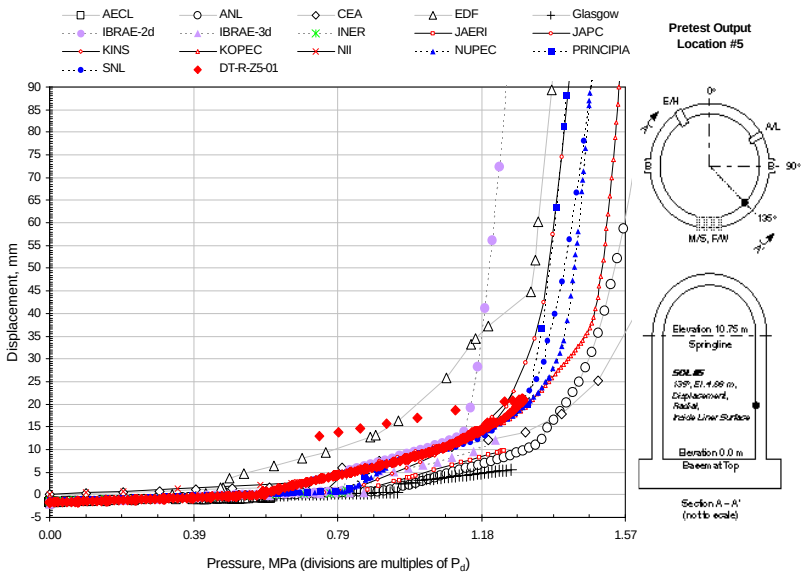

Figure 5.23 LST Radial Displacement at Azimuth 135 degrees, Elev. 4680

deformation. (In this context, only the yielding of the steel and rebar is addressed. Obviously, the loss in stiffness that occurs with global concrete cracking at approximately $1.5P_d$ cannot be recovered.) This was a positive finding for the prospect of reloading the model since most, if not all, of the capacity of the rebar and tendons was still available. Another important conclusion from the consideration of the LST data was that if, in fact, the model was on the verge of global structural yielding, the additional pressure required to cause larger; inelastic deformations was not very large; perhaps only on the order of a few tenths to half the design pressure, i.e. an additional 1.0 to 2.0 kg_f/cm^2 (14 to 30 psig).

The second issue was the requirement to reseal the model in order to repressurize it. Since large sections of the liner were removed as part of the post-LST inspection, the liner was no longer capable of providing an effective membrane to prevent premature leakage. Furthermore, even if the liner tears and cutouts were locally repaired or sealed, it was clear that other areas of the liner were susceptible to tearing at the same pressures (or perhaps even at lower pressures) that caused the liner to tear during the LST. It was necessary, therefore, to devise a cost-effective method of completely replacing the liner function in order to proceed with plans to repressurize the PCCV. The replacement 'liner' was also required to ensure that the model could be repressurized to a level beyond the maximum pressure achieved during the LST. (A corollary of this conclusion was that there was no further need to investigate the response of the liner, and the instrumentation applied to the liner could be abandoned.)

Furthermore, the SFMT had to be completed within the current program budget and schedule. The concept developed to repressurize the PCCV model is illustrated in Figure 5.24.

The concept consists of sealing the interior surface of the liner with an elastomeric membrane after removing all interior transducers on the liner. After closing the E/H and A/L, the model would be filled with water to 1.5 m (5') from the dome apex, approximately 97% of the interior volume 1,591,000 ltr (350,000 gal). Filling the model with water would provide several advantages:

1. The leak rate of water through any tears in the liner is much less than the corresponding leak rate of gas. Therefore, even if a leak path developed, the flow rate capacity of the pressurization system should be adequate to compensate for the leak.
2. By maintaining a gas pocket in the model, the pressurization system used for the LST, with nitrogen gas as the pressurization medium, could be used for the SFMT without any major modifications. The only modification required would be installing additional piping inside the model to allow the gas to be introduced at the dome apex and to fill (and drain, if necessary) the model. Reducing the volume of gas to be pressurized lowered the demand on the pressurization system in the event of a leak, as well as the volume of gas required to conduct the test. In the

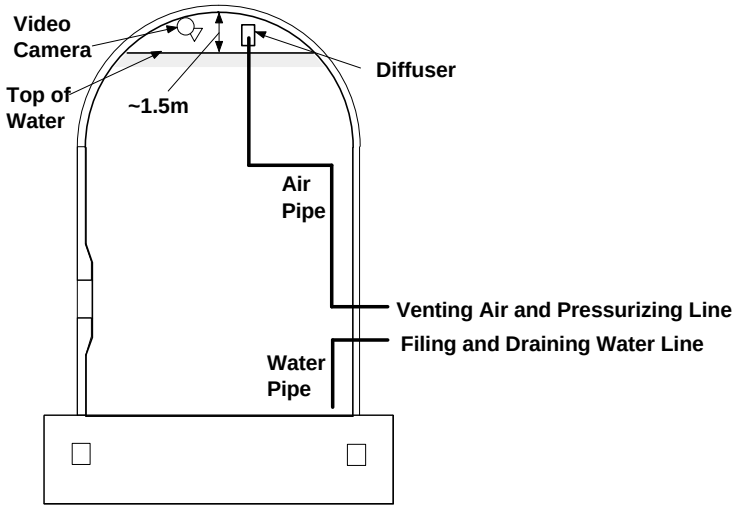

Figure 5.24 PCCV Structural Failure Mode Test Concept

case of the SFMT, a pressurized tube trailer could be used instead of the more expensive liquid nitrogen source required for the LST.

3. Since the pressurization system could compensate for small leaks, it is not essential that the elastomeric liner be completely leak-tight, only that the leaks would be small enough to allow the model to be pressurized to the desired level.
4. Water leaks would be readily visible, compared to gas leaks.
5. In the event of a catastrophic PCCV model rupture, the energy stored in the model nearly filled with water is much less than the stored energy if pressurized to the same level with gas. As a result, the safety exclusion zone around the model could be reduced, if necessary.

At the same time, filling the model with water would have some disadvantages:

1. Any instruments or other electrically-powered components (lights, cameras, etc.) inside the model would have to be removed or completely sealed.
2. The internal pressure would not be uniform due to the hydrostatic head, approximately 1.4 kg_f/cm^2 (20 psig).

These disadvantages, however, were not deemed significant, and efforts focused on selection of a suitable liner. A number of vendors were contacted, and two proposals for sealing the liner were considered. One proposal was to prefabricate a 5 mm (200 mil) PVC sheet liner, which would be installed inside the model by heat welding the seams and sealing around the penetrations using ring clamps. The second proposal was to spray on a two-part polyurea coating, also a minimum of 5 mm (200 mil) thick. After considering both proposals, the sprayed-on lining was selected since it could be more readily adapted to the irregular liner surface and had significant cost and schedule advantages. The elastomeric liner was installed by Ershigs Corporation[31] in August, 2001 after the interior model inspection was completed and all the surface instrumentation was removed. The application of a test sprayed-on liner is shown in Figure 5.25.

After the elastomeric liner was installed, the interior instrumentation for the SFMT was installed. A reduced set of instruments was selected, allowing one data acquisition computer to scan all the gages in less than 60 seconds to support 'rapid' pressurization of the model. The instrumentation suite for the SFMT consisted of the following (A complete list of all the SFMT gages is provided in Appendix H):

[31] Ershigs, 742 Marine Drive, PO Box 1707, Bellingham, WA 98277, (http://www.ershigs.com/)

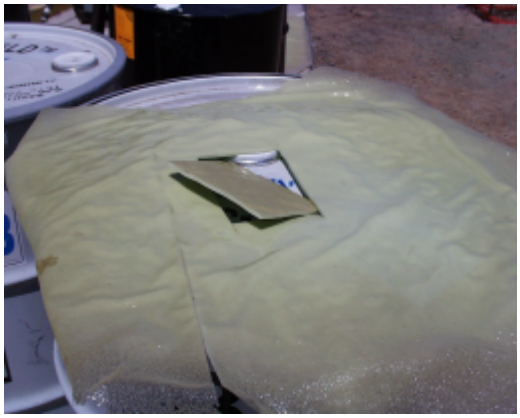

Figure 5-25. Test Specimen of Elastomeric Lining

1. All interior gages used for the LST were removed or abandoned. These were replaced by 20 waterproof LVDTs, 17 radial and three vertical, located as shown in Figure 5.26.
2. Five interior pressure transducers, three below water at the base, cylinder mid-height, and springline, and two to measure the gas pressure.
3. Two interior video cameras and lights to monitor the E/H and the water surface.
4. 18 exterior liner strain gages
   a. 14 at meridional at wall-base junction
   b. Four at hoop stiffener details
5. 82 rebar strain gages (Standard Output Locations (SOLs)).
   a. 35 rebar gages (all 22 SOL plus 13 meridional at wall-base junction)
   b. 47 gage bars (all surviving)
6. All surviving tendon strain gages and all load cells.
7. Soundprint® acoustic monitoring (external sensors only).
8. Concrete strain (six SOFO gages).
9. Four external digital video cameras at 0 degrees, 90 degrees, 270 degrees, and 360 degrees, completely covering the PCCV cylinder wall.

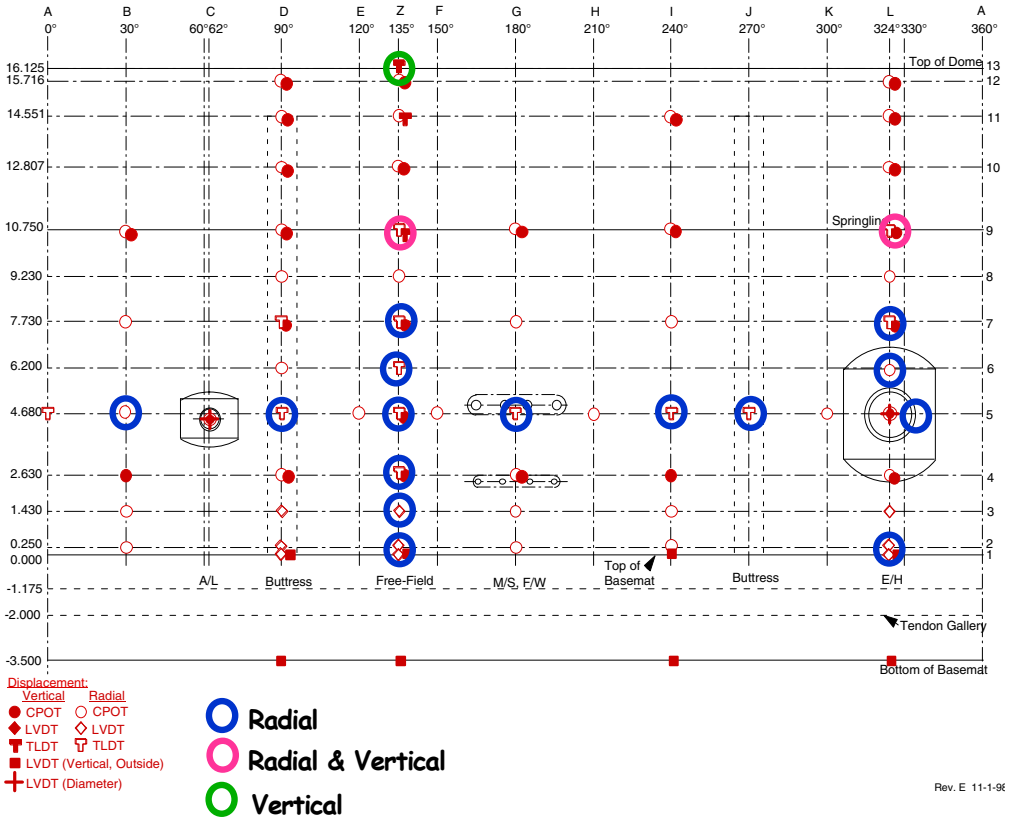

Figure 5.26 SFMT Displacement Transducer Layout

After completing the installation and all test-readiness checks, the E/H cover was installed and sealed. A low pressure pneumatic test was conducted to check for leaks on October 3, 2001. The pressure and temperature time histories for the leak test are shown in Figure 5.27. The leak test began at approximately 09:30 and a leak was detected (via the acoustic system) at approximately 0.2 Pd (~12 psig). Pressure was increased to the target pressure of 0.5Pd (30 psig), at which time the vessel was isolated and monitored for a 24-hour leak test. The acoustic system (multiple sensors) continued to output signals consistent with a leak in the model and several potential leak locations were identified.

Once the model was deemed stable, the nitrogen supply was isolated and a close inspection of the model was conducted. Through a combination of visual/auditory inspection, hand-held acoustic monitoring, and the application of soap-water solution, a number of locations were discovered where nitrogen gas was leaking from the model.

- The largest apparent leak was from a crack on the left-hand side of the 90-degree buttress at an elevation of approximately 6 m (20') above the top of the basemat (Level 6 in the cardinal coordinate system). This leak was the first detected by the acoustic system and was immediately confirmed during the close-up inspection.
- Secondary leaks, identified by the acoustic system, were confirmed at 150 degrees/3 and 6 m (10 and 20') and 210 degrees/4.5 m (15'). These leaks appeared to be through previously existing cracks in the concrete. The leak at 150 degrees was along the horizontal construction joints between C1, C2, and C3 as well as along a vertical crack extending between C2 and C3. The leak at 210 degrees also appeared to be through a previous crack.
- The acoustic system also suggested leaks at 300 degrees/1 to 2 m (3 to 6-1/2') and 360 degrees/0 m, but close-up examination could not confirm leakage at either location.
- During the close-up inspection, a leak was also detected at 30 degrees/5 m (16') which was not initially identified by the acoustic system.
- Close-up inspection of the penetrations also revealed leakage at the F/W penetrations. Their was no evidence of leakage at the E/H, A/L, or M/S penetrations.

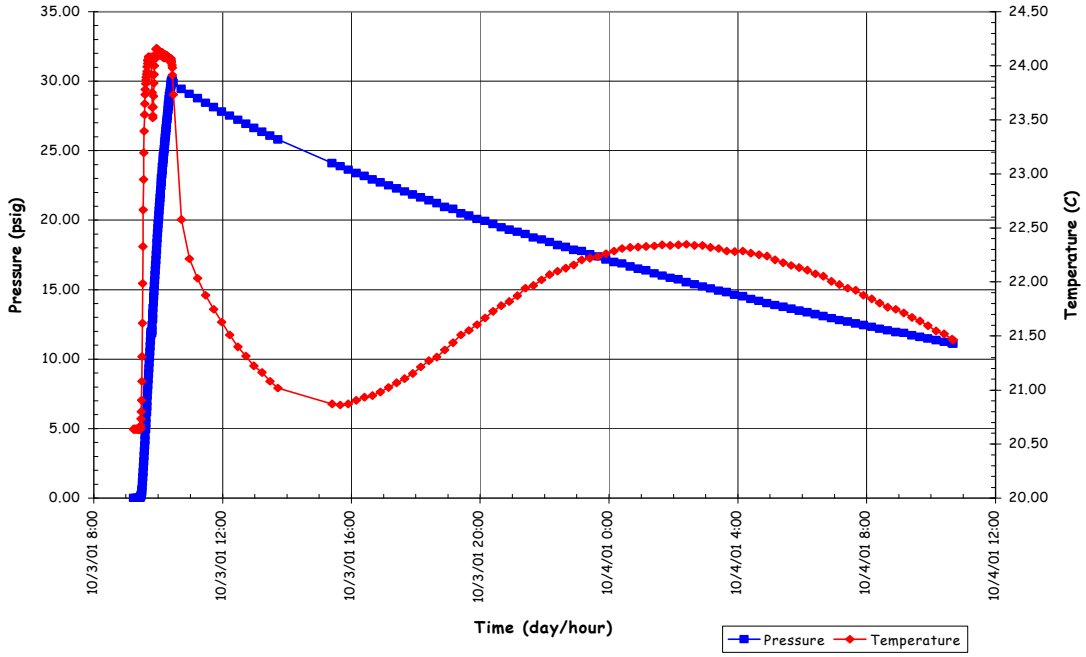

Figure 5.27 Pre-SFMT Leak Test Pressure and Temperature

These results indicated that, in spite of the manufacturer's quality control procedures coupled with detailed visual inspection (individual locations that appeared suspect were also sealed with silicone sealant prior to closing the model), the sprayed-on liner was not impermeable. Once the gas escaped through the sprayed-on and steel liners, it migrated between the steel and concrete until it found an exit path. The pressure did not appear high enough to tear the sprayed-on liner when a leak was first detected.

The calculated leak rate, shown in Figure 5.28, was initially 70% mass/day at the maximum pressure of 2.1 kg_f/cm^2 (psi) decaying to 45% at 0.77 kg_f/cm^2 (11 psi) over 24 hours. The sound levels as detected by the SoundPrint system (shown in Figure 5.29), which are roughly proportional to the rate of gas escaping, indicated a stable leak rate that was, to a large extent, independent of the pressure.

Based on these results, it was concluded that the leak was most likely due to a pre-existing hole(s) in the sprayed on liner which did not increase (or decrease) significantly during pressurization or during the leak test. (The equivalent orifice size reduced from about 6 mm (0.25“) at 2.1 kg_f/cm^2 (30 psi) to 5 mm (0.20“) at 0.8 kg_f/cm^2 (12 psi), based on the calculated leak rates.) As a result, the SFMT could be conducted without repairing the sprayed-on liner while maintaining a reasonable chance that the leak would not grow significantly and overwhelm the capacity of the pressurization system. (Nevertheless, during an unscheduled one-month postponement of the SFMT, the surface was retested with a ‘spark-tester,’ and a few small holes were discovered and sealed. The model was then resealed and readied for filling with water.)

Filling the PCCV with water and the SFMT began at approximately 09:00 November 6, after the initial data scan was taken, and continued until November 8, 2001. Slow water leaks were initially observed late November 6, after the model was about one-quarter full, however, the amount of water leaking was insignificant. The pressure time histories at various elevations in the model from the start of filling to the SFMT are shown in Figure 5.30. This figure illustrates the hydrostatic head and also reflects the slight loss of water due to leaks. The water level was ‘topped off’ on November 12, prior to the start of the SFMT.

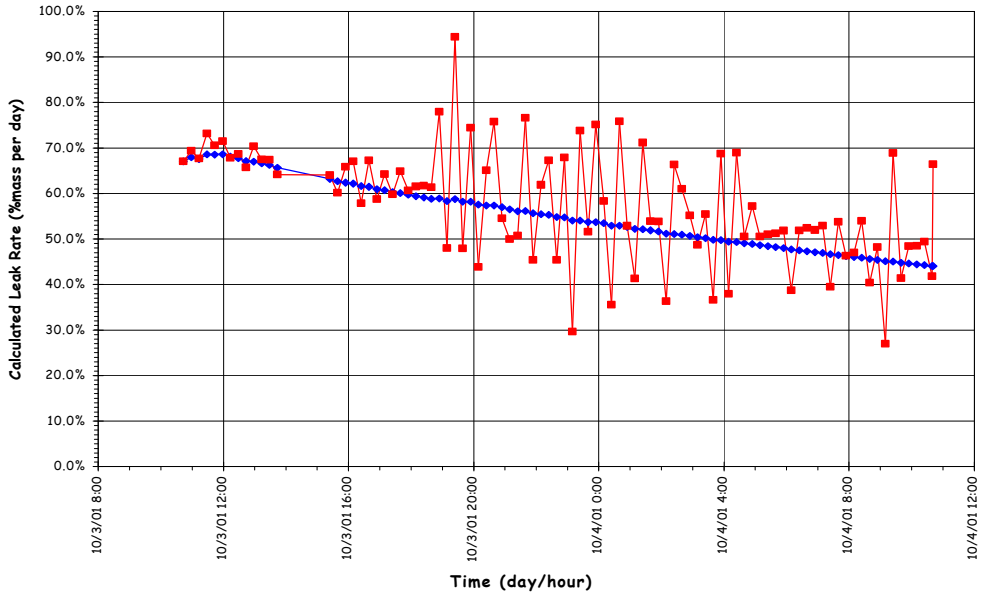

Figure 5.28 Pre-SFMT Leak Rate Test

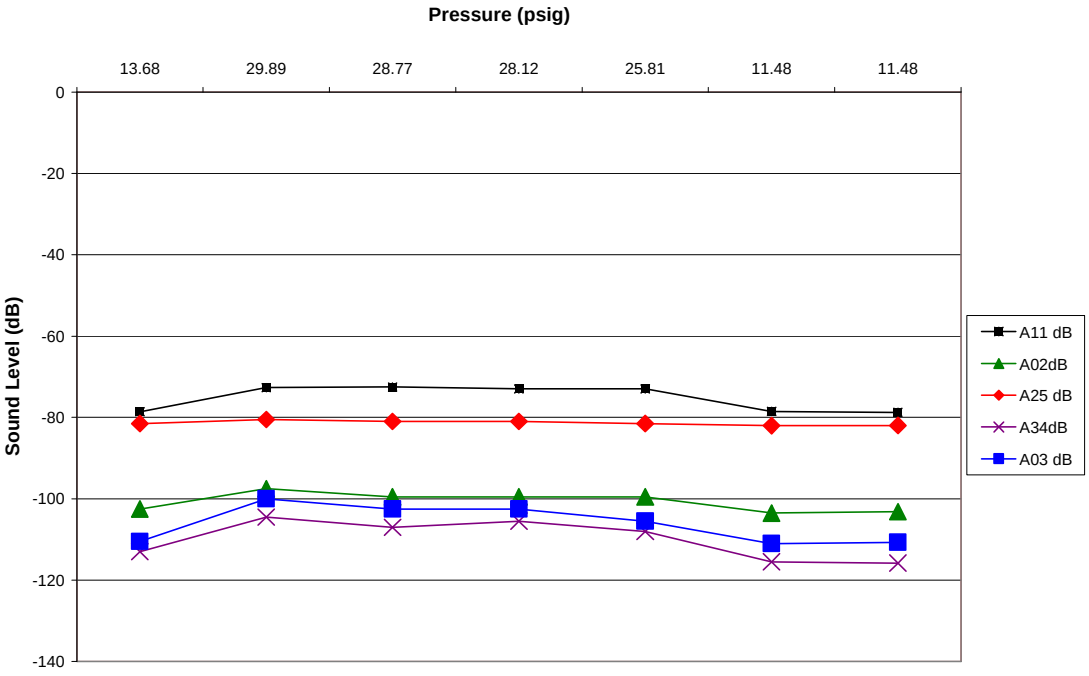

Figure 5.29 Pre-SFMT Leak Test Acoustic Data

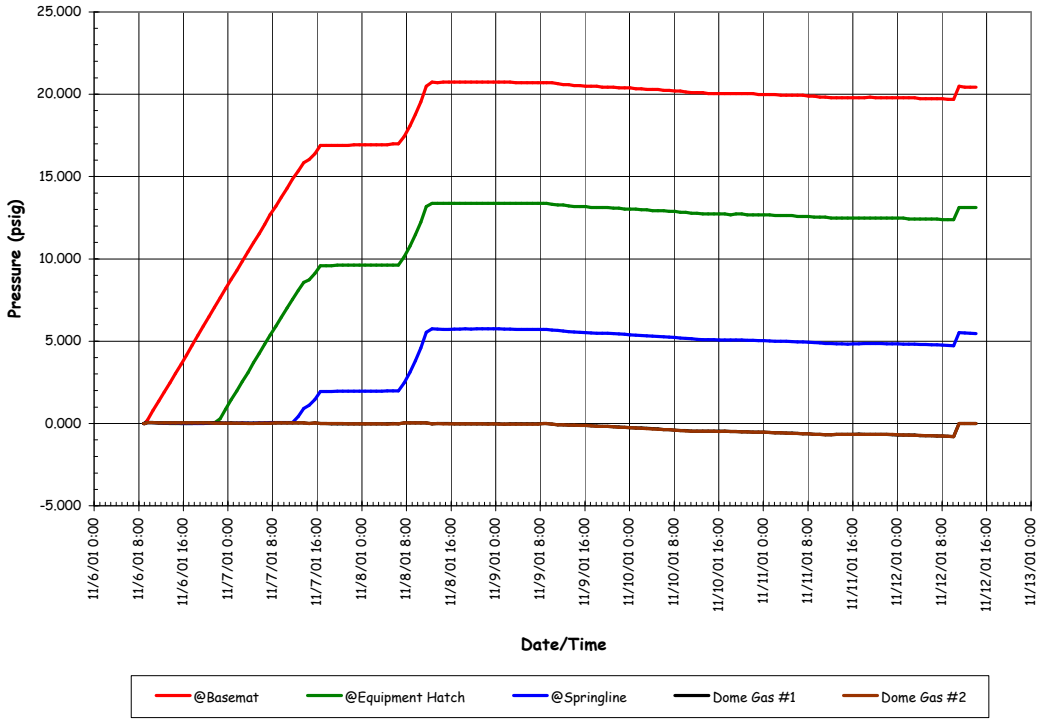

Figure 5.30 Pre-SFMT Hydrostatic Pressures

The test sequence planned for the SFMT was to rapidly pressurize the model using nitrogen gas to compensate for the known leaks in the model. The minimum flow rate capacity of pressurization system, 14 std.m^3/min (500 scfm), would increase pressure in the reduced void space at a rate of about 0.35 kg_f/cm^2 (5 psi) every minute. At this rate, the model could be pressurized to failure in less than an hour.

The SFMT began shortly after 10:00 AM on Wednesday, November 14, 2001. The pressure time histories are shown in Figure 5.31. The pressure time history of all five gages are shown along with the effective model pressure, which is calculated as a volume-weighted average. Any references to the SFMT pressures are to the effective pressure, unless noted otherwise.

The model was continuously pressurized at a rate of approximately 0.35 kg_f/cm^2 (5psi)/min. All active sensors were continuously scanned at intervals of approximately 30 seconds and the video cameras continuously recorded the response of the model. As the pressure increased, evidence of leakage was visible as increasing wetting of the concrete surface. At 10:38 AM, the effective pressure in the model equaled the peak pressure achieved during the LST, 3.3 Pd (1.29 MPa or 188 psig). At approximately 10:39 AM, the acoustic system recorded a very high noise level event, which was interpreted as the breaking of a tendon wire. At this point in the test, events occurred very quickly. Shortly after detecting the wire break, a small spray of water was observed at approximately 0 degrees Azimuth and additional tendon wire breaks were detected by the acoustic system with increasing frequency. The wire break events are plotted in Figure 5.32, along with the effective pressure and the radial displacement at Azimuth L (324 degrees), elev. 6 (6280), as a function of time.

The rate of pressurization decreased and the nitrogen flow rate was increased to maintain the pressurization rate. The gas pressure and flow rates are shown in Figure 5.33. The water surface inside the model, viewed through the internal video camera, was dropping slowly, but it was unclear if this was due to leakage or radial expansion of the vessel.

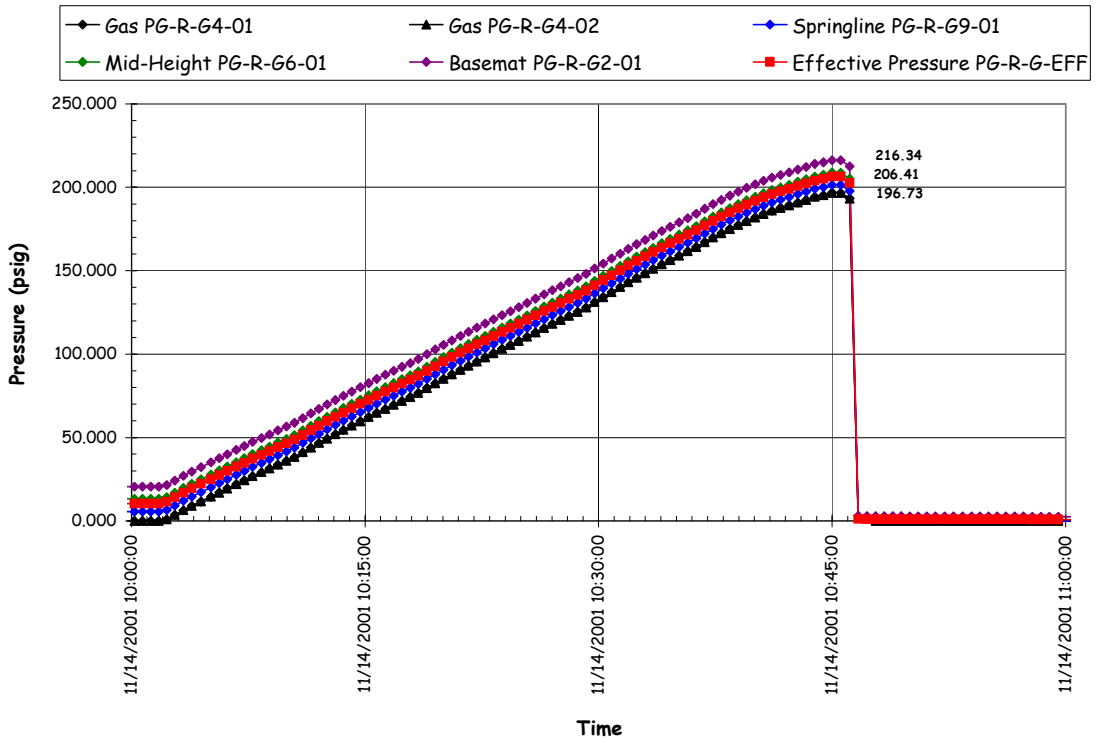

Figure 5.31 SFMT Pressure Time Histories

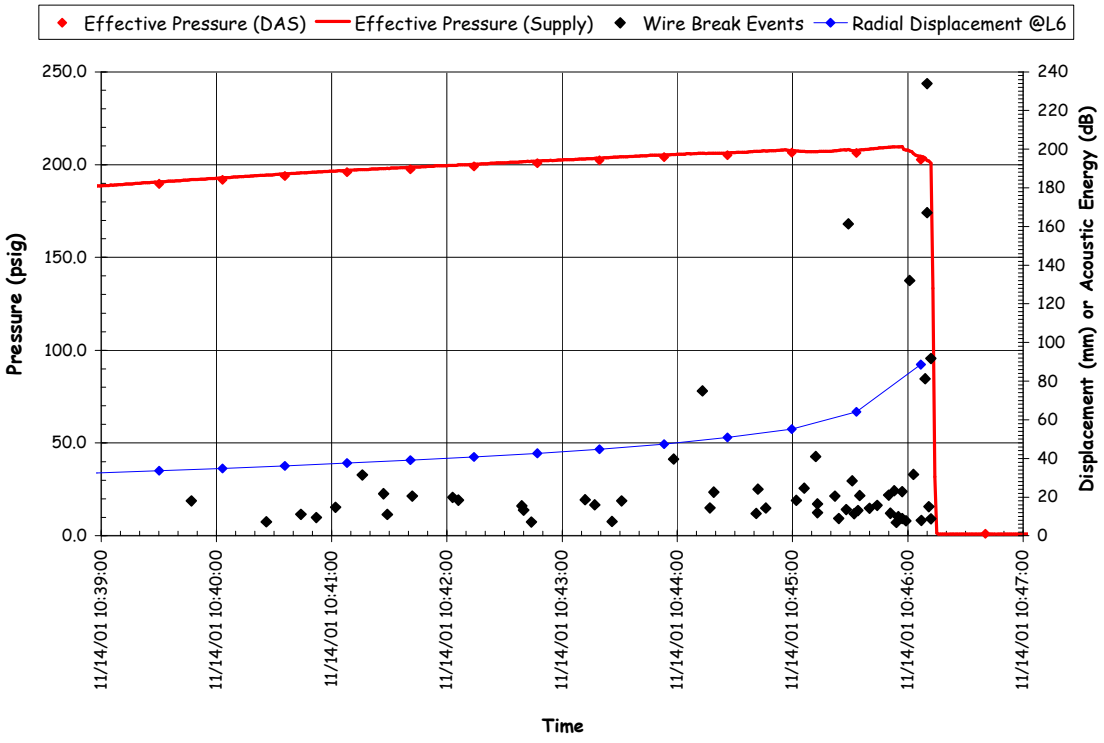

Figure 5.32 SFMT Wire Break Events vs. Pressure vs. Displacement

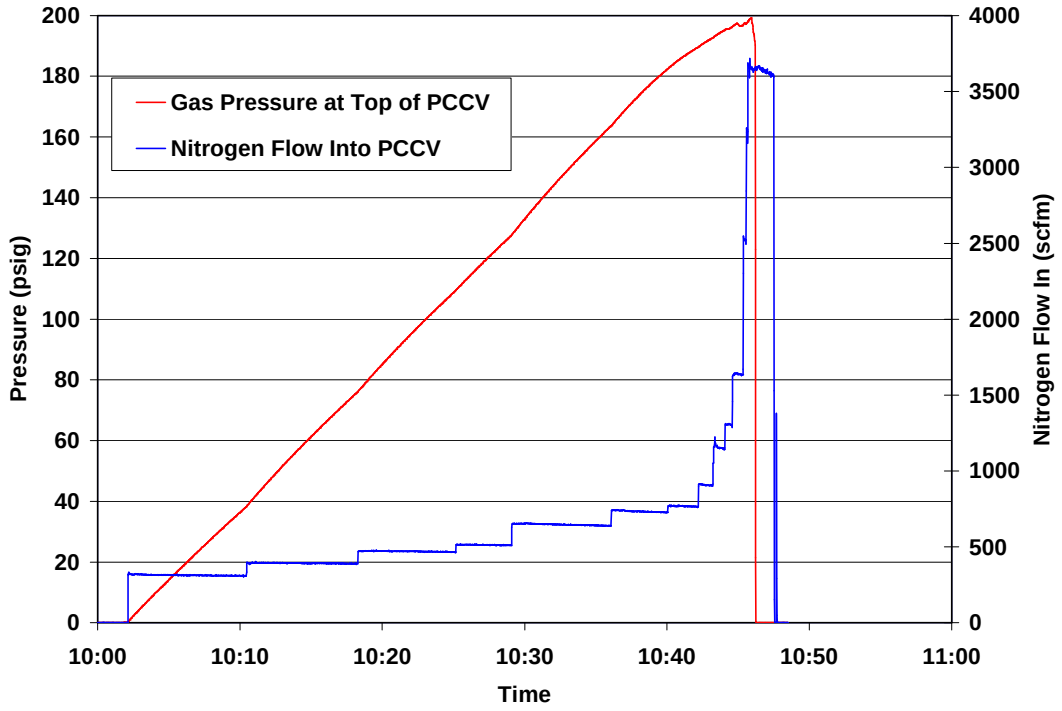

Figure 5.33 SFMT Pressurization System Data

Pressurization of the model continued until a second spray of water was observed and suddenly, at 10:46:12.3, at an effective pressure of 3.63 P_d (1.42 MPa or 206.4 psig), the PCCV model ruptured violently at ~6 degrees azimuth near the mid-height of the cylinder. The rupture propagated vertically in both directions and then radiated circumferentially about 2 m above the top of the basemat, shearing off the cylinder wall. The dome and cylinder wall then came to rest on the instrumentation frame, which apparently prevented the model from toppling over. The entire collapse was over in slightly more than one second. The entire SFMT, including the sequence of rupture and collapse, was recorded by the digital video cameras. A short movie (.mpg) file showing the rupture of the model is included on the enclosed data CD. The moment of rupture is shown from all four angles in Figure 5.34. The video recorded failure of the tendons, including ejection of tendon anchors. The condition of the model after the SFMT is shown in Figure 5.35.

The detailed results of the SFMT are discussed in Section 5.3.3, along with observations from the posttest inspection of the model. In the case of the SFMT, posttest inspection was limited to visual inspection due to the obvious damage and restricted access for safety.

Because of program schedule constraints, demolition of the PCCV model commenced in December, 2001 and was completed in April, 2002. During this period, attempts were made to further inspect the model and characterize the damage caused by the SFMT. However, these efforts were of limited value due to the difficulty of discriminating the damage caused during the SFMT from the demolition process. A few specimens from the model were retrieved, however, more for sentimental value than for providing any further technical insight into the behavior of the model.

5.3 Test Results

5.3.1 Data Files

The response of the model was continuously recorded beginning March 3, 2000, prior to prestressing, through October 11, 2000, following the LST. Additional data was recorded using a modified instrumentation suite from November 6 to 14, 2001 for the SFMT. Data for each set of transducers was saved in individual files and a data management and file

(a) 0 degrees Azimuth

(b) 90 degrees Azimuth

(a) 180 degrees Azimuth

(b) 270 degrees Azimuth

Figure 5.34 SFMT: Rupture of the PCCV Model

Figure 5.35 PCCV Model after the SFMT

naming scheme was developed to facilitate access and utilization of the data. A summary of the data file structure is shown in Figure 5.36.

The basic data was recorded as the output voltage (strain for strain gages, °C for temperature sensors) for each instrument at discrete time steps. This basic data is referred to as the raw, dynamic data. Note that the time reported in the data files is the DAS clock time at the start of a data scan. Since it took up to two minutes to complete a data scan (one minute for the SFMT), the actual time the data was recorded may be up to two minutes later than the recorded time. For pseudo-static loading, this is not a significant issue, but it may have some effect on the response recorded near the end of the LST and SFMT. The raw data is stored as ASCII, tab-delimited text files (.dat)

The raw, DOR is a subset of the raw, dynamic data. The concept of the DOR was defined to facilitate comparison of the data with analysis results. Typically, the analysis results are described as a function of pressure. The DOR is intended to provide a single, stable response value at each pressure step. The DOR were recorded separately from the dynamic data when the gage stability criteria (Eq. 5.1) was met, or at the direction of the test conductor.

The concept of dynamic and DOR data is illustrated in Figure 5.37. In this figure, the dynamic data during and after the LST is plotted along with the DOR for the radial displacement at the cylinder mid-height at 135 degrees. At lower pressures, the data are essentially identical; however, at higher pressures, the drift due to model creep and/or leakage is apparent. Furthermore, the DOR set does not capture the maximum pressure. In subsequent discussions of the DOR, the response at the maximum pressure from the dynamic data has been appended to the DOR for completeness.

Due to the extended length of time over which the data was recorded, the raw data files were separated into individual files by time periods. These periods were chosen to correspond with distinct loading periods, as shown in Figure 5.36. The acronyms for each period were used in the file naming scheme. The full response time history (from March 3 to October 11) for any transducer can be reconstructed by combining the data from the individual files, as illustrated in Figure 5.38 for the radial displacement at the cylinder mid-height at 135 degrees. Gaps in the data represent times when the DAS was shut down for maintenance or when temporary malfunctions (e.g. loss of power, etc.) corrupted the data. Times when the corrupted data was removed from the files are duly noted in the Excel© spreadsheets.

	Before Prestressing	Prestressing	Post Prestressing	System Functionality Test	DAS SHUTDOWN FOR MAINTENANCE	Post SFT	SIT/ILRT	Post SIT/ILRT	Limit State Test	Post LST	Structural Failure Mode Test
Start	3/3/00	3/10/00	5/5/00	7/18/00		8/7/00	9/12/00	9/14/00	9/26/00	9/27/00	11/6/01
End	3/9/00	5/5/00	7/18/00	7/21/00		9/11/00	9/14/00	9/26/00	9/27/00	10/11/00	11/14/01
	BPS	**PS**	**PPS**	**SFT**		**PSFT**	**SITILRT**	**PSITILRT**	**LST**	**PLST**	**SFMT**
RAW	DYNAMIC	DYNAMIC	DYNAMIC	DYNAMIC		DYNAMIC	DYNAMIC	DYNAMIC	DYNAMIC	DYNAMIC	DYNAMIC
	*.dat	*.dat	*.dat	*.dat		*.dat	*.dat	*.dat	*.dat	*.dat	*.dat
	DOR	DOR		DOR			DOR		DOR		
	*.dat	*.dat		*.dat			*.dat		*.dat		
CONVERTED	DYNAMIC	DYNAMIC	DYNAMIC	DYNAMIC		DYNAMIC	DYNAMIC	DYNAMIC	**DYNAMIC**	**DYNAMIC**	**DYNAMIC**
	*.dat	*.dat	*.dat	*.dat		*.dat	*.dat	*.dat	*.dat	*.dat	*.dat
	*.xls	*.xls	*.xls	*.xls		*.xls	*.xls	*.xls	***.xls**	***.xls**	***.xls**
	DOR	DOR		DOR			DOR		**DOR**		
	*.dat	*.dat		*.dat			*.dat		*.dat		
	*.xls	*.xls		*.xls			*.xls		***.xls**		
CORRECTED									DYNAMIC		
									*.xls		
									DOR		
									*.xls		

Figure 5.36 PCCV Test Data File Matrix

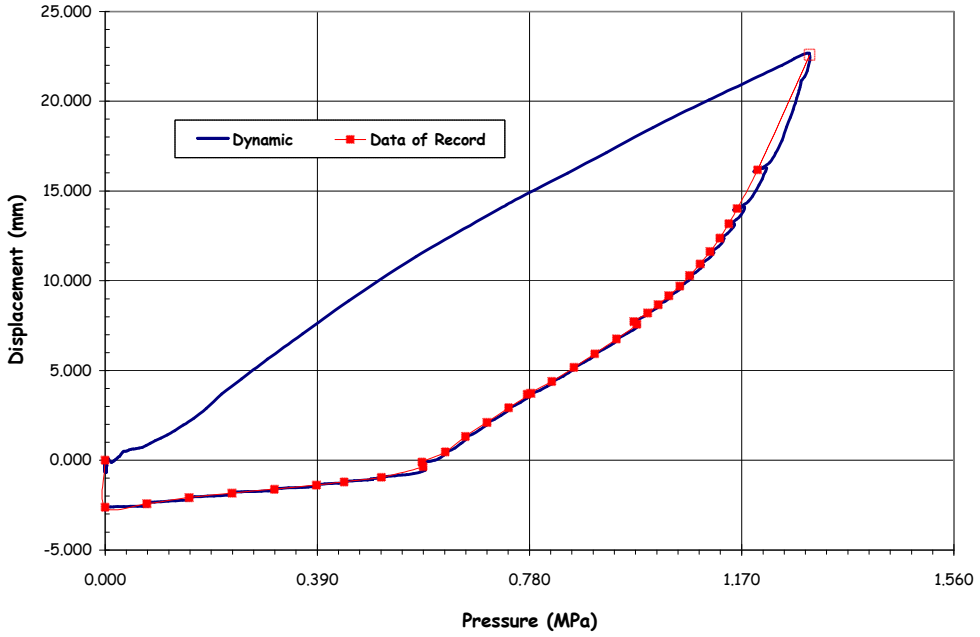

Figure 5.37 Radial Displacement at Azimuth 135 degrees, Elev. 6200

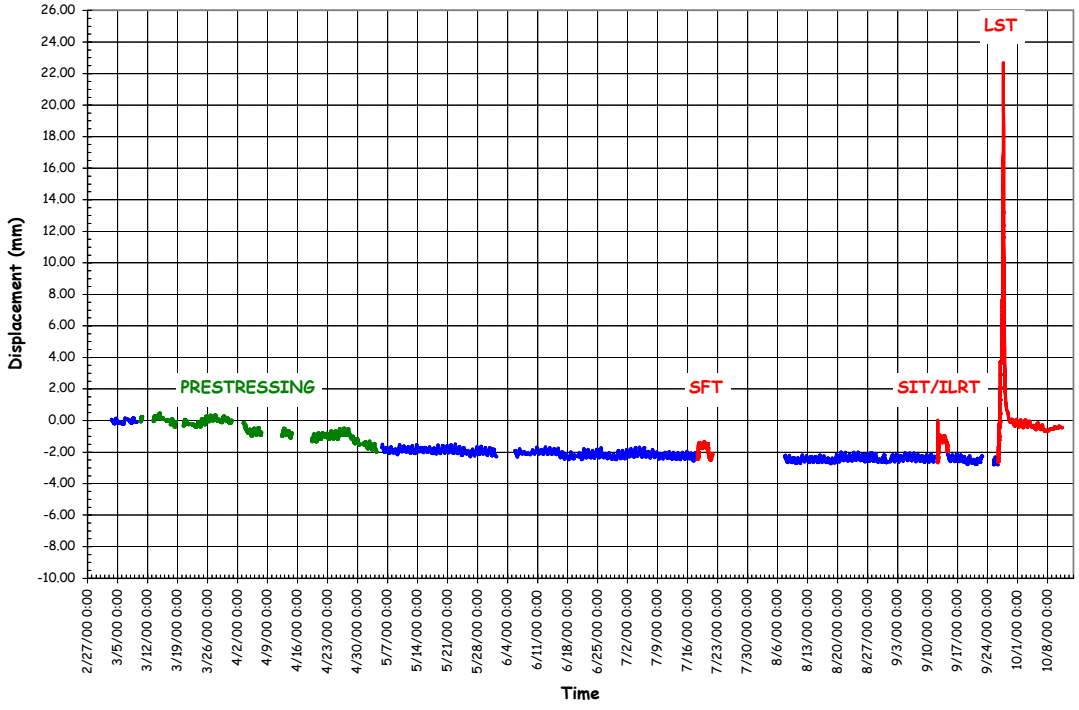

Figure 5.38 Radial Displacement History at Azimuth 135 degrees, Elev. 6200 (DT-R-Z6-01)

After the raw data was stored, it was converted using utility programs constructed as part of the DAS software. The conversion process was described in Chapter 4 and consisted of applying gage specific-gage factors (GFAC) obtained from the manufacturer or from gage calibration test data, correcting for actual gage power supply voltages. This converted data (CONV) was also stored as ASCII, tab-delimited text files (.dat) for each type of gage and loading period.

To simplify access to the data, the converted data files were further reorganized and stored in Microsoft Excel© spreadsheet format (.xls). The data files were grouped by response variable type according to the scheme shown in Table 5.3. Each data file was further subdivided by grouping similar gages on separate worksheets, as shown. Units for each response variable/gage are also shown. The converted data files in Excel© format are provided with this report on a CD. Appendix I provides a complete list of the data files on the disk. The format of each data file consists of the time (at the start of the data scan) in the first column followed by the response for each of the gages, identified by gage name in the following columns. The Excel© data files were also modified to add the average pressure at each time step where appropriate, (i.e., for the pressure tests), the nominal azimuth, elevation, and, in some cases, radius of the gage, and additional information (such as references to an instrumentation drawing detail or tendon number), where applicable.

The data file naming scheme consists of

- the gage type acronym,
- the data type acronym,
- a designation for dynamic (DYN) or DOR, and
- the loading period acronym.

For example, the file:

DISP_CVTD_DYN_LST.xls

contains the converted (CVTD) DYN displacement (DISP) during the LST in Excel© format (.xls).

One final set of data files, corrected data (COR), is also provided. The model was exposed to variations in ambient temperature, both temporal (day/night, seasonal) and spatial (due to direct solar heating), and responded accordingly. Since the converted test data includes the response to ambient thermal conditions, as well as prestressing and pressure loads, and the analyses, typically, do not, an attempt was made to correct the test data and 'remove' the effect of the temperature transient. This correction is described in Appendix J and was only applied to the LST data files.

In addition to the basic data files described above, additional data was collected by the pressurization system, acoustic system, and from visual observation and photographic (still and video records). This data is described in the following sections.

5.3.2 Limit State Test Results

5.3.2.1 Test Data

The LST data (DYN and DOR) is provided on the enclosed data CD in Excel© spreadsheets, as noted in Section 5.3.1. The response of every functioning transducer is provided. The following sections present a synthesis of the data focusing on the critical response measurements.

5.2.3.1.1 Displacements

The displacement data provides the most comprehensive view of the overall or global response of the model. Figures 5.39 through 5.42 show the displacement response as a function of pressure at various azimuths and elevations.

Table 5.3 Data File (Excel©) Format

Gage Type	Gage Type Acronym	Worksheet Label
Displacements	DISP	Unit: millimeters
		Radial
		Meridional
		Hatches
		Instrumentation Frame
Gage Bar Strains	GBST	Unit: strain
		Wall-Base 90 deg
		Wall-Base 135 deg
		Wall-Base 350 deg
		Above Tendon Gallery
Liner Strains	LINST	Unit: strain
		Free-Field Hoop
		Free-Field Merid
		Free-Field Merid Anchors
		E-H Details
		A-L Details
		M-S Details
		F-W Details
		Wall-Base
		Misc Details
Pressure	PRES	Unit: MegaPascal
Rebar Strain	REBST	Unit: strain
		Free-Field Hoop
		Free-Field Merid
		Free-Field Radial Bar
		Basemat
		E-H Bars
		A-L Bars
Temperature	TEMP	Unit: ºCelsius
		Inside Air (includes outside air temperature)
		Inside Liner
		Embedded Concrete
Tendons	TENDON	Unit: Newtons/strain
		Load Cells (grouped by tendon)
		Tensmegs (grouped by tendon)
		Strain Gages (grouped by tendon)
Concrete Strain*	SOFO*	Unit: strain

*Concrete strains by SOFO gages were only measured during prestressing and pressure tests.

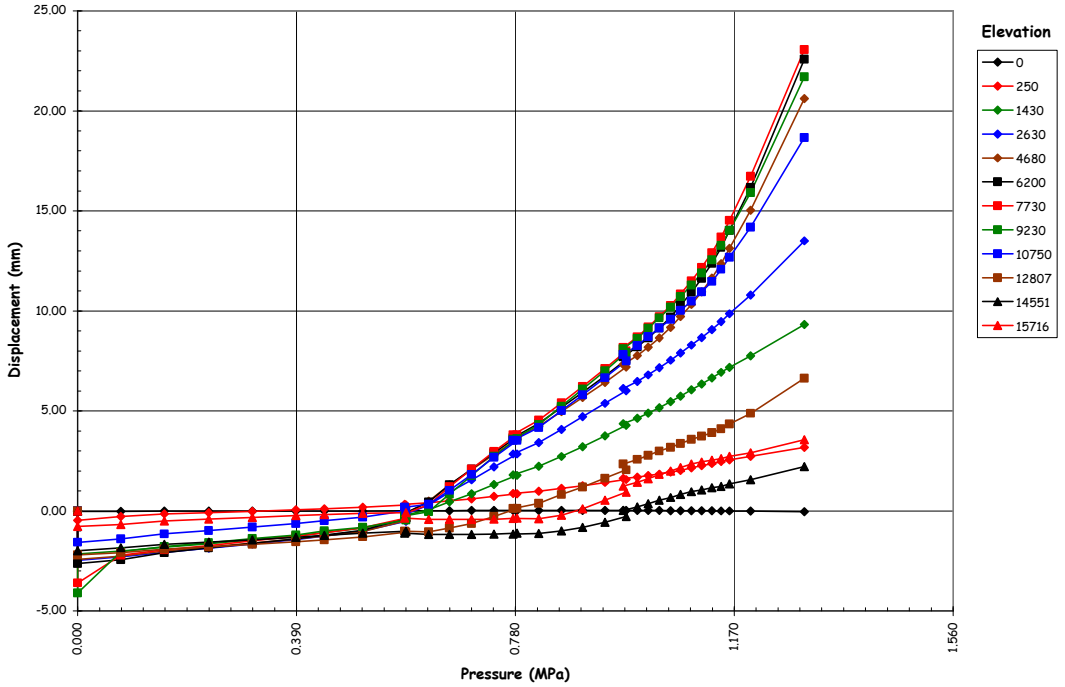

Figure 5.39 LST - Radial Displacement at Azimuth 135 degrees

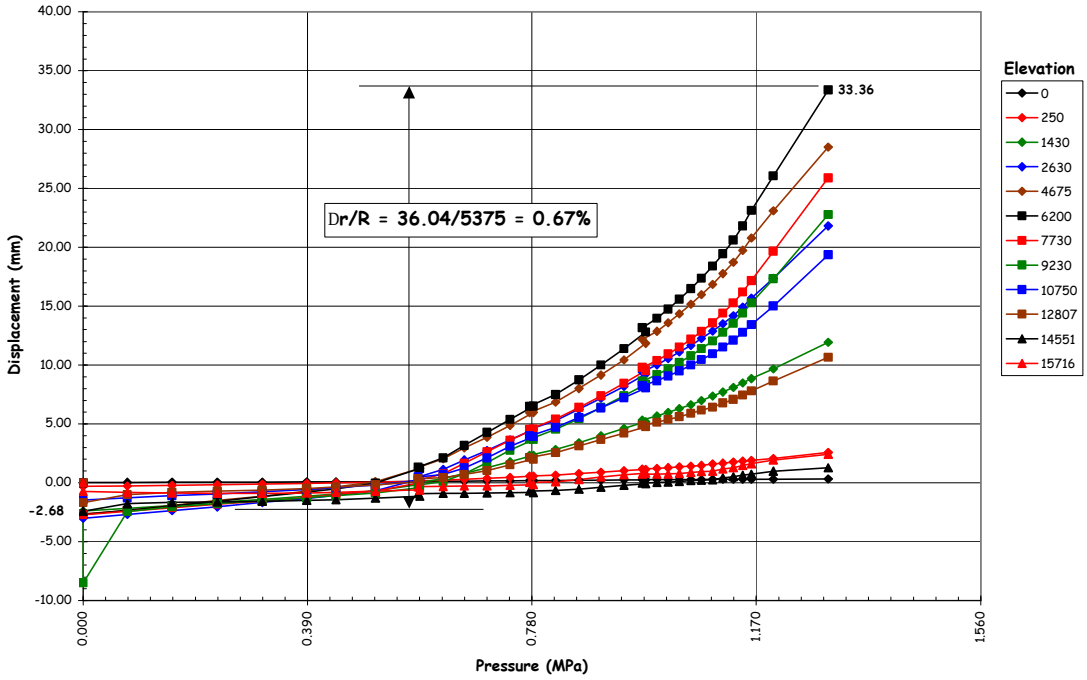

Figure 5.40 LST - Radial Displacement at Azimuth 324 degrees

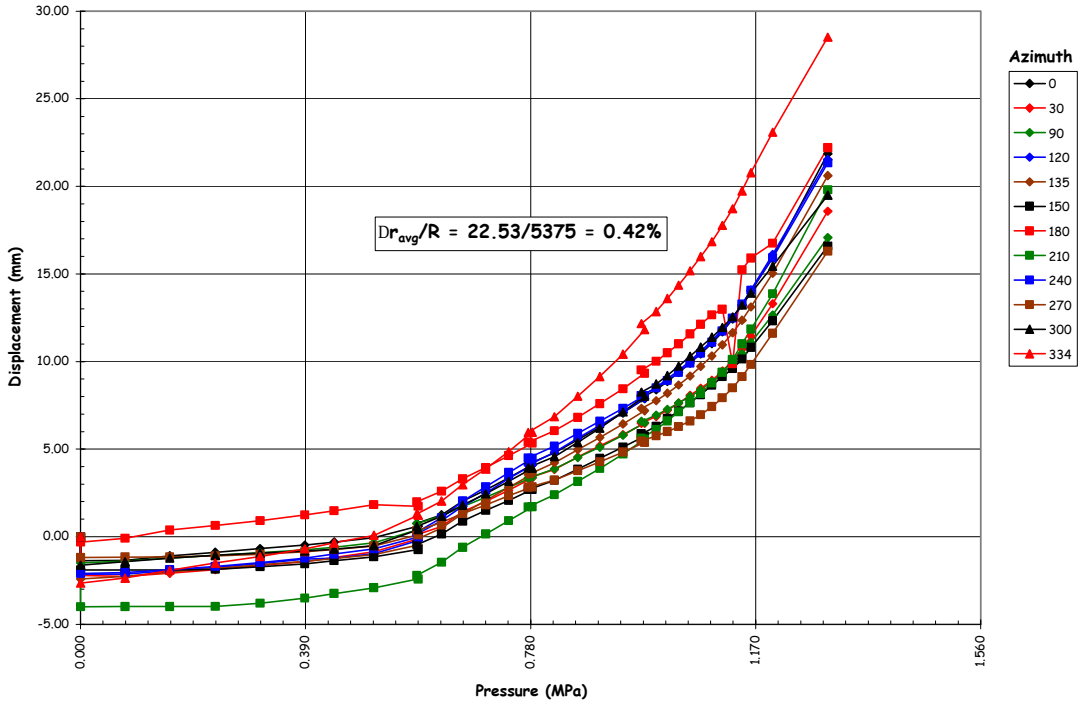

Figure 5.41 LST-Radial Displacement (DOR) at EL 4680

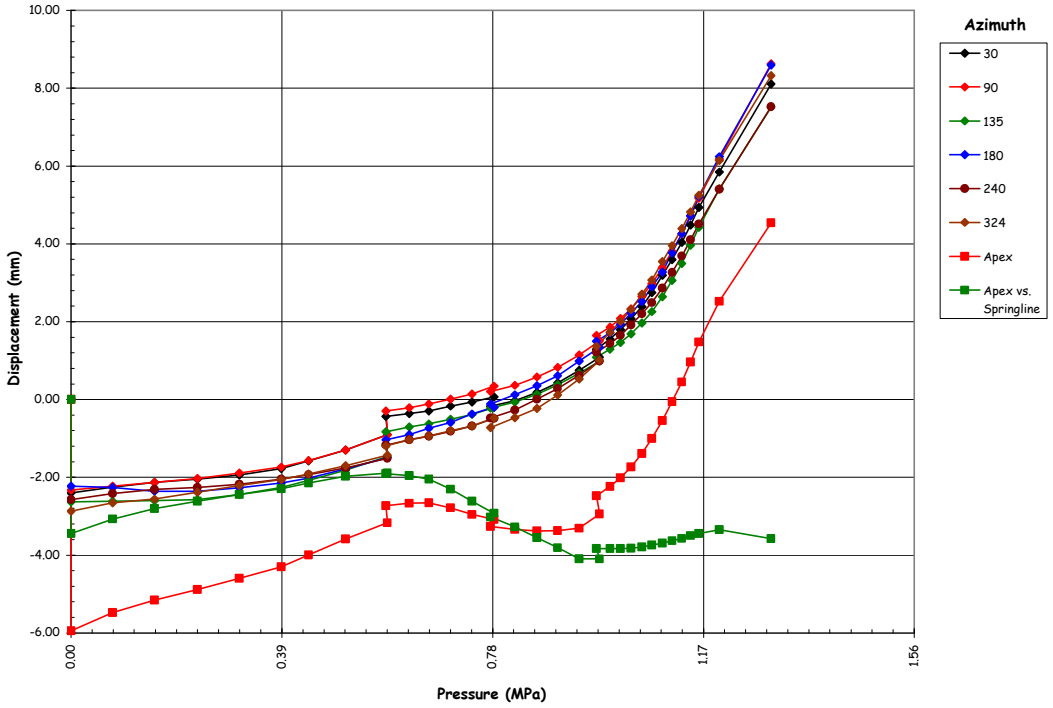

Figure 5.42 LST-Vertical Displacements (DOR) at Springline, El. 10750

The radial displacement of the model at the cardinal elevations along Azimuth 135 degrees, selected to represent the 'free-field' or axisymmetric response of the model, is shown in Figure 5.39. This plot illustrates several features of the response data that should be noted. The initial values (i.e. at P=0) reflect the inside surface motion of the liner between March 3rd and the start of the LST, thereby reflecting the influence of prestressing, changes in ambient temperature, creep, etc. The response due to pressure alone is the reported displacement minus the displacement at the start of the LST (i.e., at P=0 on 10:03 a.m., 26 September, 2000).

The initial data also suggests that the liner most likely separated from the concrete wall at some locations, as evidenced by the relatively large displacements that occurred during the first pressure step. At these locations, the first increment of pressure 'pushed' the liner back into contact with the concrete surface. This behavior can also be observed in the SFT and SIT/ILRT data, including a restoration of the gap after depressurization. The liner separation is most likely a result of differential thermal expansion and prestressing, resulting in compressive stresses that may have bowed or slightly buckled the liner.

The response remains essentially elastic up to 1.3 to 1.5 P_d, after overcoming the prestress (~1.2 P_d) and tensile cracking of the concrete. It is interesting to note that even though drying and shrinkage cracks were present prior to pressure testing, the onset of generalized concrete tensile cracking is quite distinct. Beyond 1.5 P_d to approximately 2 to 2.5 P_d, the response is still linear, although the loss of concrete tensile stiffness is quite distinct. Beyond 2.5 P_d, the response becomes increasingly nonlinear, particularly in the mid-section of the cylinder, as the model exhibits generalized yielding in the hoop direction.

The data also exhibits some apparent discontinuities at 1.5, 2.0, and 2.5 P_d. These apparent discontinuities coincide with the leak checks of the model and reflect, primarily, the response to changes in ambient thermal conditions over the time the model was isolated. The jump in displacement at 2.5Pd, however, most likely includes creep effects, since the temperature was stable over the relatively short (1-1/2 hour) hold at this pressure.

Figure 5.40 displays the displacements at Azimuth 324 degrees, which coincides with the centerline of the E/H. The largest radial displacement recorded during the LST, 33.36 mm, occurred at this Azimuth at El. 6200, above the E/H. Computing the equivalent hoop strain due to pressure at this location from kinematics,

$$@P_{max} = \frac{\Delta r}{R} = \frac{(33.36 + 2.68)}{5375} = 0.67\%$$

Similarly, calculating the local hoop strain in the vicinity of the equipment hatch at $2.5P_d$, corresponding with the onset of liner tearing and leakage, yields a value of approximately 0.28%.

Figure 5.40 again illustrates the liner separation phenomena, previously described, at elev. 9230. In this case the large magnitude of the displacement clearly indicates that the liner buckled. (A review of the post-prestressing data indicates that this occurred shortly after the completion of prestressing, most likely in conjunction with thermally-induced compressive strains.) This behavior did not, however, compromise the integrity of the liner and no tears were discovered at this location.

Figure 5.41 compares the displacement response as a function of Azimuth at elev. 4680, nominally the mid-height of the cylinder and the centerline of the E/H, A/L, and M/S penetrations. Ignoring some variation in initial conditions, reflecting some 'out-of-roundness' following prestressing, the response is fairly uniform, i.e. axisymmetric, except at 324 degrees, where largest deflections were already noted to occur. Averaging the radial deformation due to pressure yields a nominal average hoop strain of 0.42% at the peak pressure $3.3P_d$. Similarly, the average hoop strain at $2.5P_d$, coinciding with the onset of liner tearing and leakage, was 0.18%.

Figure 5.42 shows the vertical displacement of the springline at various azimuths. The vertical displacement at the apex and the differential displacement between the average springline displacement and the apex are also plotted. The vertical displacement exhibits similar behavior to the hoop displacements. In the vertical direction, however, the loss of stiffness due to concrete cracking occurs around 2.5 P_d. Yielding in the vertical direction does not appear to occur. This is due to the higher level of vertical prestress in the cylinder wall and the lower tensile forces induced by the pressure. The

vertical displacement is nearly uniform at the springline and the average meridional strain in the cylinder wall is less than 0.1%.

$$@P_{max} = 3.3P_d: \qquad \frac{\Delta l}{L} = \frac{(8.00 + 2.50)}{10750} = 0.10\%$$

The vertical displacements illustrate, much more dramatically, the effect of ambient temperature and creep during the leak checks.

Figure 5.42 also shows that beginning around $1.5P_d$, the dome apex deflects downward relative to the springline, most likely due to increasing force in the vertical tendons once the initial prestressing force is overcome by the pressure. (The vertical prestressing applies a compressive force on the cylinder wall approximately equal to the tensile force exerted by a pressure of $1.88P_d$.)

Deformed profiles of the PCCV model, constructed from the displacement data, are shown in Figures 5.43 through 5.45. These figures provide a more illuminating view of the model behavior than the pressure histories. The figures were constructed by applying the displacement data (exaggerated by a factor of 100) to the initial configuration of the model. The initial conditions were defined by the as-built model survey data (Appendix C). While these measurements were made in July, 1999, it was assumed that any changes in the position of the cardinal points by March, 2000 could be neglected without significant error. The motion of the cardinal points without displacement transducers were computed by linear interpolation. Both radial and vertical displacements were applied to the cardinal points and out-of-plane (i.e. circumferential) motion of the was not measured or considered.

The as-built position of the PCCV model is plotted along with the deformed shapes at the start of the LST (P = 0), at approximately $1.0P_d$ (0.398 MPa/57 psi), 2.0 P_d (0.776 MPa/113 psi), 2.5 P_d (0.978 MPa/142 psi), 3.0 P_d (1.162 MPa/169 psi), and 3.3 P_d (1.295 MPa/188 psi).

The figures illustrate a few interesting points about the behavior of the PCCV model.

First, and most importantly, the radial deformations are smallest at the buttresses (90 degrees and 270 degrees) and larger between the buttresses (0 degrees and 180 degrees), illustrating the stiffening effect of the buttresses even though the net hoop prestressing force is smallest at the buttress. The largest radial deformations are at the E/H and A/L penetrations, showing the reduced stiffness of these regions in spite of thickening and added conventional reinforcing. This reduction in stiffness is due to the lower prestressing forces as the tendons are deflected around the penetrations in addition to the opening itself.

Secondly, the vertical profiles do not show any reverse curvature at the wall-base junction and seem to imply the presence of a hinge forming at this location. While a hinge may have occurred, this deformation pattern may be more reflective of an instrumentation artifact than the model's behavior in this region. The displacement transducers at the wall-base junction were anchored to the base liner immediately adjacent to the wall, while the displacements above this point were measure relative to the instrumentation frame. It is likely that the differential displacement measured at the wall-base junction does not accurately reflect the total displacement in this region, and the data should be viewed with this limitation in mind.

Finally, a few other minor observations:

- The unusual deformation patter in the dome at 135 degrees and 324 degrees coincides with the regions where the East-West and North-South sets of vertical tendons overlap with the hoop tendons in the dome, where higher prestressing forces are present than in other regions of the dome.

- The initial buckling of the liner at Azimuth 324 degrees, elev. 9230 is clearly shown in Figure 5.44.

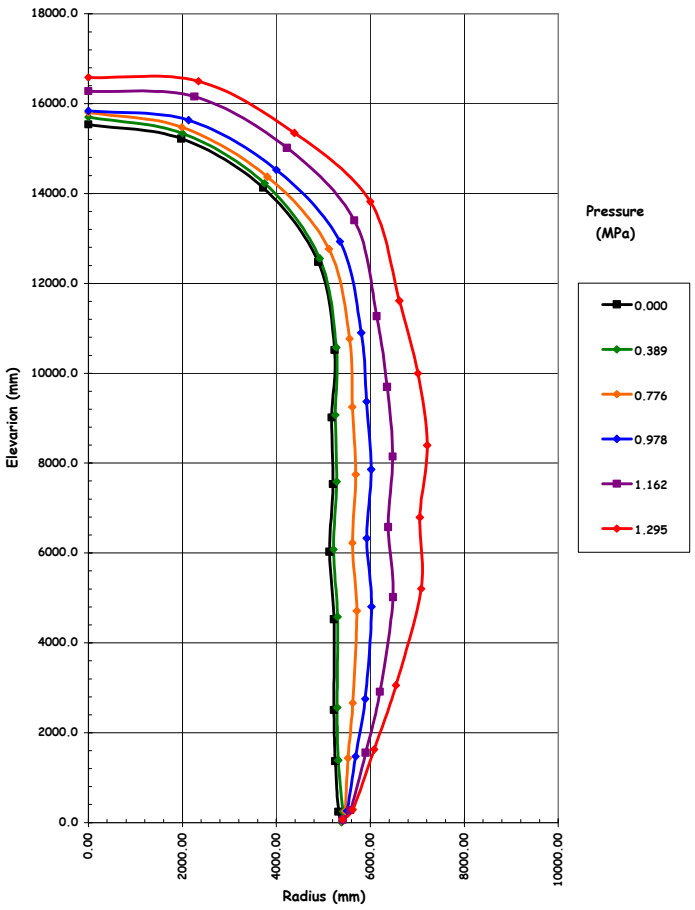

(90º)

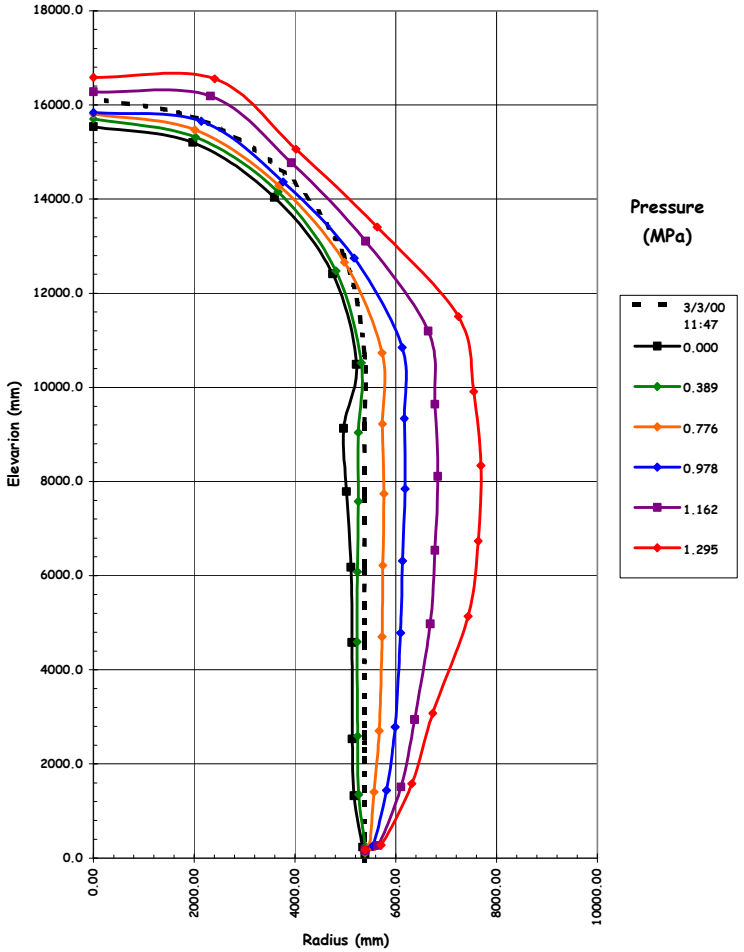

(135º)

Figure 5.43 LST - Deformation at Azimuth 90 degrees and 135 degrees (D and Z) × 100

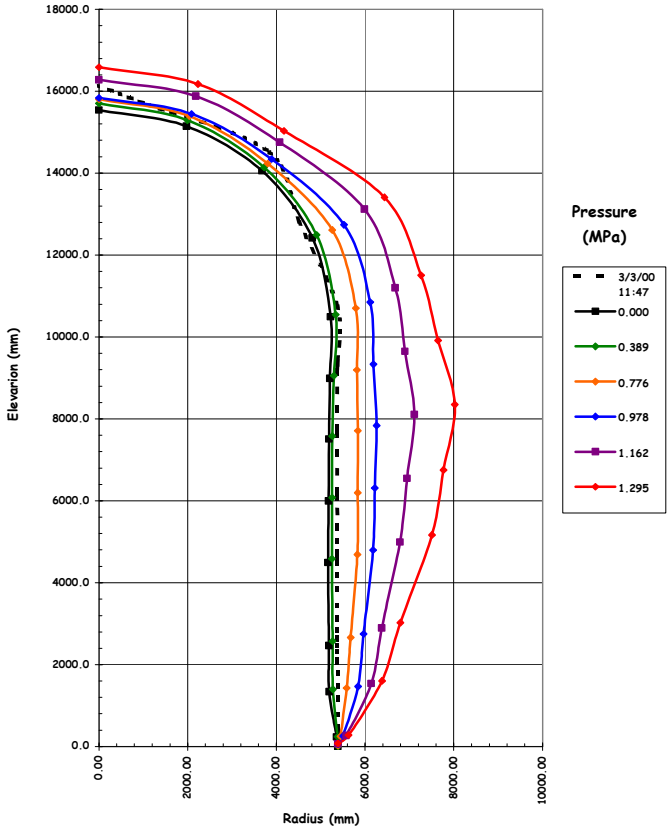

(240º)

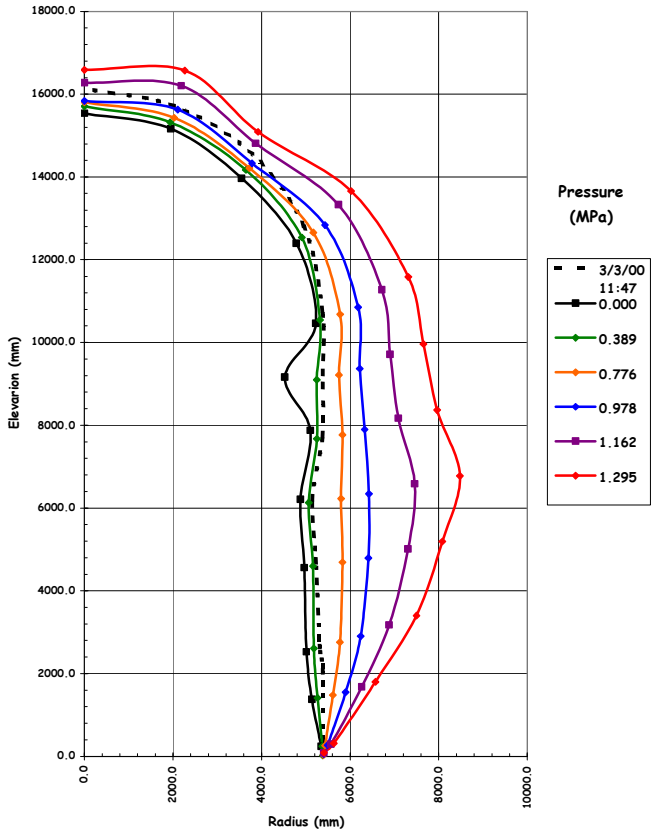

(324º)

Figure 5.44 LST - Deformation at Azimuth 240 degrees and 324 degrees (I and L) × 100

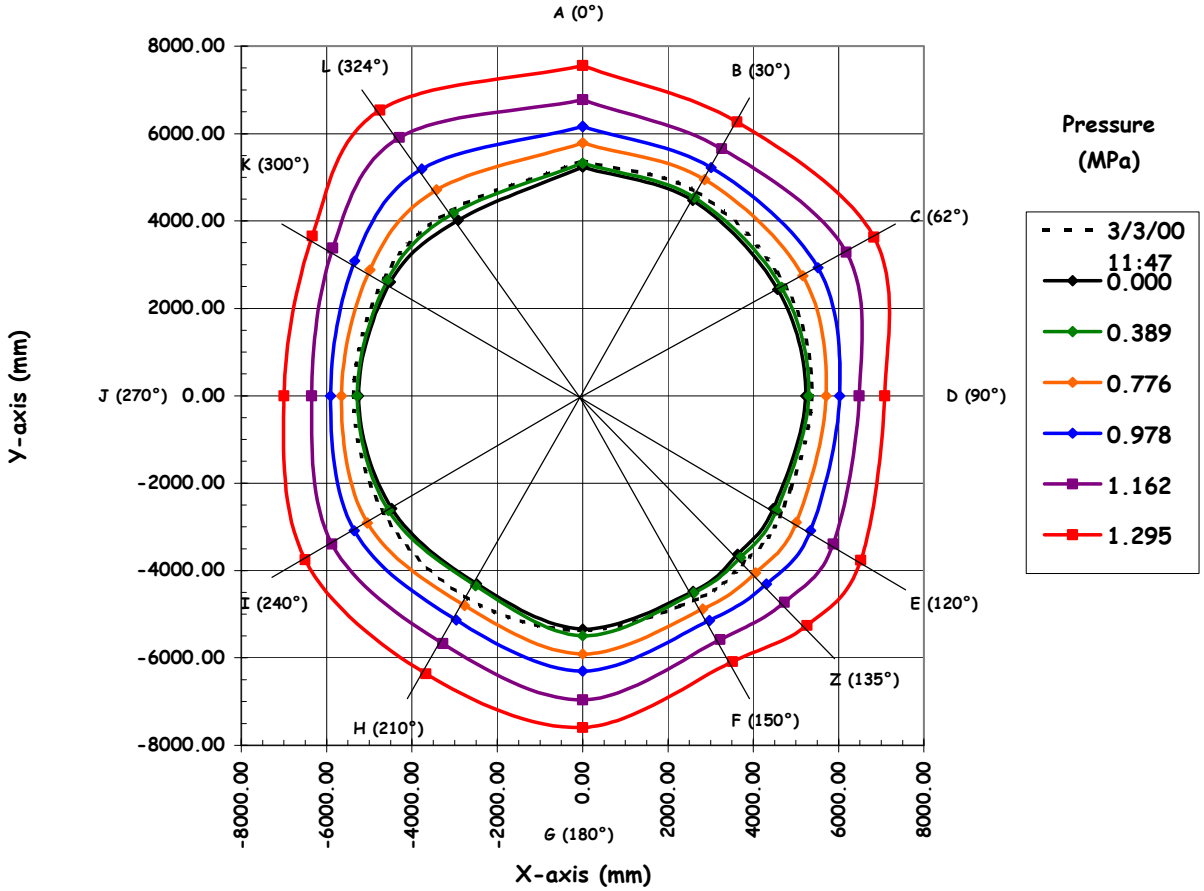

Figure 5.45 LST - Deformation at Elev. 4680 (5) × 100

5.3.2.1.2 Liner Strains

Five hundred and fifty-nine strain gages were placed on both surfaces of the liner to measure both the meridional and hoop free-field liner strains, as well as local strains at the penetrations, the wall-base junction, liner anchor, and stiffeners where discontinuities might result in high local strains prior to the liner tearing. The data for each of these gages is provided on the enclosed CD. The majority of these gages did not record significant strains, however, gages at a number of locations deserve closer inspection. Table 5.4 summarizes the maximum strains recorded during the LST at locations of interest.

Before considering several of these locations in detail, it is worth noting that individual strain gages can provide misleading information due to their sensitivity to local as-built conditions, particularly in areas of sharp discontinuities and high strain gradients. As a result, it is more meaningful to consider sets of gages in these locations, thus providing a more realistic view of the strain field in a particular area.

Figure 5.46 shows all the free-field liner hoop strain gages that exceeded 0.5% at the end of the test. It is interesting to note that up to 2.5 Pd, the free-field liner strain hoop strains were almost all below 0.2%, which compares favorably with the average hoop strain computed from the displacements, 0.18%.

Nearly all the free-field liner and liner anchor meridional strain gages were below 0.1%, which is also consistent with the displacement data.

Considering the liner strains near penetrations and other discontinuities, the strains in the vicinity of the E/H are of primary interest since there were indications during the LST that the liner initially tore in this region. Posttest inspection of the liner, described in Section 5.3.2.2, revealed several tears at the edges of the embossment (Figure 5.47), but no apparent damage near the insert plate. The layout of the liner strain gages is shown on Drawing D-SN-P-218 (Appendix E), and reproduced in Figure 5.48 for reference. The highest strains in this region were at the left and right edges of the embossment. The strains adjacent to the insert plate (#19 to #67) were small, nearly all less than 0.2% at maximum pressure, with only a few near the ends of anchors or stiffeners reaching 0.5%.

Table 5.4 LST Liner Strain Summary

Maximum Free-Field Hoop Strain	0.90%
Maximum Free-Field Meridional Strain	0.14%
Maximum Meridional Anchor Strain	0.10%
Maximum Equipment Hatch Strain	3.88%
Maximum Personnel Airlock Strain	0.75%
Maximum Main Steam Penetration Strain	4.54%
Maximum Feedwater Penetration Strain	6.39%
Maximum Wall-Base Junction Strain	1.97%
Maximum Miscellaneous Liner Details Strain	5.75%

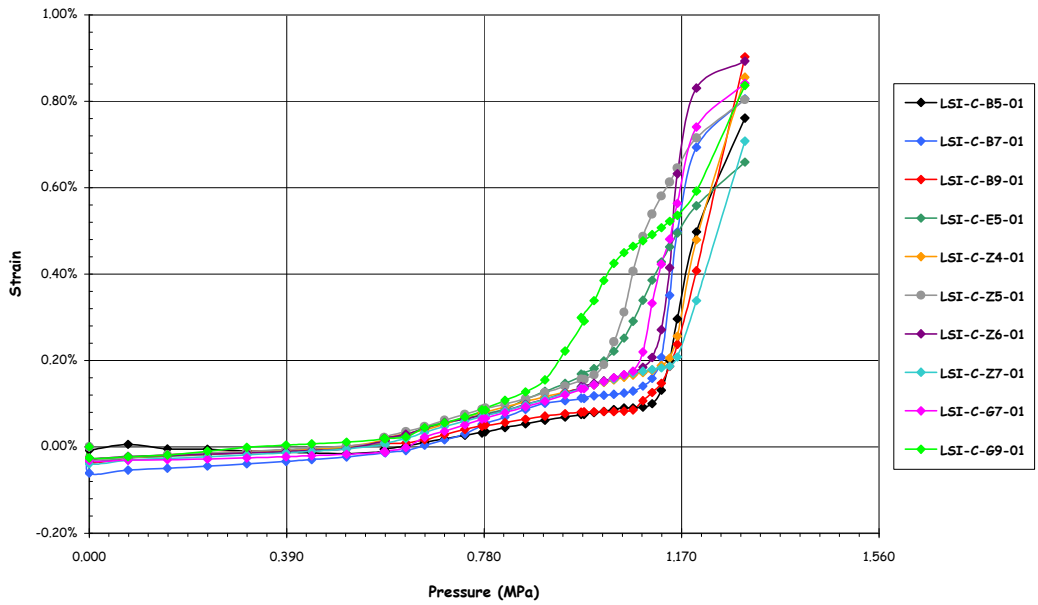

Figure 5.46 LST – Free-Field Liner Hoop Strains

Figure 5.47 Liner Tear (#15) at E/H

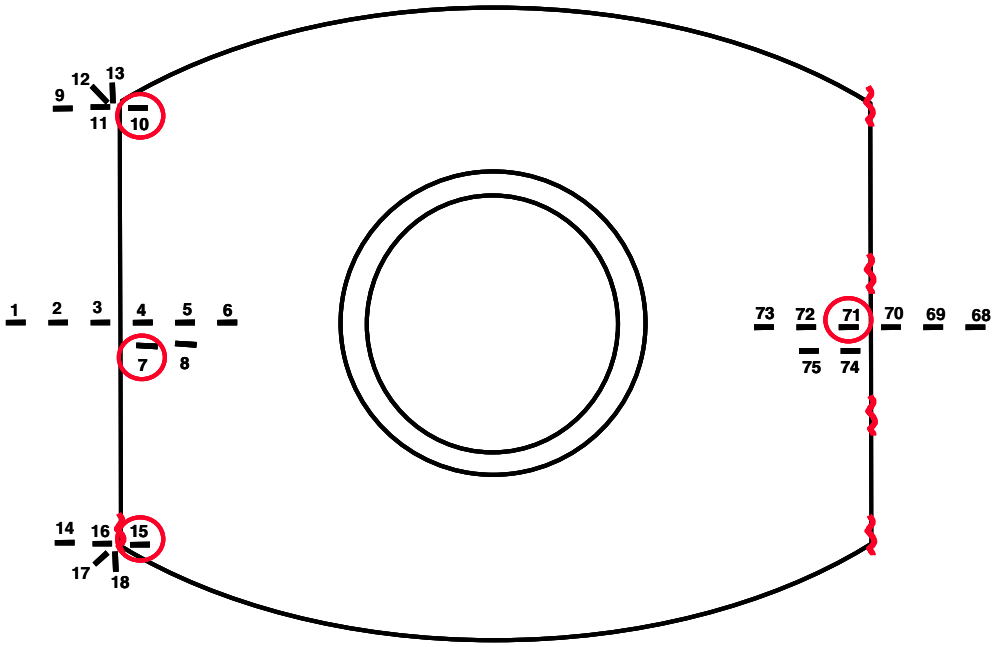

Figure 5.48 Equipment Hatch Liner Strain Gage Layout (Inside View)

The strains at the middle of the 'left' (#1-8) and right (#68-75) edges of the embossment are shown in Figures 5.49 and 5.50. The strains at the upper and lower 'left' corners are shown in Figure 5.51. With the exception of gage #7, the strains at the mid-sides of the embossment are all very small until global yielding of the model occurs just below $3P_d$. At the corners, however, liner strains begin increasing earlier, with gage #10 showing increasing strains beginning at 1.5Pd, while most of the other gages show significant increases beginning at 2.5Pd, when liner tearing was believed to

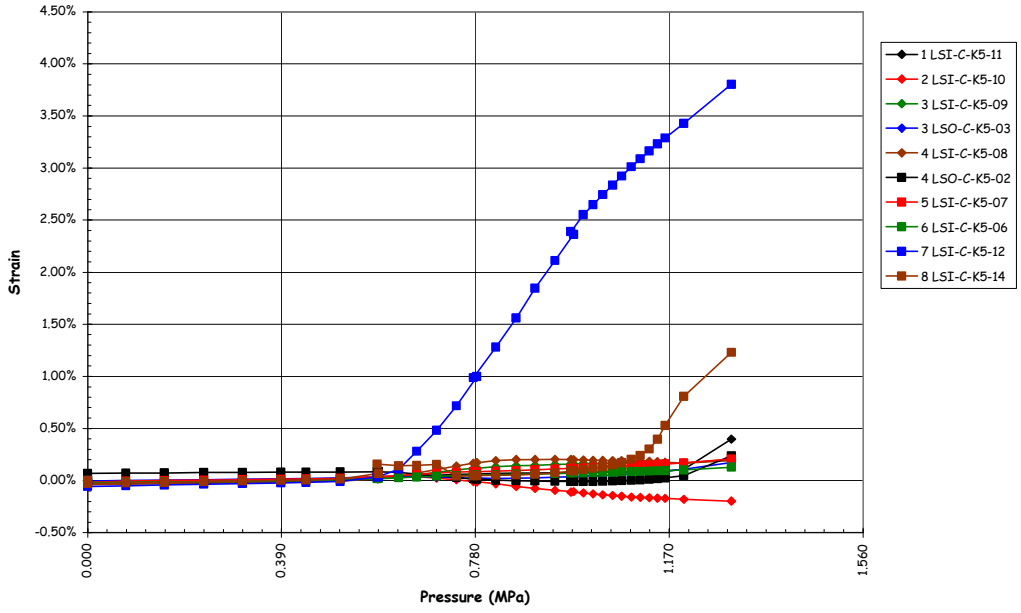

Figure 5.49 E/H Liner Strains at 'Left' Edge of Embossment

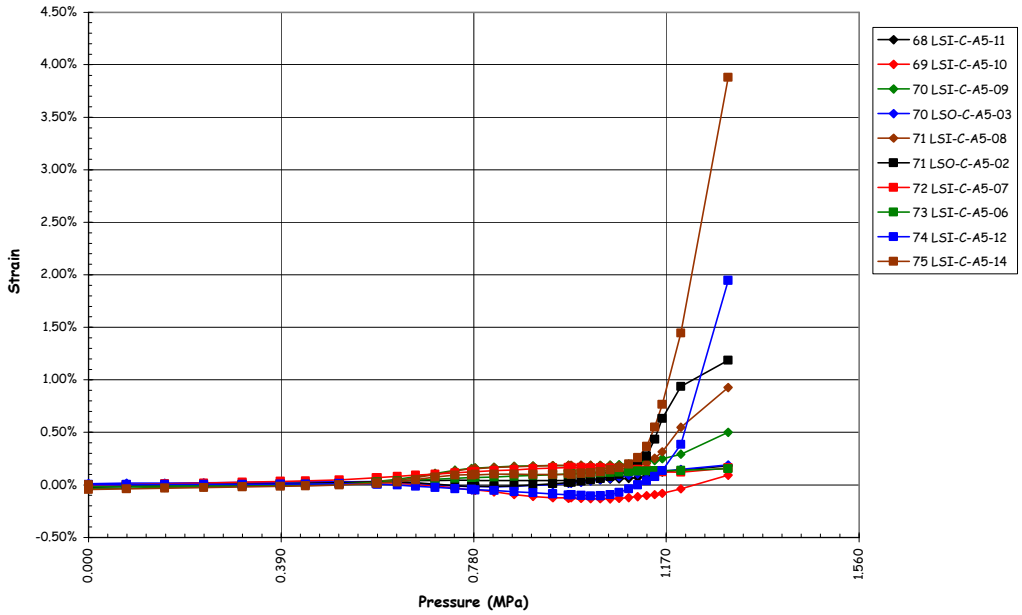

Figure 5.50 E/H Liner Strains at 'Right' Edge of Embossment

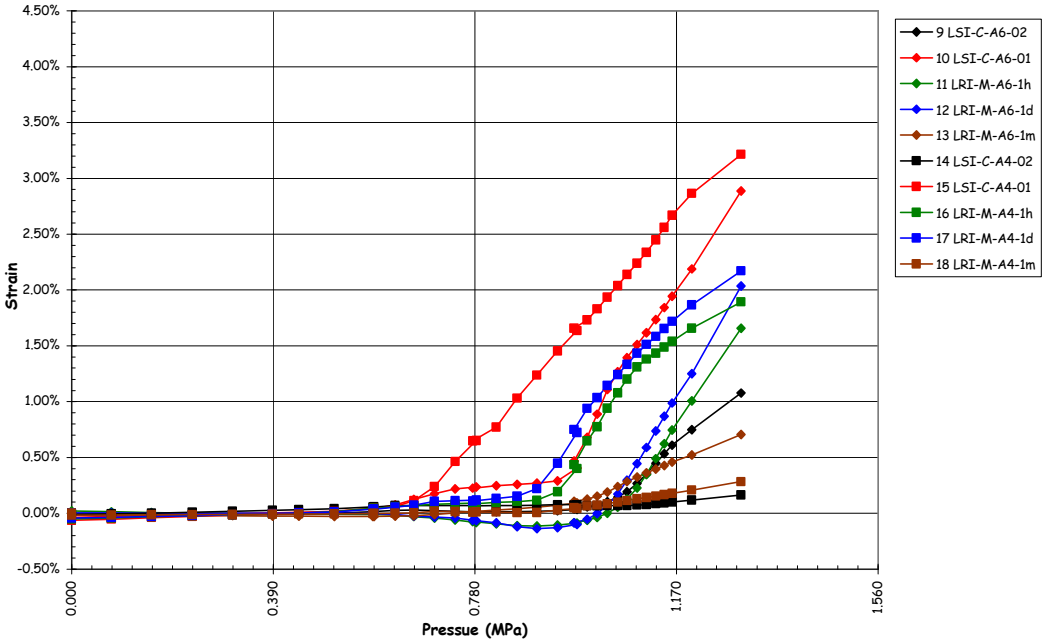

Figure 5.51 E/H Liner Strains at 'Left' Corners of Embossment

have occurred. At first glance, it appears unfortunate that the liner tore on the opposite side from the strain gages (pretest analyses suggested the highest strains would occur or the 'left' side). However, it has been found that strain gages near tears often see lower strains than would be expected, since the tear acts as a strain relief mechanism. While it is apparent that the strains on the 'right' side were higher, it is unlikely that gages at those locations would have recorded higher strains than those on the left side. This is demonstrated by comparing gages #7 on the left and its mirror image, #74, on the right.

Note that at the pressure 2.5 P_d, when the liner tearing is believed to have begun, the measured strains were only on the order of 0.75% to 1.50%.

The liner strain at the A/L shows a similar pattern to those at the E/H, with a peak tensile strain at the corner of the embossment of 0.75%. However, no tears occurred at this penetration.

Liner strains at the M/S and F/W penetrations are shown in Figures 5.52 and 5.53. The layout of the liner strain gages is shown on Drawing D-SN-P-220 (Appendix E).

Several large tears occurred at each end of the F/W penetration, beginning at the weld between the thickened insert plate and the liner; however, no tears occurred at the M/S penetration event, though the free-field hoop strains at the M/S are higher since it is closer to the mid-height of the cylinder. There are a number of reasons why this occurred, primarily liner fabrication issues discussed in Section 5.3.2.2. It is interesting to note that even though the strain gages at the F/W penetration were located near the tear (see Figure 5.54), measured strains were relatively low until the very end of the LST, when some strains increased very rapidly. This might indicate that a tear in the vicinity of a strain gage can act as a strain relief mechanism on the surrounding material. The 'jump' in the strain near the end of the test may also be due to material distortion in the vicinity of the tear as the tear propagated. On the other hand, the strains recorded at the M/S penetration begin to climb rapidly at 2.0 to 2.5 Pd, reaching values as high as 4.5% without resulting in any liner tearing. Detailed inspections of this location did not reveal any evidence of the fabrication problems that were present at the F/W penetration.

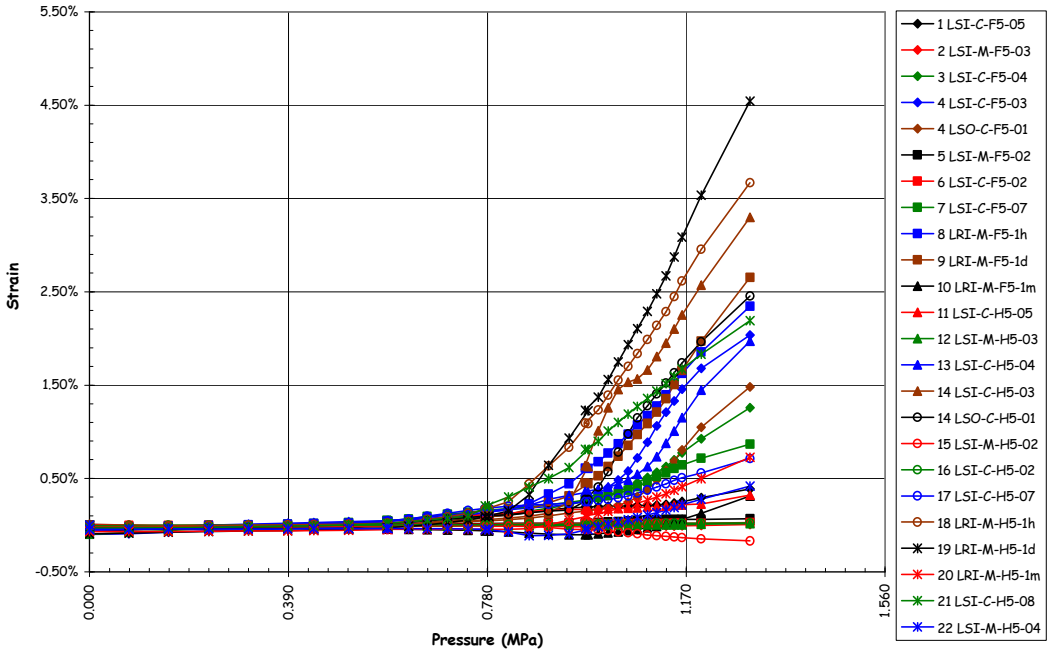

Figure 5.52 Liner Strains (DOR) at M/S (Ref. D-SN-P-220)

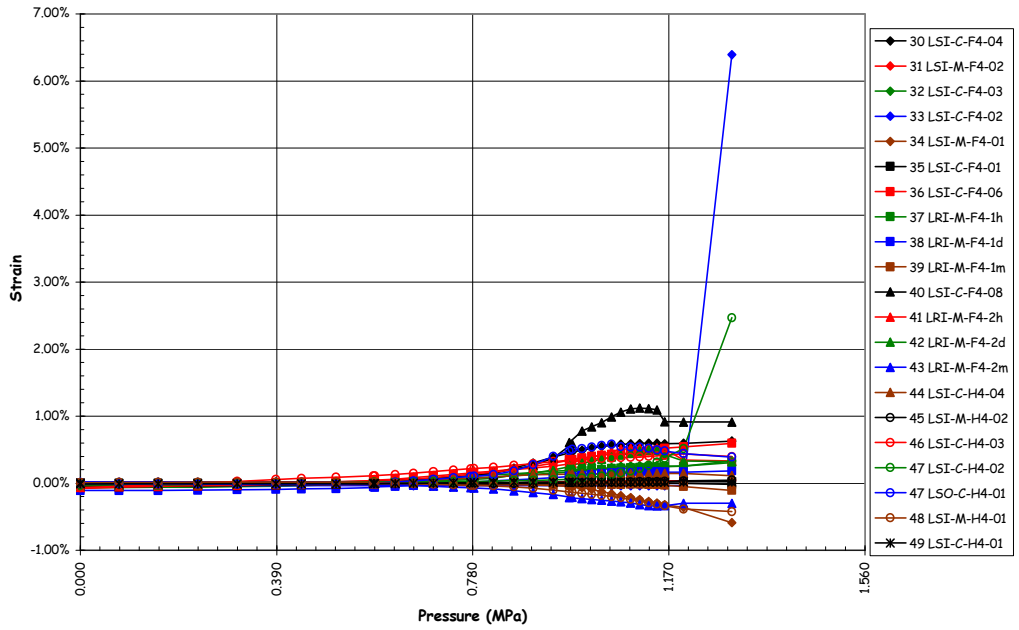

Figure 5.53 Liner Strains (DOR) at F/W (F=Ref. D-SN-P-220)

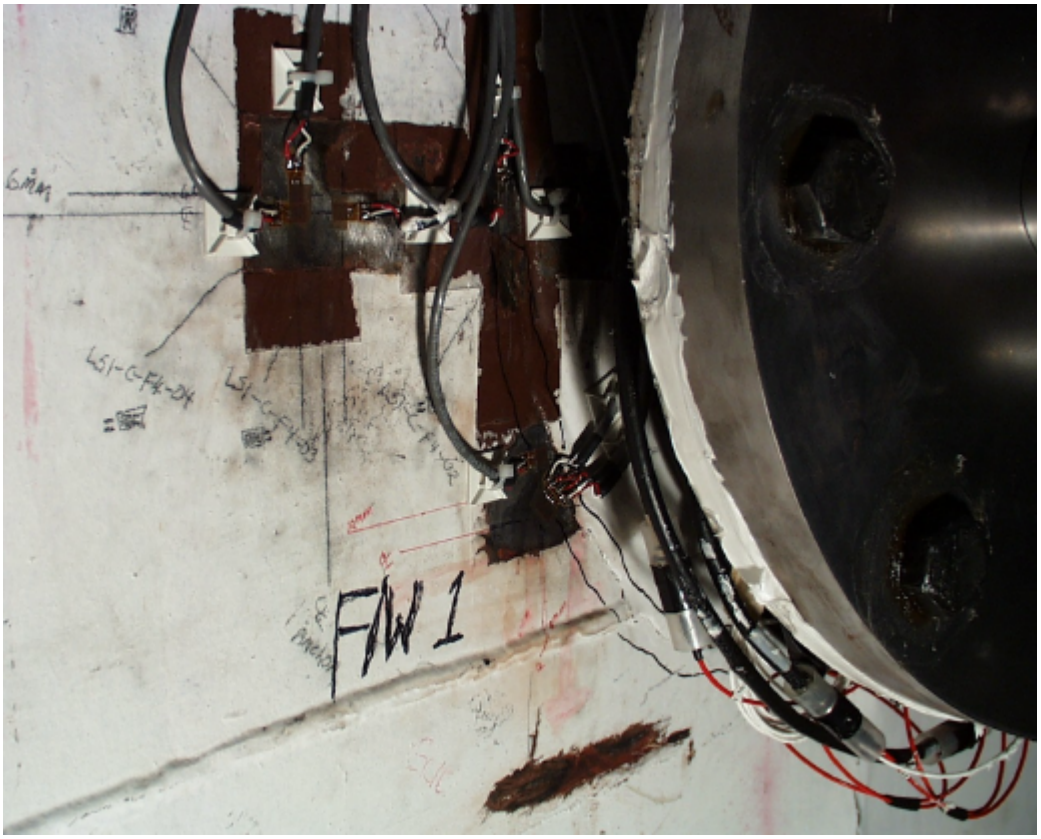

Figure 5.54 Liner Tear (#3) and Strain Gages at F/W Penetration

A number of other details believed to create potential strain concentrations in the liner were also instrumented and monitored during the test. One of these details occurs throughout the model: a gap is left in a horizontal stiffener or vertical anchor where it crosses a liner seam wells (Figure 5.55), euphemistically called a 'rathole.' In previous containment model tests, this detail caused significant strain concentrations when the surrounding liner began to yield. In fact, a number of the liner tears found after the test occurred at these details. One such detail that was instrumented was located near the intersection of cardinal lines D7 (Azimuth 90 degrees, elev. 7730). Although a tear occurred in a similar detail above this location, the liner did not tear at this rathole and the strains recorded at this location provided valuable information regarding the behavior of this detail for comparison with analyses.

The interior strain gages at D7 are also shown after the LST in Figure 5.56. The arrangement of these gages is shown on Drawing D-SN-P-209, Detail a.4 (Appendix E). Strains begin increasing between 2.0 and 2.5Pd, reaching a maximum of 5.7% at the maximum pressure. Nevertheless, the liner did not tear. A subsequent comparison of this detail to similar rathole details that did tear, but were not instrumented, revealed a lack of any weld repairs, which was not true of the other locations. This detail appears to demonstrate that the liner is capable of undergoing significant local strain without tearing in the absence of any other factors that might degrade the liner.

5.3.2.1.3 Rebar and Concrete Strains

The reinforcing steel strains are summarized in Table 5.5. Typically, after the onset of global yielding, the rebar strains were higher than the corresponding strains computed from displacements and the free-field liner strains. This phenomena was recognized during gage calibration and occurs due to a local reduction in cross-section from grinding away a portion of the bar to mount the strain gage. The effect of this local cross-section reduction causes the bar to yield at the gage location slightly before the rest of the bar yields. The effect on the rebar strain readings is to introduce an artificial strain increment, on the order of 0.5% strain, after the bar has yielded, compared to the strain that would occur if the gage were not present. This artifact can be illustrated by considering the hoop strain measurements at Z6 shown in Figure 5.57. Attempts were made to develop an algorithm to correct for this gage artifact; however, the results were not particularly useful. The rebar strain data included on the data CD were not corrected for this artifact, which any interpretation of this data should consider.

Figure 5.57 compares the hoop strains recorded at the mid-height of the cylinder wall (Z6: Azimuth 135 degrees, elev. 6280) by the fiber optic gages (CE), rebar strain gages (RS), liner strain gage (LI) and computed from the displacement (DT). The strains track each other very well until local yielding occurs in the liner and, shortly after, in the rebar. The fiber optic gage continues to track the displacement and provides a much more accurate measure of the hoop strain in the wall than the LI or RS gages.

Figure 5.55 Horizontal Stiffener Detail at Vertical Seam Weld ('Rathole') near D7

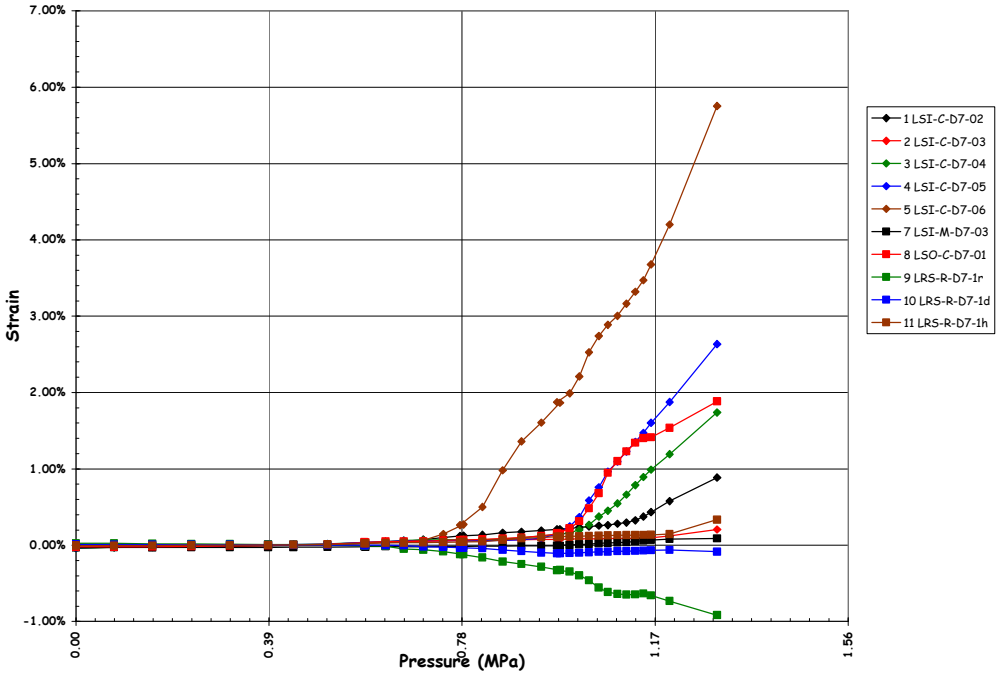

Figure 5.56 Liner Strains (DOR) at D7 Anchor Detail (Ref. R-SN-P-209, a.4)

Table 5.5 Rebar Strain Summary

Maximum Free Field Hoop Rebar Strain	1.68%
Maximum Free Field Meridional Rebar Strain*	0.47%
Maximum Free Field Radial Rebar Strain	0.88%
Maximum Basemat Rebar Strain	0.84%
Maximum Rebar Strain at E/H	1.62%
Maximum Rebar Strain at A/L	1.50%

* One gage (RS-M-A0-07) recorded a maximum strain of 6.11%. However, the initial strain of the start of the LST was 5.85%, yielding a change in strain of 0.27%. The initial high strain reading was due to an increase in resistance not associated with strain of the bar.

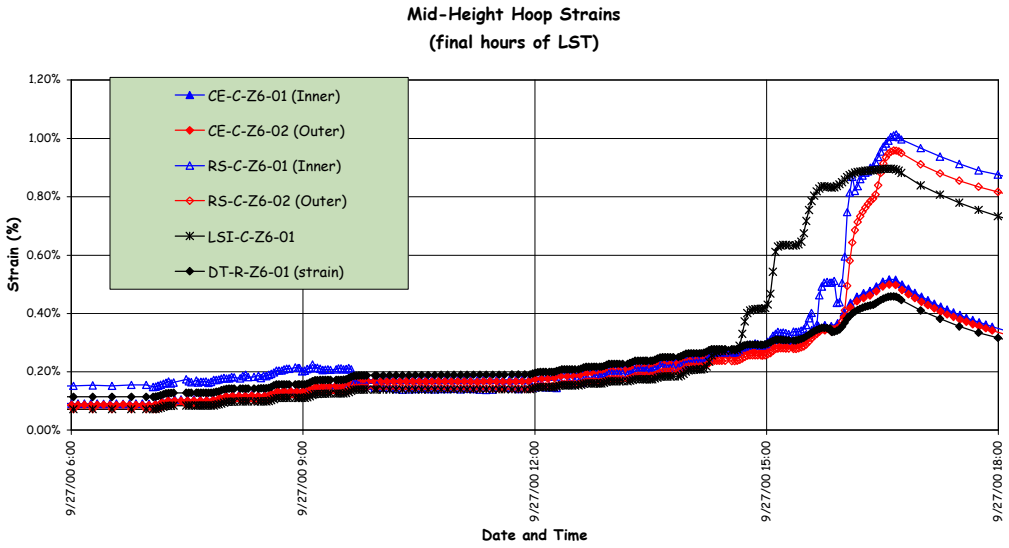

Figure 5.57 Comparison of Strain at Z6 (Azimuth 135 degrees, Elev. 6280)

Strain gages were also installed on specially fabricated 'gage bars,' which were located at several azimuths (90 degrees, 135 degrees and 350 degrees) at the wall-base junction in an attempt to get a more accurate picture of the strain fields at this location due to the presence of large bending forces under pressure (Figure 5.58). Unfortunately, a large number of these gages were damaged during construction and only very limited data was obtained. (Since the gage bars were embedded in the basemat, they were placed at the time of the final basemat lift and left exposed for almost two years until the first cylinder wall lift was placed. During this time, they were exposed to the weather and some rough handling by the construction workers.) However, enough gages survived at 135 degrees that it is possible to construct a picture of the strain history at this location. Figure 5.59 shows the distribution of strain *due to pressure only* at four elevations (86, 201, 312, and 427) above the top of the basemat. Only the strain due to pressure is plotted, since the initial strains due to dead load and prestressing are somewhat ambiguous and mask the pressure response. The strains recorded by the surviving gages at each elevation are plotted at pressure levels corresponding to $1P_d$, $2P_d$, $2.5P_d$, $3P_d$, and $3.3P_d$. While these results are incomplete, they do show the increasing curvature of the cross-section as a function of pressure, especially at elev. 427.

Some gage bars were also located in the basemat, above the tendon gallery, in an attempt to measure tensile strains that might develop at this location. However, there was no indication of any damage in this region and, with a few ambiguous exceptions, the gages did not record any response to the pressure loads.

Overall, in spite of the significant effort (and expense) involved in the application and installation of the rebar strain gages, the resulting data is only marginally useful and any future tests of a similar nature would be advised to consider the method of installing strain gages on rebar and to limit the number of gages to a few, critical locations.

5.3.2.1.4 Tendon Forces and Strains

Since the unique feature of this model, compared to previous large-scale containment models tested at SNL, is the prestressing system, and the behavior of this system to pressure loads beyond design levels is of particular interest, a significant effort was made to measure the response of the tendons. Both tendon anchor forces, as well as strains along the length of the tendons, were measured. Unfortunately, as noted in Chapter 2, approximately 50% of the strain gages installed on the tendons strands were damaged during construction and/or prestressing. Furthermore, data from the Tensmeg gages indicates the likelihood that these gages de-bonded or slipped relative to the tendon strands, casting some doubt on the accuracy of the data.

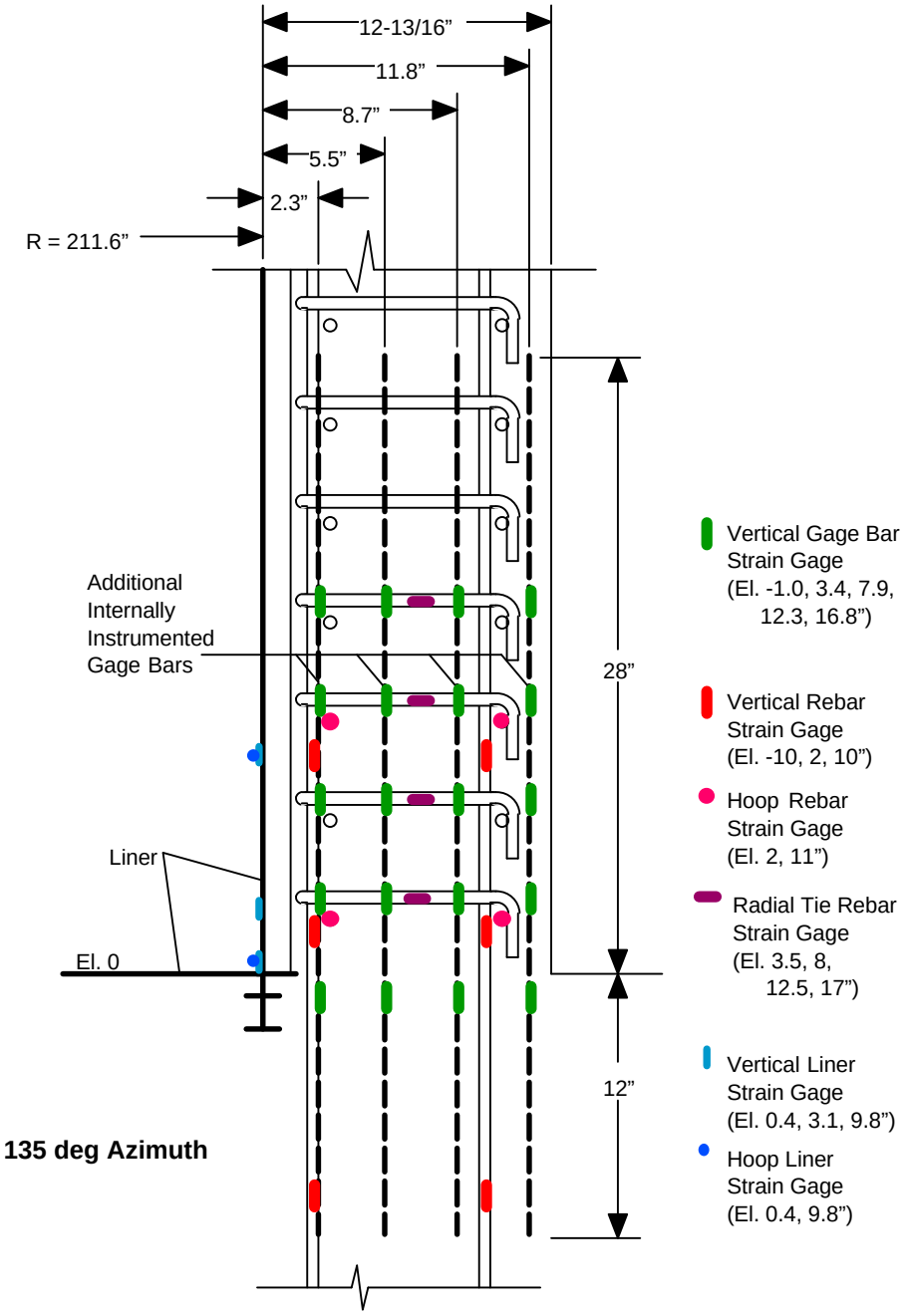

Figure 5.58 Arrangement of Gage Bar Strain Gages at Azimuth 135 degrees

Nevertheless, the surviving gages provide some significant insight into the response of the tendons to the pressure loading. All of the tendon data (load cells and strain gages) is provided on the enclosed CD, as described in Section 5.3.1. A summary of the data and a discussion of the LST results follows.

One-sixth of the tendons in the model were equipped with load cells at each anchor prior to prestressing. Figures 5.60 through 5.62 illustrate the tendon anchor forces during the LST. The anchor forces for the vertical tendons with load cells are shown in Figure 5.60. The anchor forces are shown for the maximum tensioning force during prestressing, after the completion of prestressing (on 5/4/00) and during the LST at $0.0P_d$, $1.0P_d$, $2.0P_d$, $2.5P_d$, $3.0P_d$ and at maximum pressure, $3.3P_d$. Similarly, Figures 5.61 and 5.62 show the anchor forces for the hoop tendons anchored at the 90 degree

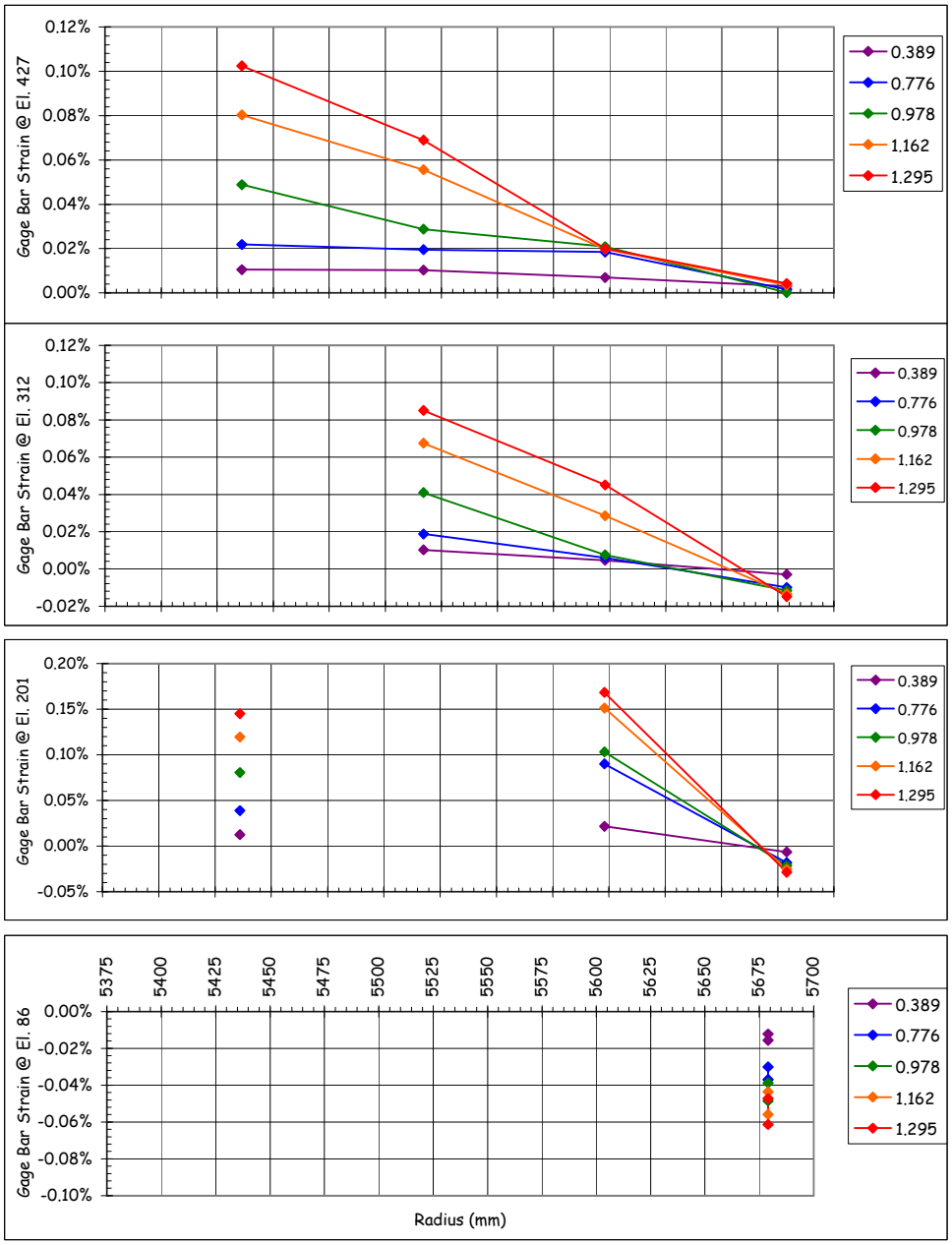

Figure 5.59 LST Gage Bars Strains at Azimuth 135 degrees (due to pressure only)

and 270 degree buttresses. In general, the vertical tendon anchor forces did not exceed the initial tensioning force. The average vertical tendon force at the peak pressure of $3.3P_d$ was 466 kN (104.7 kips) compared to the average tensioning force of 472 kN (106.3 kips). The hoop tendon anchor forces, however, did exceed the initial tensioning force of 424 kN (95.3 kips). The maximum anchor force recorded at the peak pressure of 3.3 Pd was 550 kN (123.64 kips) for tendon H53. The average anchor force for all the hoop tendons at the peak pressure was 496 kN (111.6 kips). The tendon yield strength (0.2% offset) is approximately 590 kN (132.6 kips), so hoop tendon forces at the anchors were approaching, but had not exceeded their yield strength.

Eight tendons, five hoop tendons (H11, H35, H53, H67, and H68) and three vertical tendons (V37, V46, and V85), were instrumented along their length by placing strain gages on individual strand wires at specified locations. The surviving bonded foil gages are believed to have provided the most reliable data on the strain in the tendons. Figure 5.63 plots the strain history during the LST of the surviving gages on tendon H68. This plot illustrates the variability between strains in different strand wires at roughly the same position along the tendon. Nevertheless, considering an average strain of approximately 0.40% at the start of the LST, the increase in the average strain to 0.80% is nearly identical to the average hoop strain computed from the displacements, at 0.42%.

A more useful way of analyzing the tendon response data is by constructing the tendon force profiles at pressures during the LST, similar to the force profiles constructed for the prestressing loads (see Figures 2.66-2.73). The tendon force profiles for the five instrumented hoop tendons are shown in Figures 5.64 to 5.68. The force profiles include the design and measured values at maximum tension and after seating, and the recorded response during the LST at 0.0 P_d, 1.0 P_d (0.389 MPa/56.4 psi), 2.0 P_d (0.776 MPa/112.5 psi), 2.5 P_d (0.978 MPa/141.8 psi), $3.0P_d$ (1.162 MPa/168.5 psi), and at the maximum pressure, 3.3 P_d (1.295 MPa/187.8 psi). The profiles are also shown during depressurization at approximately $2.5P_d$, $2.0P_d$, $1.0P_d$, and $0.0P_d$. These force profiles were constructed by converting the average strain from all the foil strain gages at a given position to a force using the actual tendon force-strain test data and combining the computed forces with load cell data. When only a single strain gage survived at a given position, it is noted on the profile.

There is not adequate data to assume the shape of the hoop tendon force profile between the surviving measurement positions, so only the force at the measurement locations are shown. There is enough data to suggest, however, that the tendon force distribution tends to become more uniform, with the largest increase in strain occurring near the mid-point of the tendon, where the initial prestressing force was the smallest. This may be due to a combination of local yielding and/or slipping as the tendons try to maintain equilibrium and local deformation of the cylinder wall. Comparing the differential strain at the midpoint of the tendons to the hoop strain calculated from the wall displacement at that location (see Figures 5.66 and 5.67) indicates that the tendon strain is greater than what would be expected if the tendon did not slip relative to the wall. After unloading, however, the initial tendon force profile (at the start of the LST) is almost completely recovered, which implies that any redistribution occurring during the LST is entirely elastic. This is not a completely satisfying observation, since it would seem likely that any redistribution of tendon forces due to slipping would remain after depressurizing. This reinforces the observation that the change in tendon forces is also due to the local elastic deformation of the wall.

The force profiles for the vertical tendons, constructed in the same manner as the hoop tendon profiles, are shown in Figures 5.69 to 5.71. Again, since the gage mortality was lower for the vertical tendons than the hoop tendons and the force profile is more nearly a continuous function, curves were fit through the data to facilitate interpretation and comparison of the data with the design assumptions. The data again shows that the vertical tendon force distribution becomes more uniform as the pressure increases, and the largest relative increase occurs at the mid-point of the tendon, i.e. the apex, for the vertical tendons. This suggests that the tendons must slip relative to the concrete wall to allow the forces to redistribute; however, as with the hoop tendons, recovery of the initial tendon force distribution is nearly complete after depressurization. In this case, however, it is difficult to argue that the tendon force distribution is dominated by the local radial deformation of the concrete wall/dome, since those in the dome are much smaller than those in the cylinder wall, which is inconsistent with the observed change in the force distribution.

While the tendon response measurements provided new insight into the behavior of unbonded tendons under limit load conditions, some apparent paradoxes were identified that might be answered by further testing and analysis. One conclusion is apparent and undeniable, however. The change in tendon anchor forces is not a reliable indicator, by itself, of the change in force along the length of the tendons, and any attempts to preclude tendon rupture by measuring only the anchor force will not be adequate.

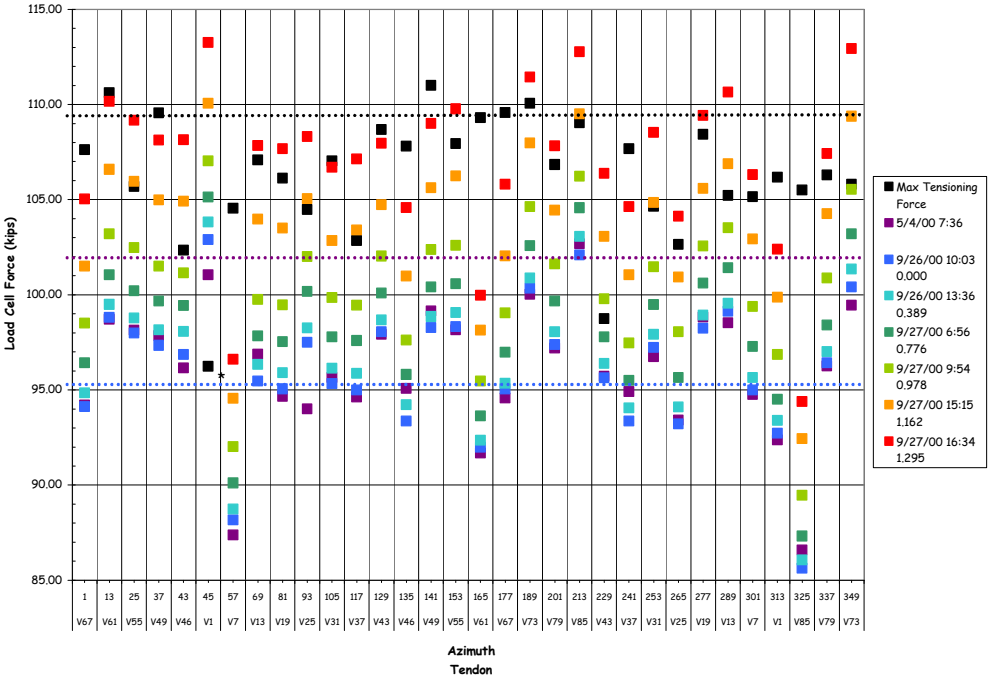

Figure 5.60 LST - Vertical Load Cells

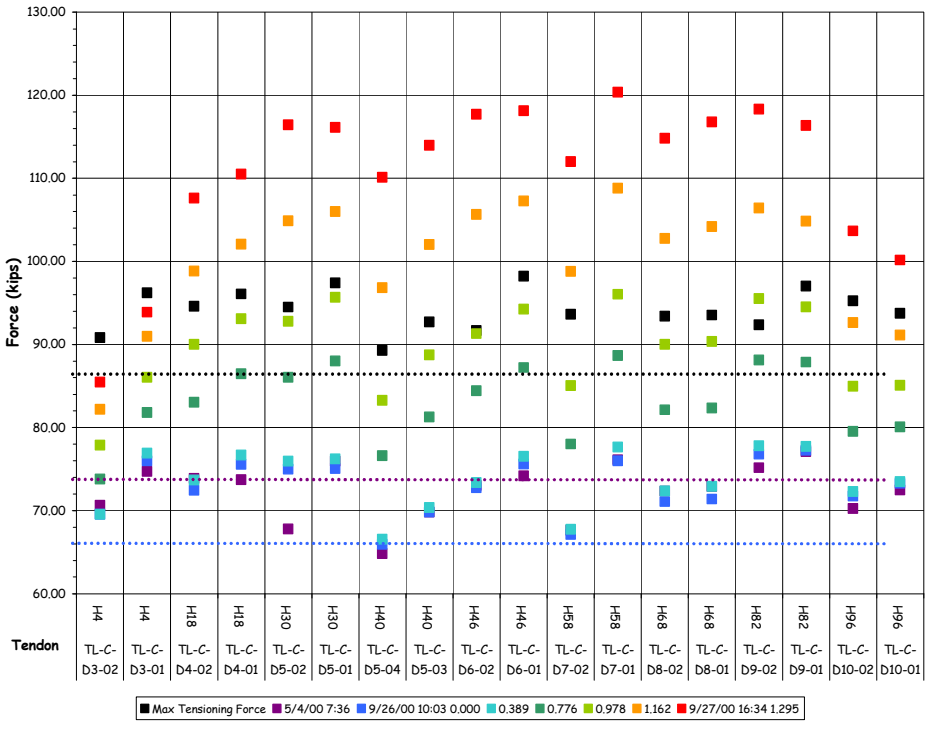

Figure 5.61 LST - Hoop Load Cells at 90 degrees

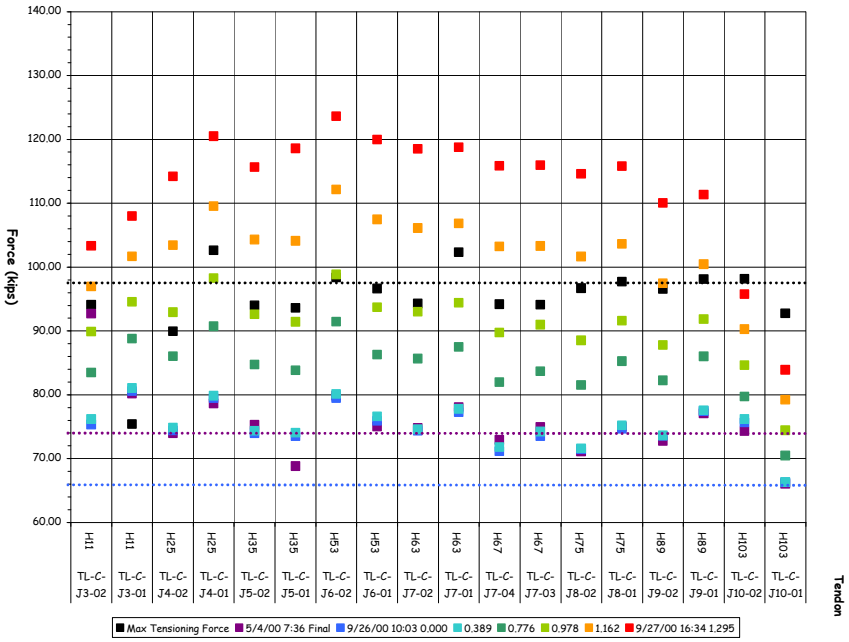

Figure 5.62 LST - Hoop Load Cells at 270 degrees

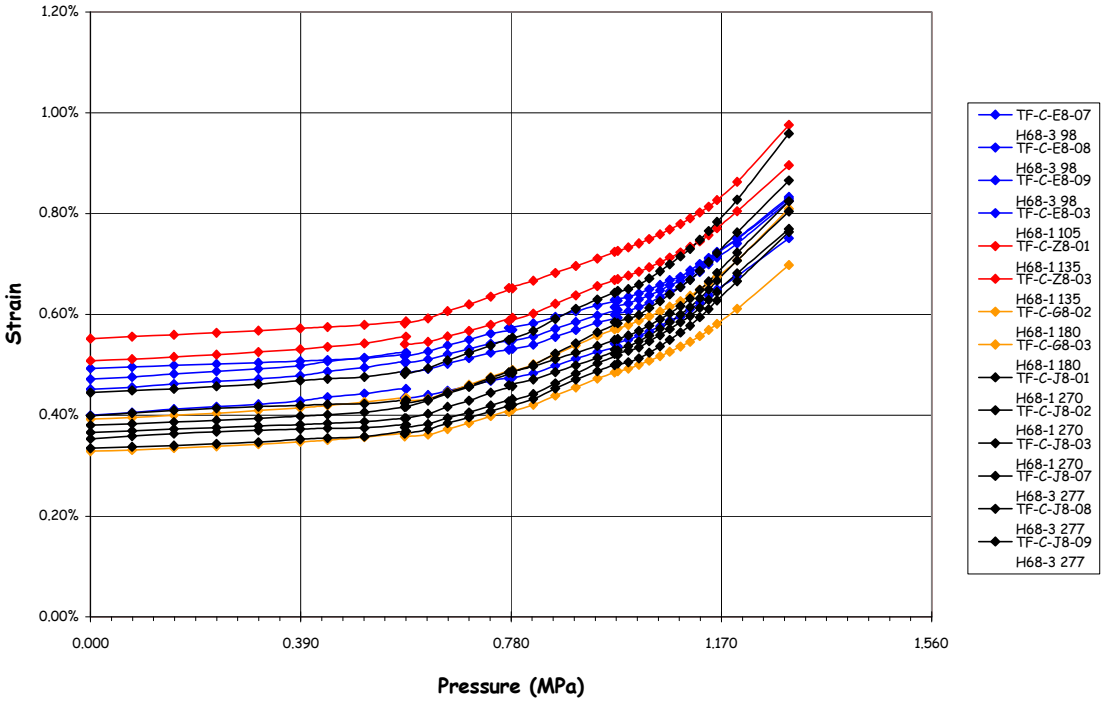

Figure 5.63 LST - H68 Tendon Strains

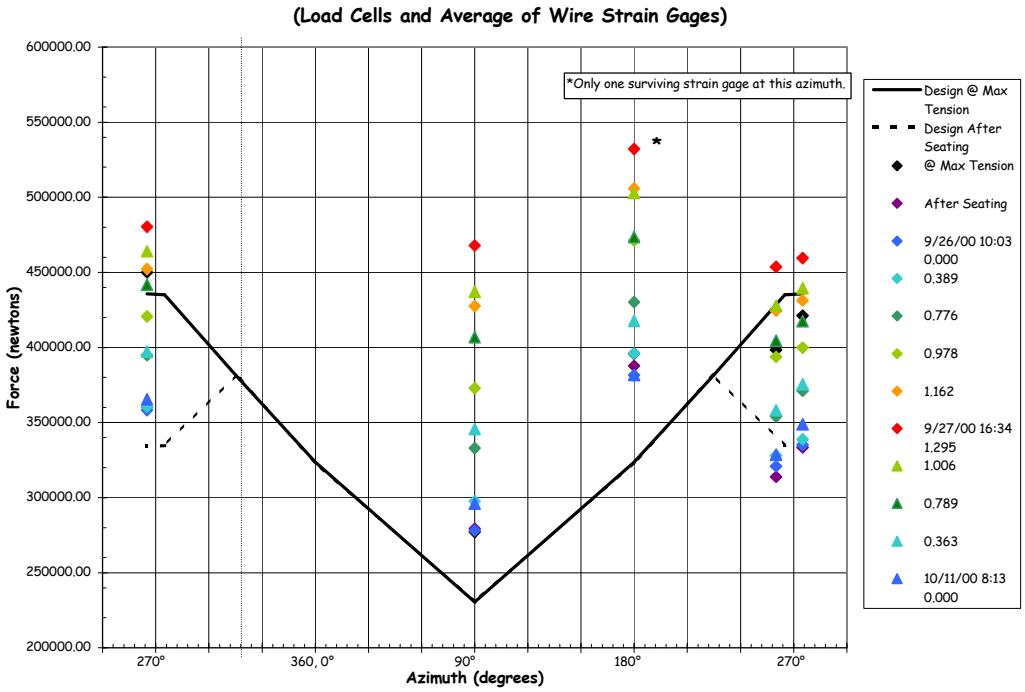

Figure 5.64 H11 Tendon Force Distribution, El. 1854

Figure 5.65 H35 Tendon Force Distribution, Elev. 4572

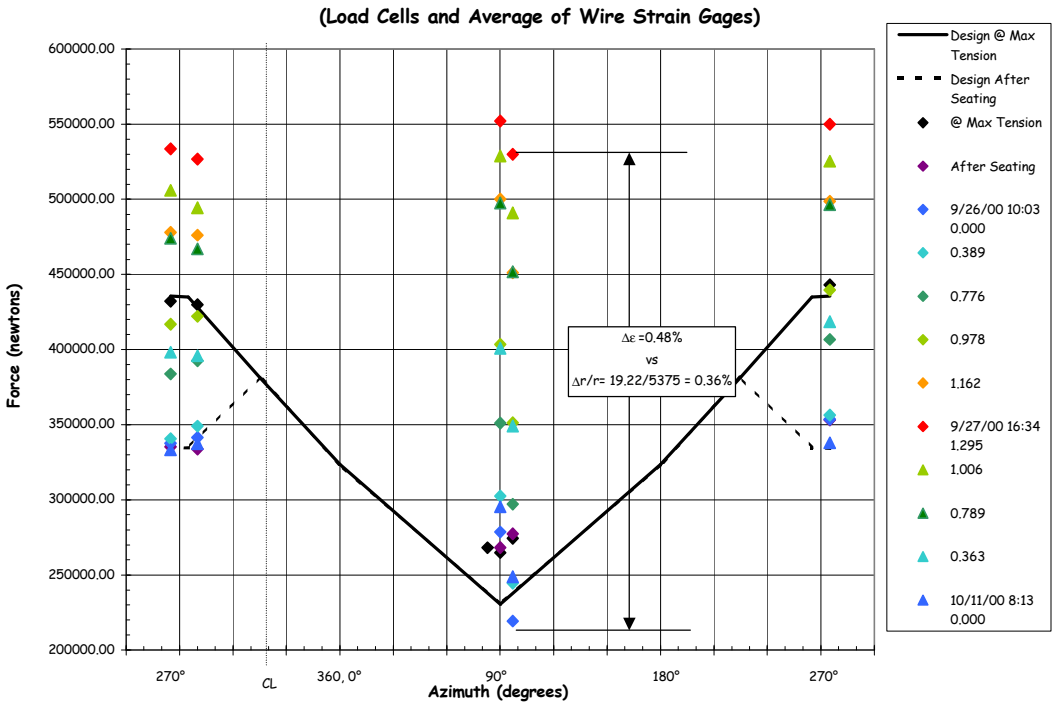

Figure 5.66 H53 Tendon Force Distribution, Elev. 6579

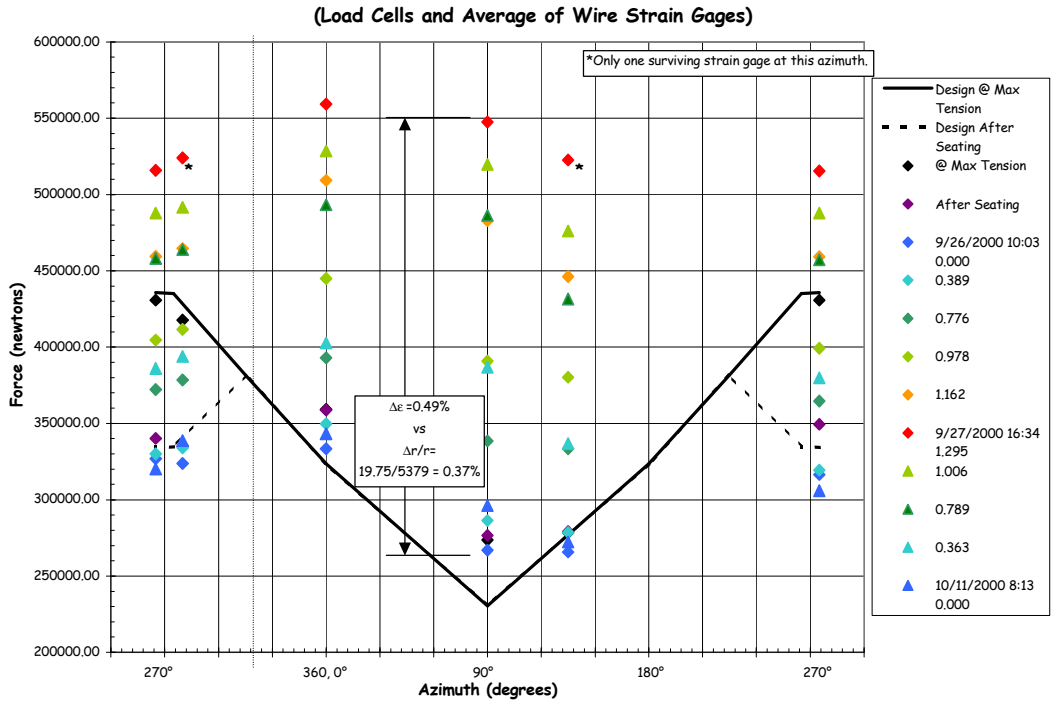

Figure 5.67 H67 Tendon Force Distribution, Elev. 8153

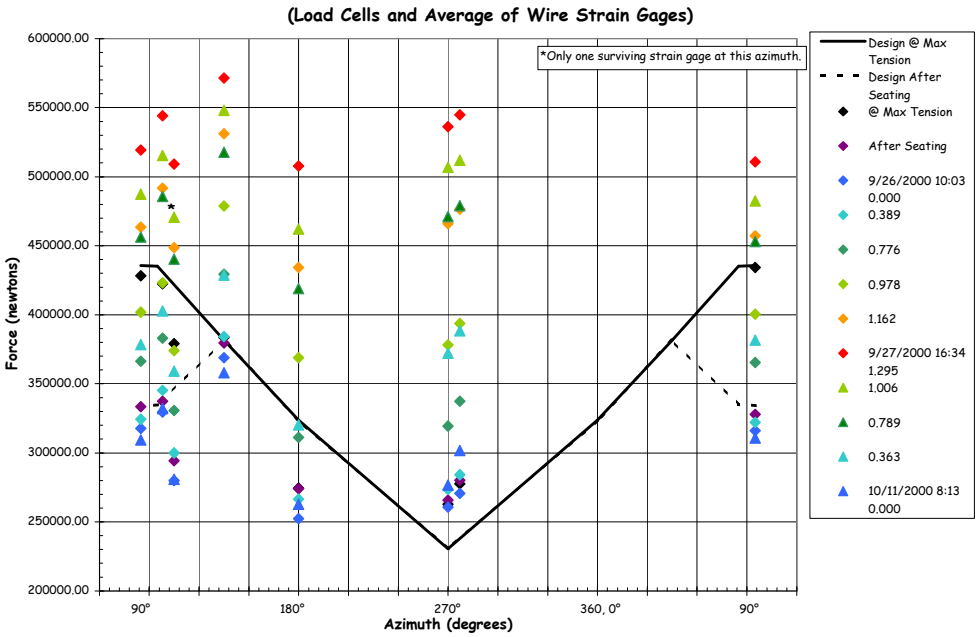

Figure 5.68 H68 Tendon Force Distribution, Elev. 8280

5.3.2.1.5 Acoustic Response

The complete reports from the Acoustic System Operator, Pure Technologies, are provided in Appendix K. As stated in Section 3.2.8, the objectives for the acoustic system were to detect tendon or rebar breaks, concrete cracking or crushing, and liner tearing/leakage. The acoustic system response data, which helped to identify when the PCCV model began leaking, was described in Section 5.2.2 (see Figure 5.17).

There were no tendon wire or rebar breaks during the LST; however, events defined as tendon 'pings' were reported. These tendon pings were interpreted as a readjustment or reseating of the tendon wires/strands as they were tensioned, but the magnitude of these acoustic events are much lower than those associated with a wire break. Figure 5.72 shows the location of the tendon pings are concentrated at the buttresses. Whether this is indicative of source of these events or merely reflects that any tendon events will be transmitted more rapidly along the tendon strands to the acoustic sensors on the buttresses is speculative, but reasonable. A histogram of the tendon ping events as a function of pressure is shown in Figure 5.73. The fact that the majority of tendon pings occurred around $2.0P_d$ is noteworthy, but the reason for physical significance of this is not obvious. It may be that a certain level of tension must be applied to reseat the strands, or it may simply be that this pressure was held for almost eight hours and the number of events that accumulated at this time appears to be significant.

A total of 489 cracking events were detected from March 3 to September 27, 2000. Two-hundred twenty nine of these events were recorded during the LST. These cracking events represent distinct acoustic events, as distinguished from the ubiquitous 'crackling' which occurred nearly continuously during the period the PCCV was monitored by the acoustic system. This crackling is believed to be the acoustic manifestation of microcracking and shearing in response to environmental and pressure loading. The acoustic events identified as cracking represent the formation or extension of discrete macrocracks in response to the applied pressure or other loads. Figure 5.74 maps the location of the cracking events during the LST, grouped by pressure bands. No obvious pattern emerges from this map except that the majority of cracks occurred in the middle section of the cylinder wall, where the strains and displacements were greatest. A histogram of the cracking events as a function of pressure, shown in Figure 5.75, however, reveals the majority of cracking events occurring in the range of 1.5 to $2.0P_d$ where the initial loss of stiffness, presumed to be due to concrete cracking, was already noted.

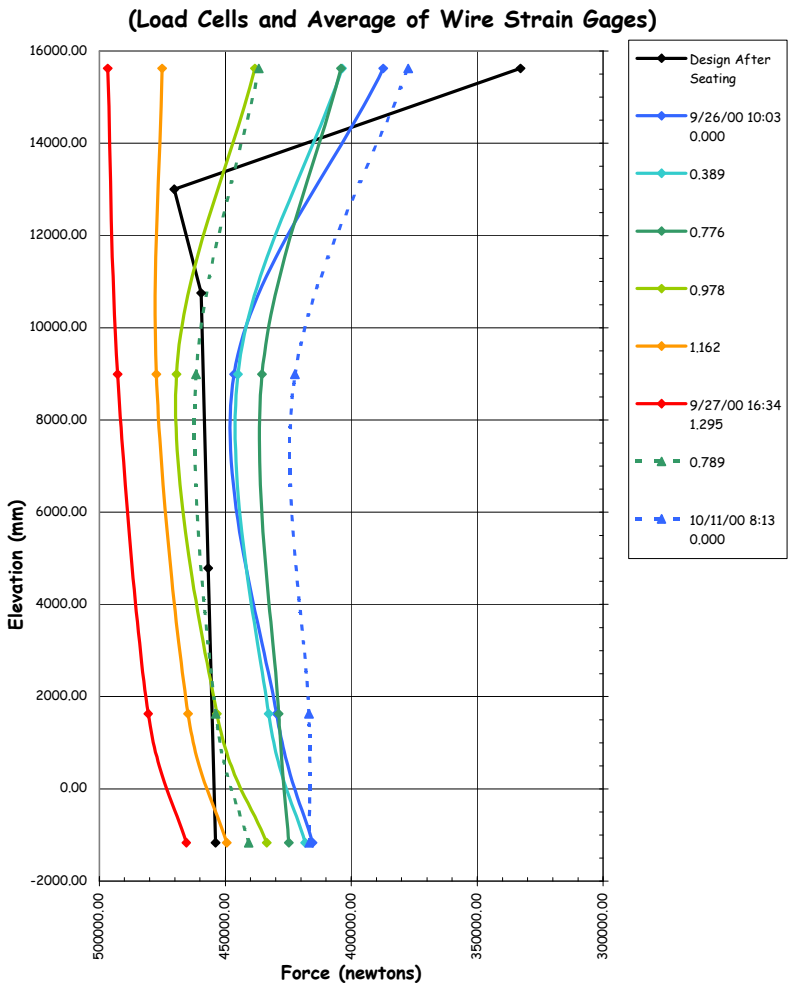

Figure 5.69 V37 Tendon Force Distribution, Azimuth 240 degrees

5.3.2.2 Posttest Inspection

Post-LST inspection of the PCCV model consisted of external crack mapping, visual inspection of the liner and metallurgical examination of the liner tears, and posttest measurements around the E/H.

5.3.2.2.1 Crack Mapping

New cracks and extensions of existing cracks within the crack mapping zones resulting from the LST (see Fig. 5.8) were traced in red and the surface was photographed to document the crack locations (e.g. Fig 5.22). The cracks were then transferred to the crack map drawing, shown in Figure 5.76, which shows all the major cracks identified after various loading stages. In general, concrete cracking was not extensive or very severe, with the exception of some areas around the E/H and some of the smaller penetrations. As noted in Chapter 3, there was no effort to measure crack widths. While it can be observed that some of the larger cracks around the E/H are near the liner tear locations, there was no further effort to correlate the crack locations with other events or data.

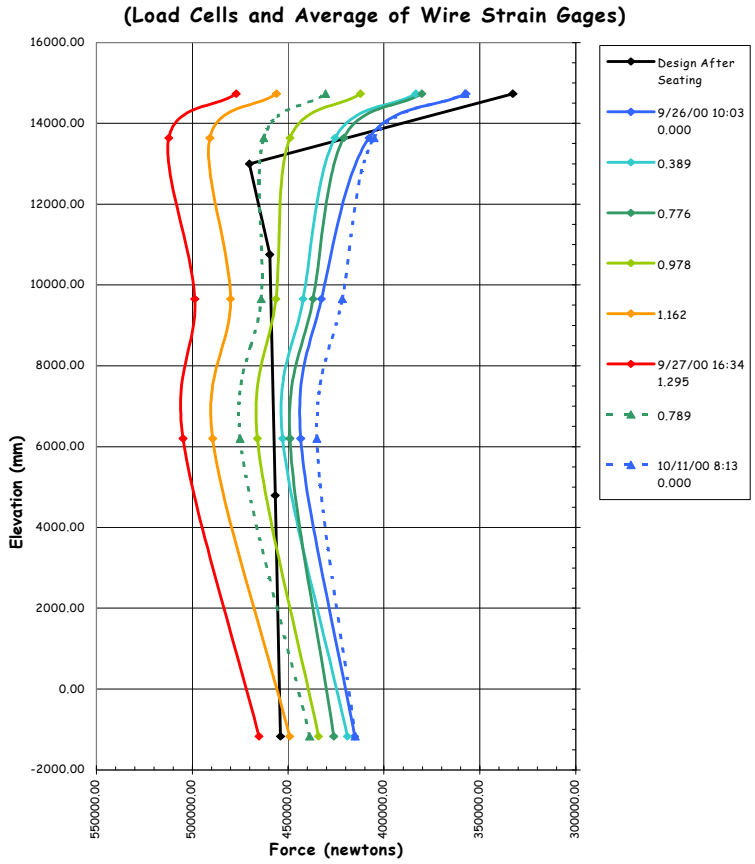

Figure 5.70 V46 Tendon Force Distribution, Azimuth 135 degrees

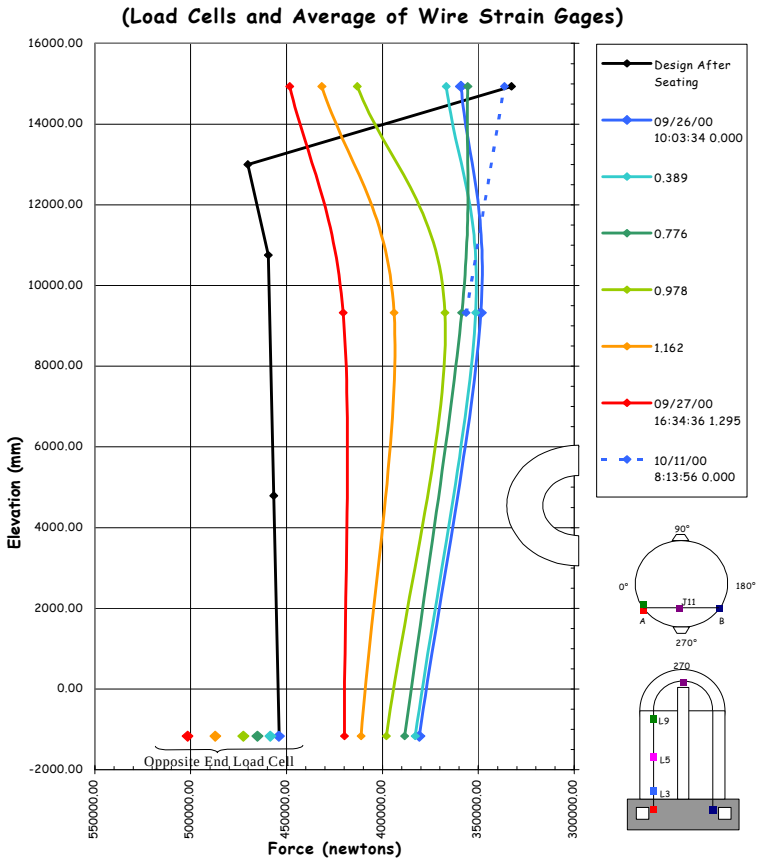

Figure 5.71 V85 Tendon Force Distribution, Azimuth 325 degrees

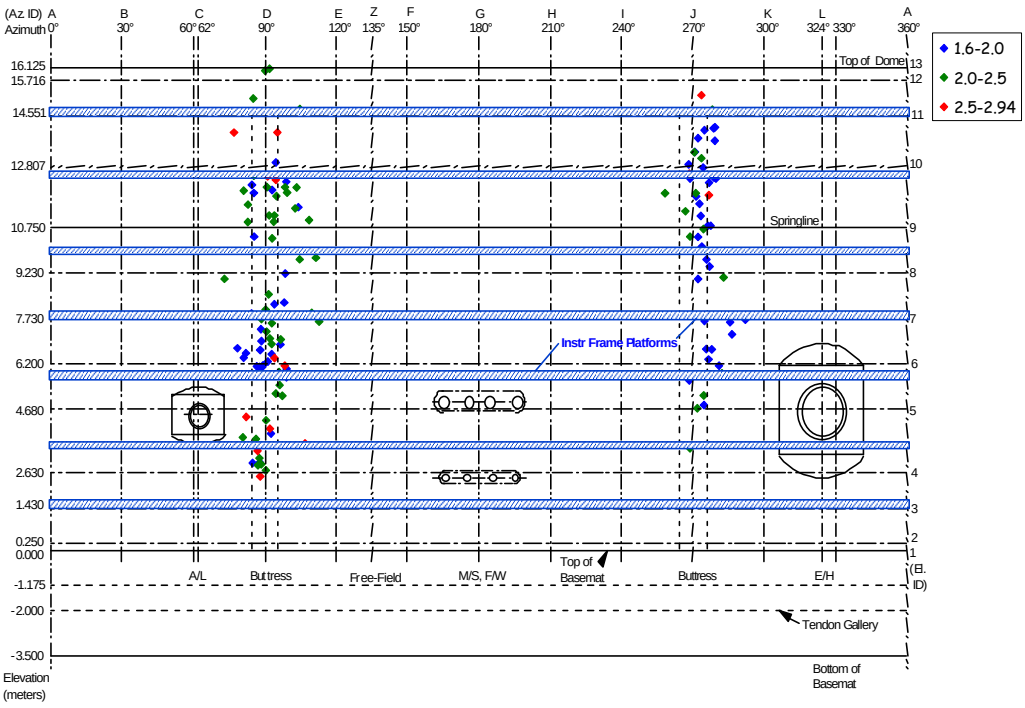

Figure 5.72 LST – Tendon Ping Acoustic Events

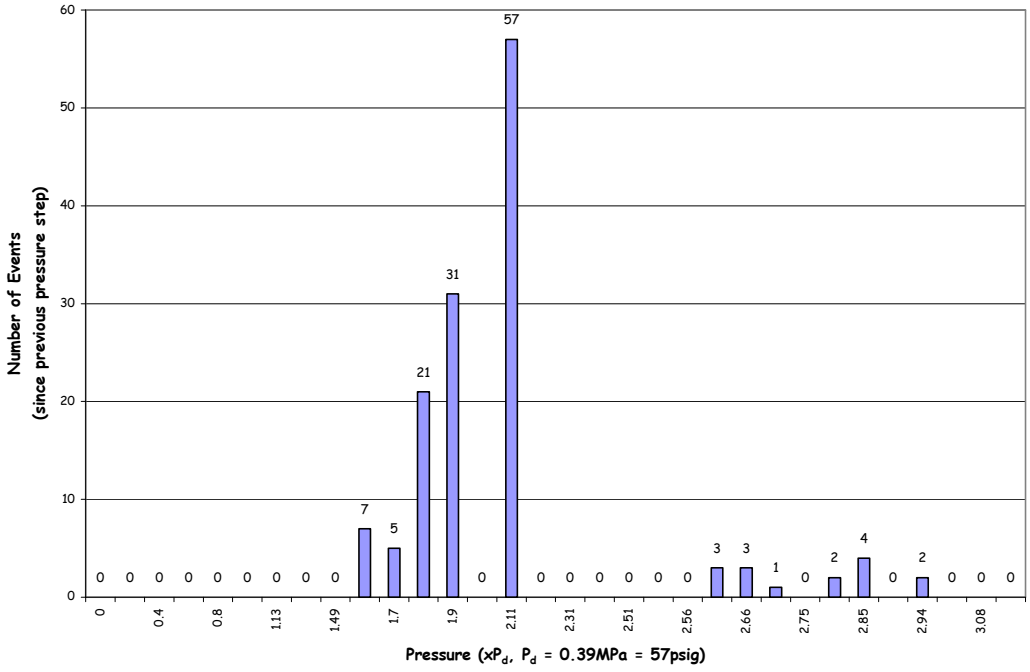

Figure 5.73 LST – Tendon Ping Event vs. Pressure Histogram

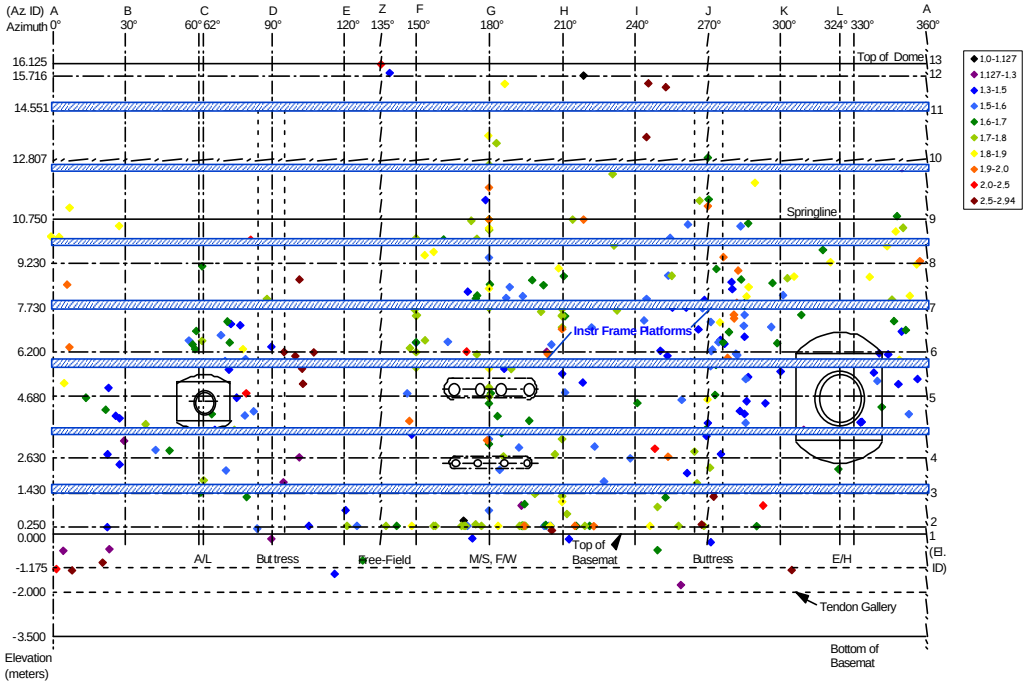

Figure 5.74 LST – Concrete Cracking Acoustic Events

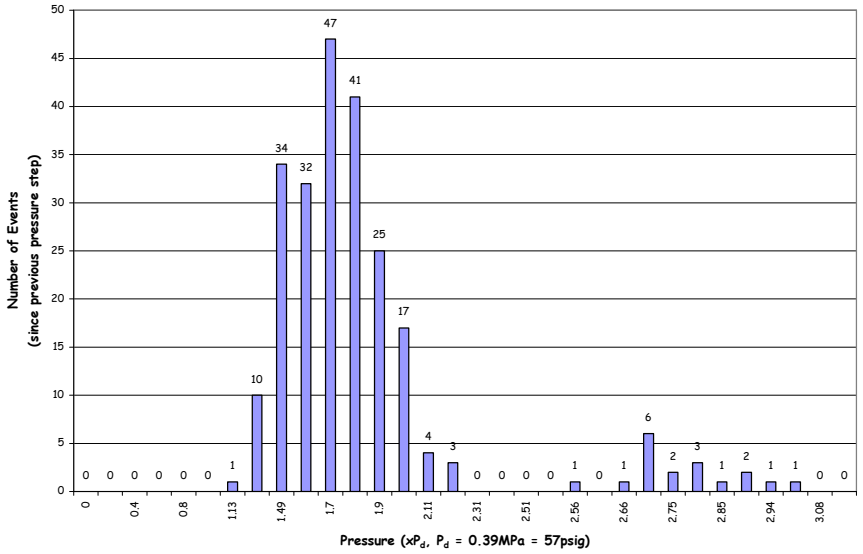

Figure 5.75 LST – Concrete Cracking Events vs. Pressure Histogram

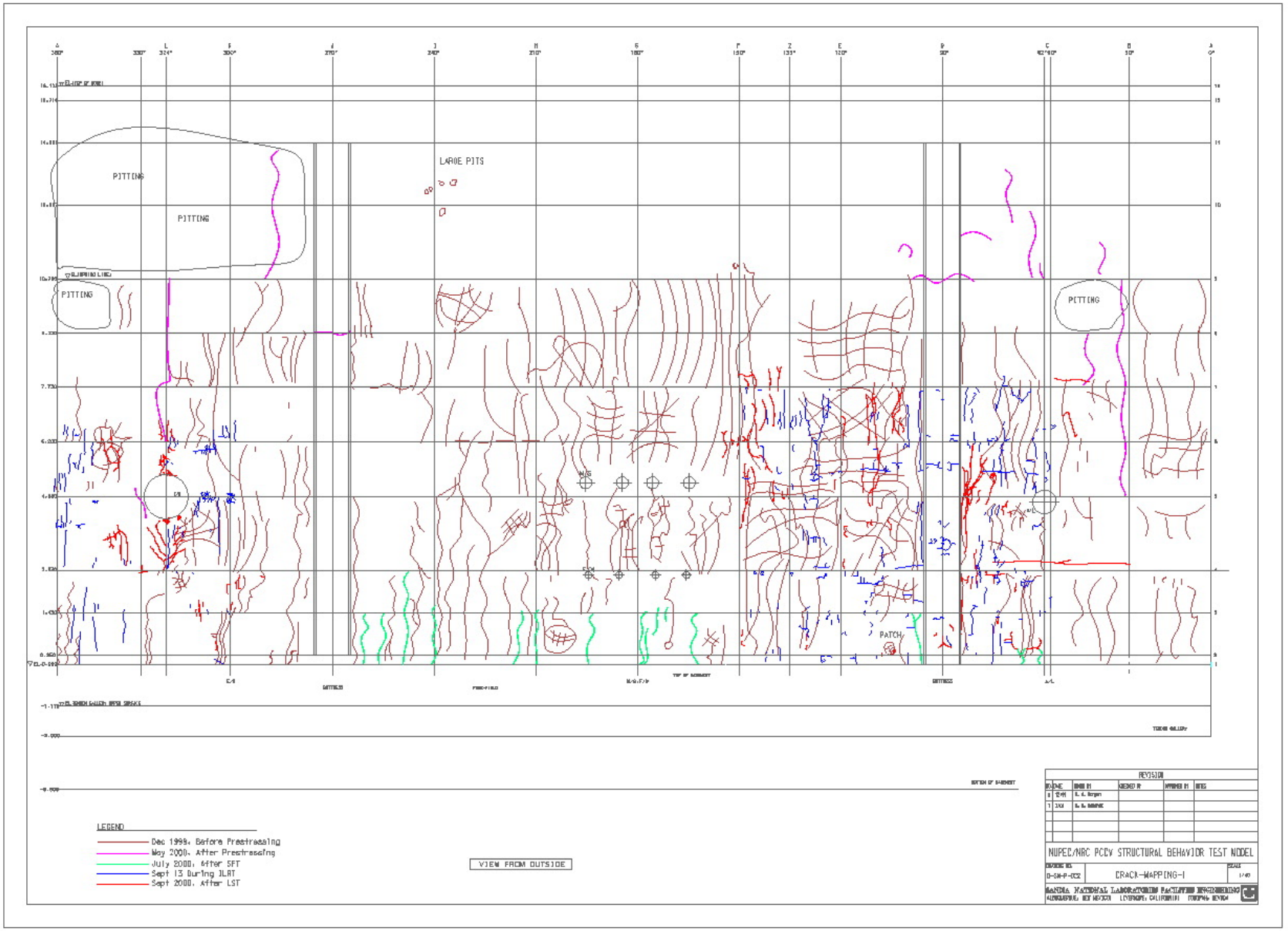

Figure 5.76 Post-LST Concrete Crack Map

5.3.2.2.2 Liner Inspection

As noted in Section 5.2.3, after entering the model following the LST, the liner surface was examined carefully and 26 discrete tears were found at 18 different locations, the grouping by location being somewhat arbitrary. The location of the tears are mapped in Figure 5.77. The location numbers are subsequently used to identify the tears.

One immediate observation was that each liner tear was at or very near a field weld seam in the liner. No tears were found in the undisturbed parent material or at a shop weld.

The acoustic events, later associated with the sound of the nitrogen gas escaping through the liner tears, are superimposed on the tear map in Figure 5.78, along with the approximate pressure levels when these events were first detected. The first tearing event appears to be clearly associated with the tears along the edge of the E/H embossment (#7, #12, #13, and #15), although it is arguable which of these occurred first. The other acoustic tearing events cannot be as clearly identified with any specific tear or tears, and, near the end of the test, it may have been difficult to distinguish the separate 'tearing' events from each other since gas continued to escape through each tear after it occurred.

A typical liner tear (#2) as it appeared during the initial inspection is shown in Figure 5.79. In addition to the liner tears, a pattern of buckling appeared throughout the middle section of the cylinder wall. The buckling pattern, also illustrated in Figure 5.79, is believed to have occurred during depressurization, when the permanently stretched liner could not accommodate the elastic recovery of the cylinder wall.

After the initial inspection of the liner, a more methodical inspection was undertaken. Each tear was photographed and matched with photographs of the 'backside' of the liner before the concrete was placed. (One early program decision was to photograph the entire length of every field weld made during the fabrication of the liner. While this was a very time-consuming and painstaking task, the benefit obtained in understanding the causes of the liner tearing was worth the effort.) A sample of the pre-LST exterior condition compared to the post-LST interior condition for Tears #7, #12, #13 and #15 at the E/H, #2 at a free-field weld seam, and #16 at a 'rathole' detail are shown in Figures 5.80 to 5.85.

The paint was then removed from each tear, allowing the liner tear to be seen without being obscured by the paint. Each tear was then photographed again for documentation. Figure 5.86 shows an close-up of Tear #13 after removing the paint. With the paint removed, it was clear that the weld was repaired or had been reworked by grinding at nearly every tear. Note the grind marks in Figure 5.86, which occurred during erection and welding of the liner. (The paint was removed by using chemical strippers; no paint was removed by mechanical methods.)

While this initial inspection was being completed, a detailed posttest liner inspection plan was being developed. After reviewing the plan with NUPEC and the NRC, the plan, consisting of the following elements, was implemented.

1. In-situ examination:
   a. In addition to the visual/photographic records, ultrasonic thickness measurements were made at each tear location and at several baseline locations where tears did not occur.
2. Destructive examination:
   a. Twenty-five liner specimens were removed from the model (see Figures 5.87 and 5.88).
   b. Eighteen of the liner specimens were subjected to metallographic analysis.
   c. Sample weld specimens were subjected to metallographic analysis.
   d. After the liner specimens were examined by SNL, the unused portions were sent to NUPEC for further examination. The results of NUPEC's examination have been reported separately.

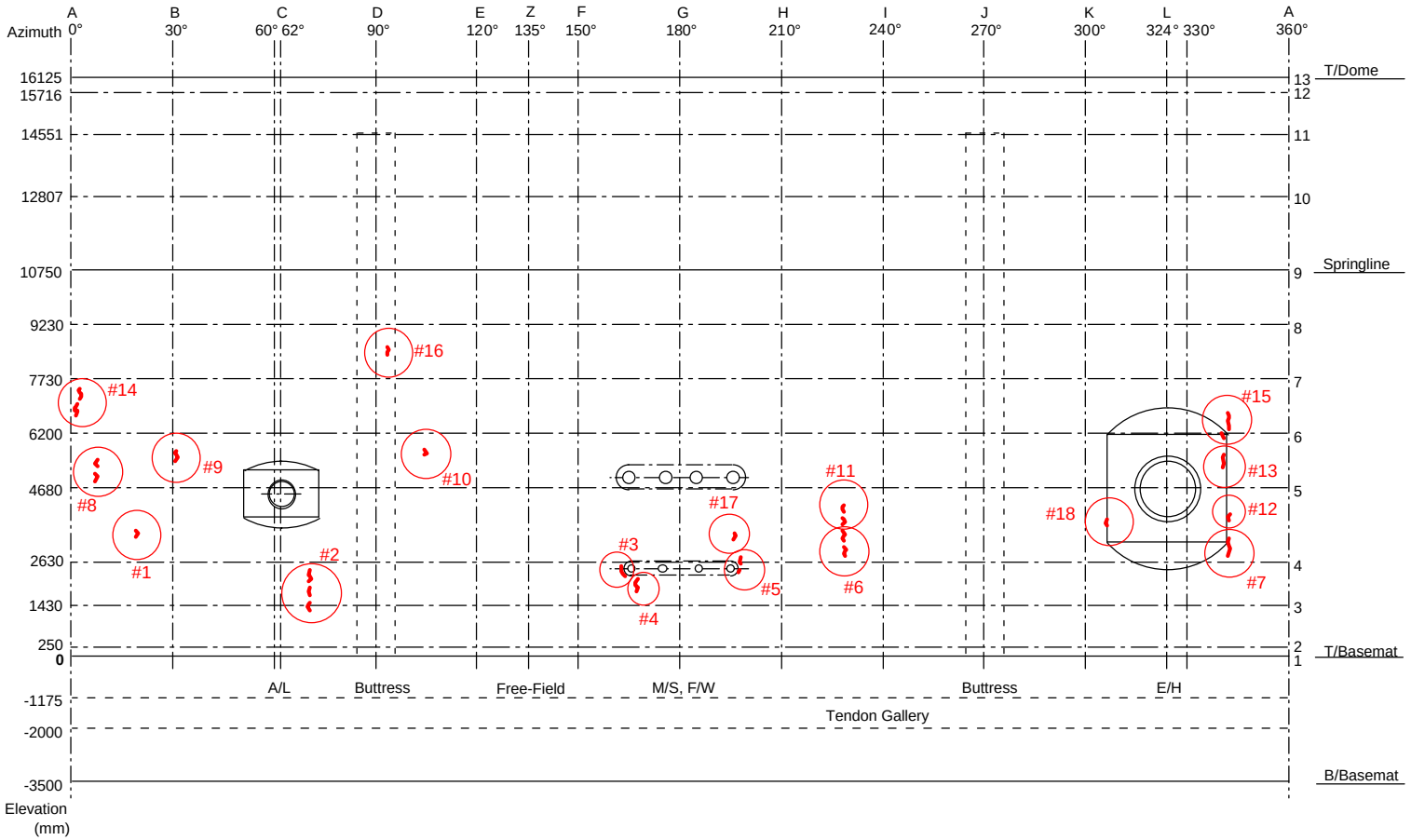

Figure 5.77 Post-LST Liner Tears

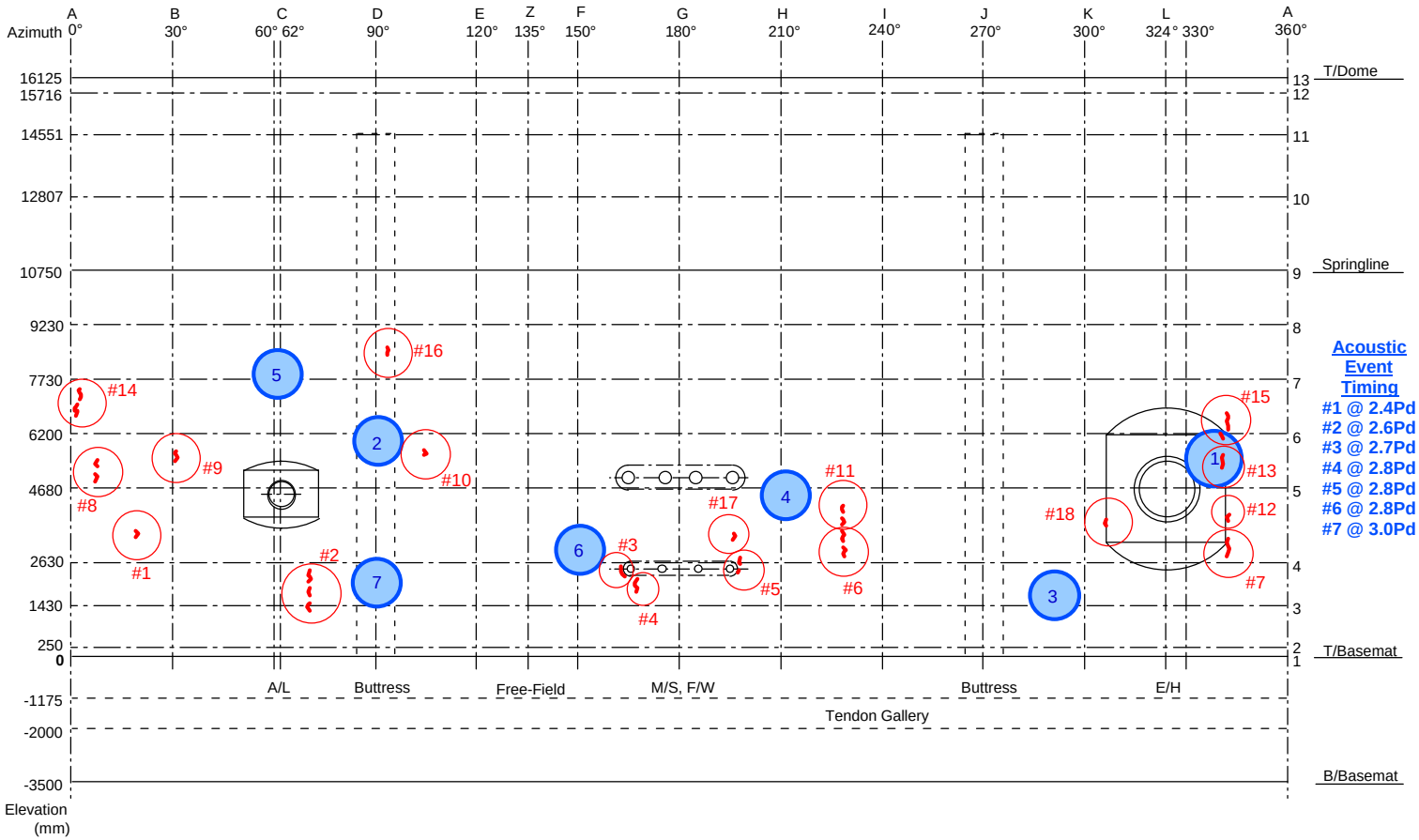

Figure 5.78 Liner Tears and Acoustic Event Locations

Figure 5.79 Post-LST Liner Tear (#2) and Liner Buckling

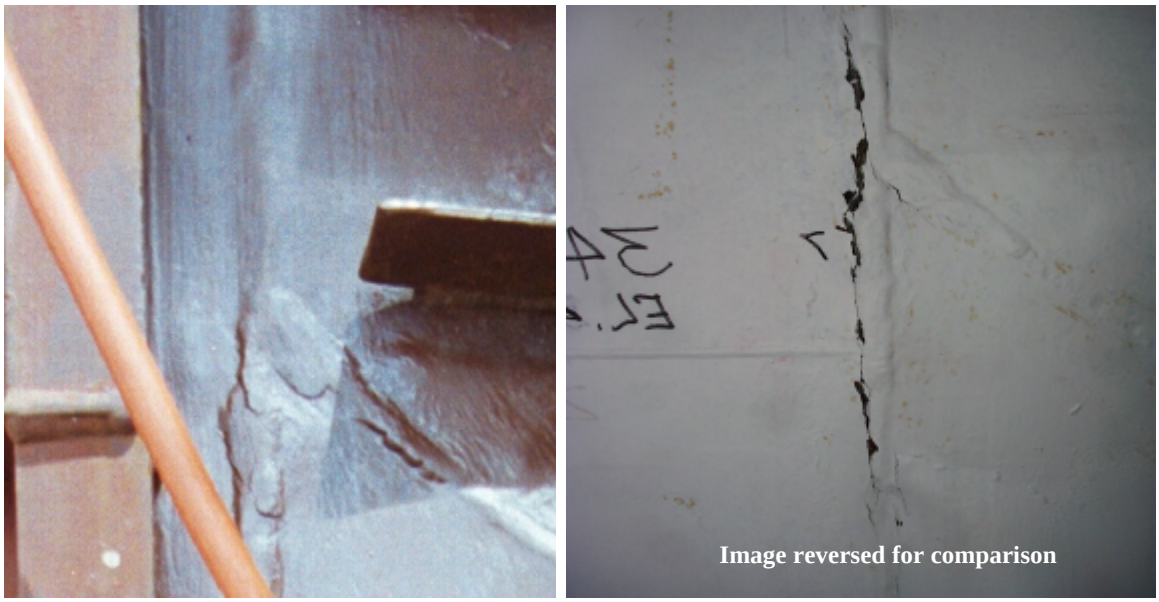

Figure 5.80 Tear #7 at E/H

Figure 5.81 Tear #12 at E/H

Figure 5.82 Tear #13 at E/H

Figure 5.83 Tear #15 at E/H

Figure 5.84 Tear #2, Free-Field

Figure 5.85 Tear #16 at Rathole Detail

The results of the liner inspection are detailed in Appendix L. The conclusions of the inspection and metallographic analysis are repeated below.

1. Nearly all of the tears occurred in areas where the liner thickness was reduced ~25% or more by grinding done in association with repair welding. Extensive localized plastic deformation culminating in ductile tearing occurred in these thinned areas as the structure was being tested. This appears to have been the most prevalent cause of liner failure.
2. In samples where quantification was possible, it appears that the reduced thickness at the point of failure was up to 50% of the local material thickness.
3. At the E/H
   a. #15: 50%-60% reduction by grinding
   b. #13: 25% reduction by grinding
   c. #12: >10% reduction by grinding
   d. #7: 25% reduction by grinding
4. @ the Free-Field
   a. #16-1 (D7): no tear, no repair ~10% reduction in thickness (post-LST)
   b. #16-2: tear, single weld repair, thickness reduction on both sides of weld
5. Geometric features may also have contributed to the formation of some tears. These include structural transitions, such as those at the feedwater penetration and the equipment hatch transition boundaries, discontinuities in horizontal stiffeners, and discontinuities in weld back-up bars. A missing segment in a horizontal back-up bar appears to have been primarily responsible for one tear (#16).
6. Only one tear occurred in association with a material or weld defect. A lack-of fusion weld defect was found at the initiation site of tear #1.
7. The specially produced quarter-scale liner material exhibited mechanical properties that may have made it particularly prone to plastic strain localization and tearing. While nearly conforming to the specifications for full-thickness material, the quarter-thickness plate exhibited a yield strength much higher than the specified minimum (383 MPa compared with 225 MPa) and an unusually high yield-to-ultimate-strength (YS/UTS) ratio (0.77). This high YS/UTS ratio is qualitatively consistent with extensive localized plastic strain culminating in ductile tearing in regions where more than ~25% of the liner thickness had been ground off, as was observed near most of the tears.

Figure 5.86 Close-Up of Tear #13 after Removal of Paint

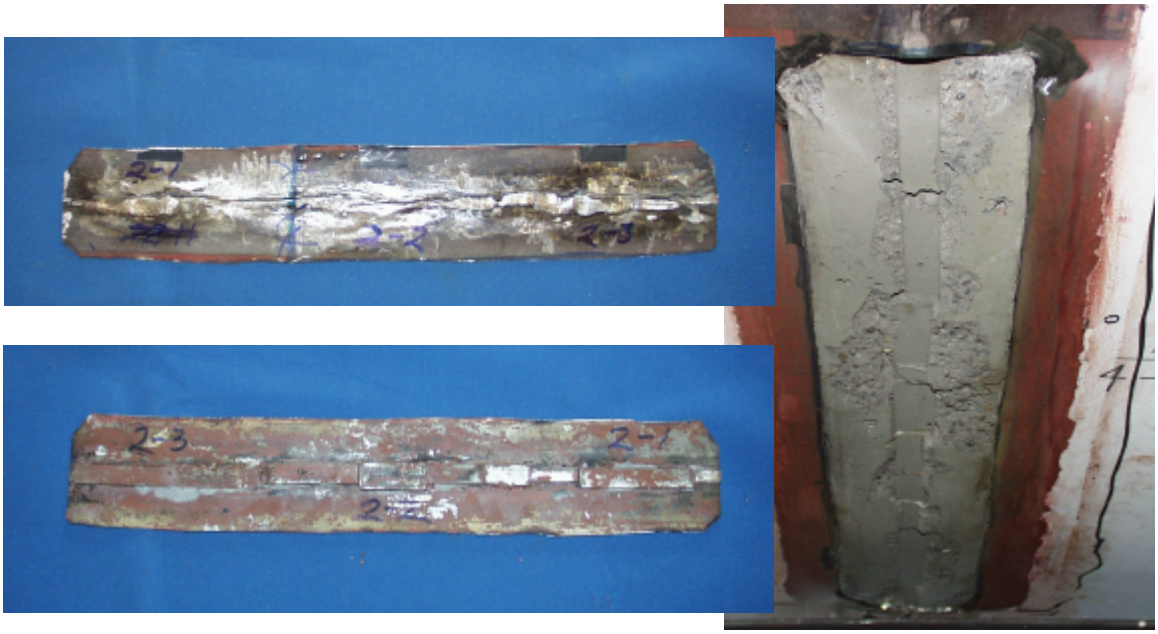

Figure 5.87 Liner Specimen at Tear #2

Figure 5.88 Liner Specimen at Tear #15

8. Tensile and hardness tests on welded test samples indicated that modest amounts of plastic strain localization should be expected in the weld-heat-affected zones, but to a much lesser extent than observed in association with the liner tears. Consistent with this, smaller (but significant) amounts of localized plastic strain were observed adjacent to some welds that had not been repaired or ground. These strains were sufficient to initiate necking in the most severely strained regions. However, with the possible exception of tear #12, there was no indication that tearing was imminent in regions other than those where repair welding and substantial grinding had been done.
9. The mechanical testing results did not suggest that deficiencies in the properties of either the base metal or weld metal, nor excessive softening in the weld-heat-affected zones, could account for the extensive localized plastic deformation culminating in tearing that appeared to occur in the liner.

In summary, it is apparent that the onset of liner tearing at $2.5P_d$ resulted, to a significant degree, from the difficulty of field welding the very thin liner. The conditions that led to the liner tearing would not be present to the same degree in the prototype, and the initiation of tearing might be delayed until a higher pressure was achieved. Nevertheless, in spite of the liner welding difficulties, it is also apparent that the near field strains in the vicinity of a liner discontinuity must be large enough to initiate a tear because all the tears were initiated at vertical weld seams within the middle portion of the cylinder wall.

5.3.2.2.3 Posttest Measurements

As described in Section 3.2.5.4, a grid was constructed around the E/H to measure the residual strain field after the test. The pretest analysis predicted large strains near the perimeter of the thickened insert plate surrounding the E/H barrel and near the anchors and stiffeners that terminated near the insert. The grid, shown in Figure 5.89, was drawn, and the position of the grid points was obtained using a 3D digital position mapping tool. After the LST, the grid points were mapped again and the pre- and posttest positions were plotted in Figure 5.90.

Unfortunately, as noted previously, the strains in this region were very small and the resulting residual displacements are barely distinguishable from the pretest positions, given the precision of the digital probe. As a result, no useful information was obtained by this effort.

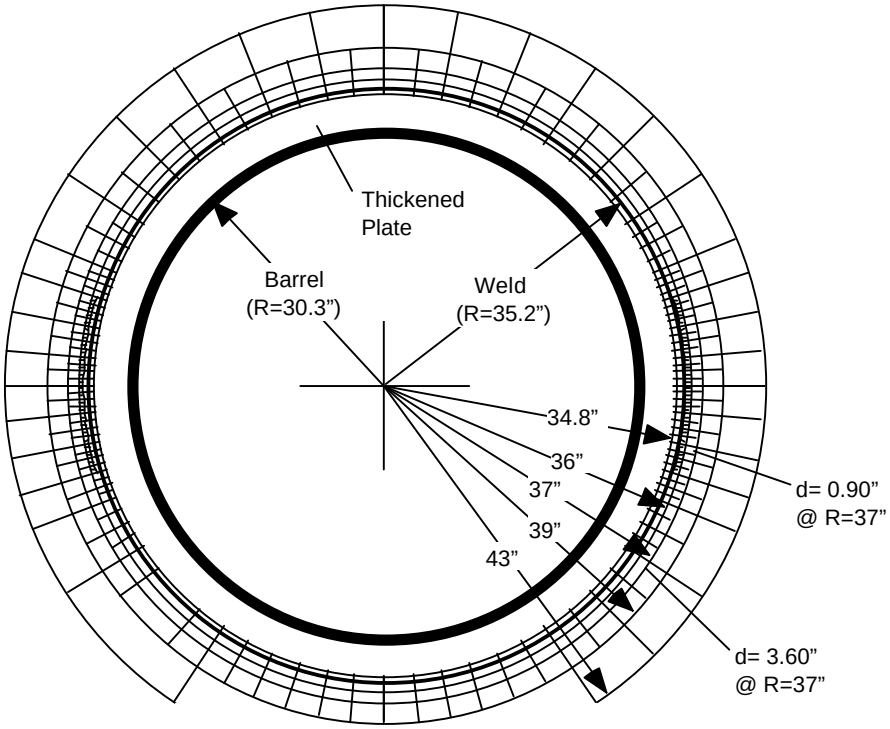

E/H Inside View

Figure 5.89 E/H Displacement Grid

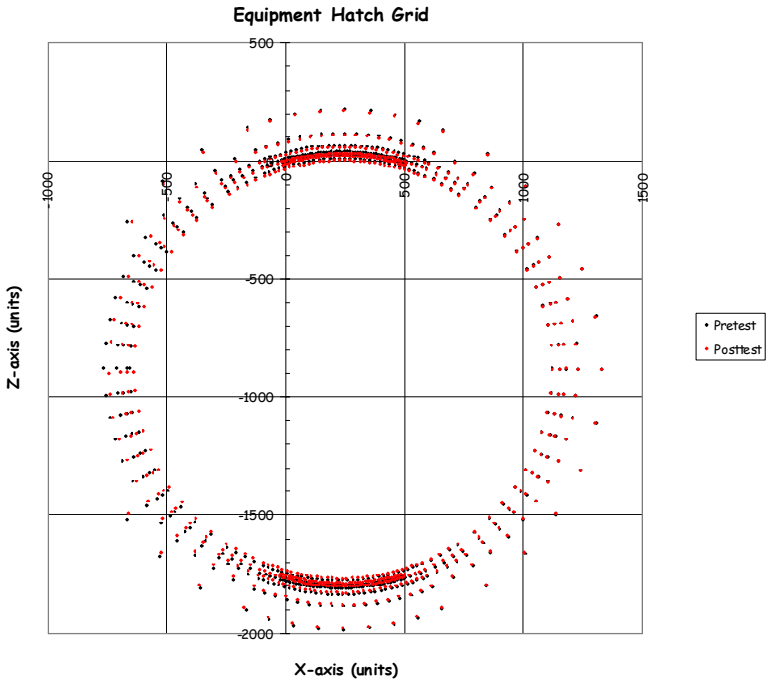

Figure 5.90 E/H Post-LST Displacement

5.3.3 Structural Failure Mode Test Results

5.3.3.1 Test Data

The Structural Failure Mode Test data (DYN only) is provided on the enclosed data CD in Excel© spreadsheets, as noted in Section 5.3.1. The response of every functioning transducer in the revised instrumentation suite is provided. The following sections present a synthesis of the data focusing on the critical response measurements.

5.3.3.1.1 Displacements

As for the LST, the displacement data provides the most comprehensive view of the overall or global response of the model. Since the displacement transducers had to be waterproof, a reduced suite of gages was used during the SFMT. Based on the results of the LST, two vertical arrays at Azimuth 135 degrees and 324 degrees, and one horizontal array at Elev. 4680, were employed for the SFMT, as shown in Figure 5.26. Figures 5.91 through 5.93 show the radial displacement response as a function of pressure along these cardinal lines. Since the displacement transducers had to be removed after the LST to install the elastomeric liner and new transducers were installed for the SFMT, the displacements were 'zeroed' prior to the start of the SFMT on November 6, before filling the vessel with water. The displacements therefore reflect only the response to pressure (including the hydrostatic pressure) and not the effects of prestressing, nor any other previous loading. Note that the pressures shown are the effective pressure, i.e. the volume weighted average pressure in the model.

During the SFMT, the displacement response of the model is essentially linear to just beyond 3.0 Pd, when global yielding begins to occur prior to rupture. The initial stiffness of the model, however, is less than the initial stiffness during the LST. Figure 5.94 compares the response at the mid-height of the cylinder (Z6) during the LST and the SFMT. (The SFMT response was offset in this figure by adding the residual displacement at the end of the LST to facilitate comparison.) This figure shows that the hoop stiffness during the SFMT is essentially identical to the post-cracking stiffness during and after the LST. It also shows that the SFMT displacement is nearly identical to the LST displacement at the maximum LST pressure, suggesting that, if the LST had continued, the response would have been virtually

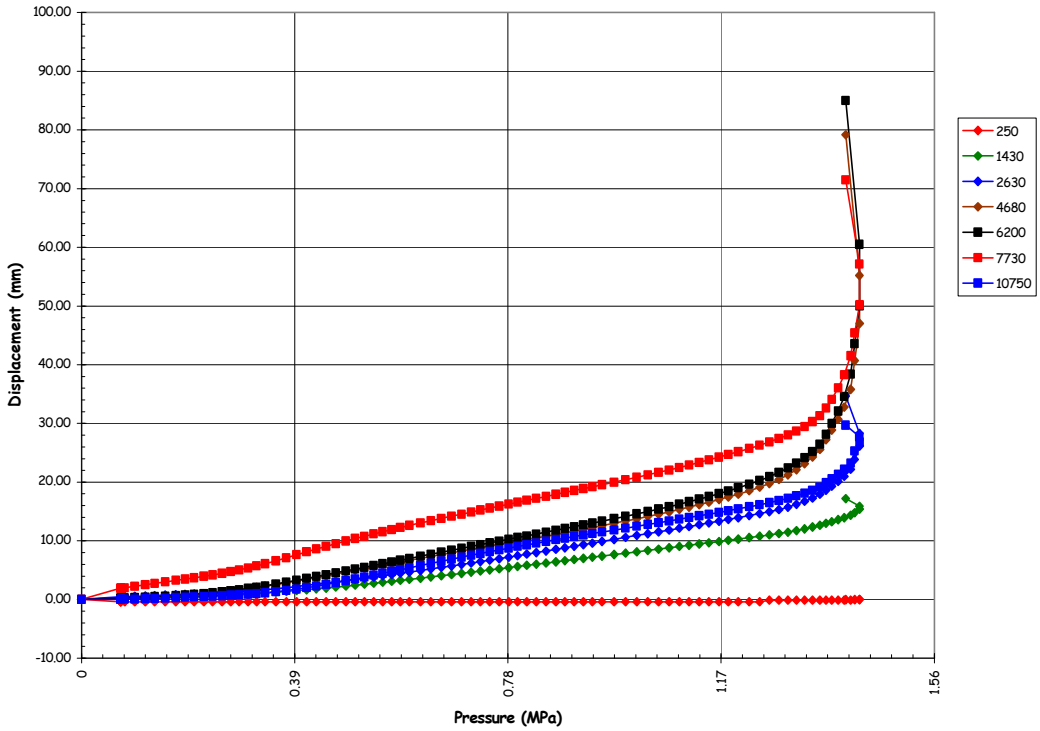

Figure 5.91 SFMT – Radial Displacement at Azimuth 135 degrees (Z)

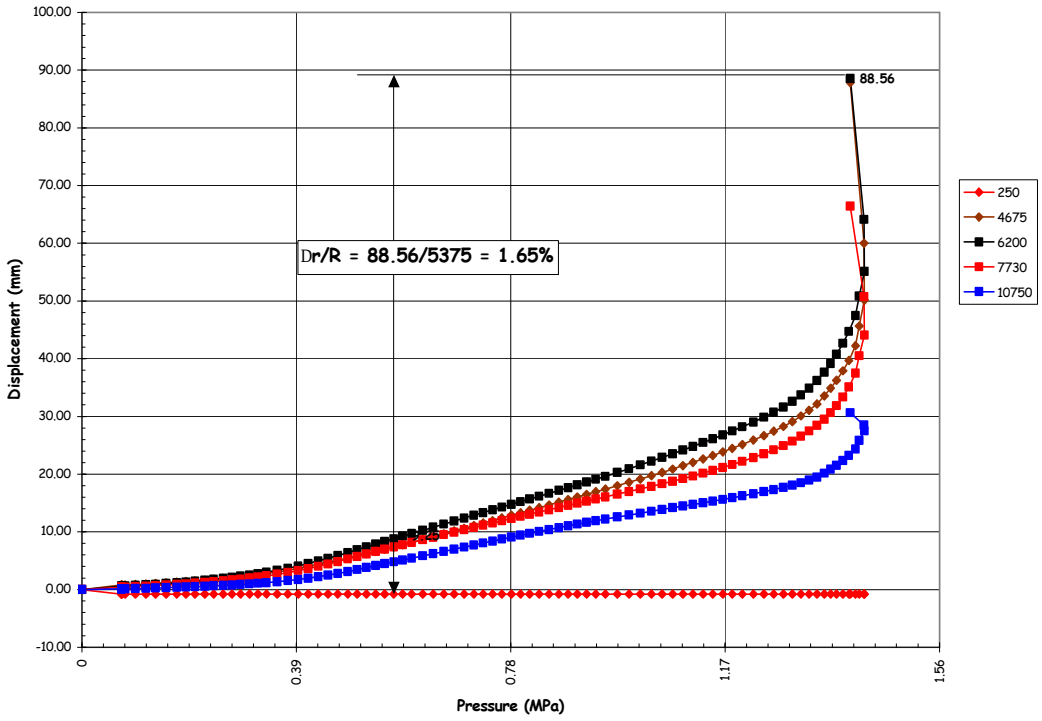

Figure 5.92 SFMT – Radial Displacement at Azimuth 324 degrees (L)

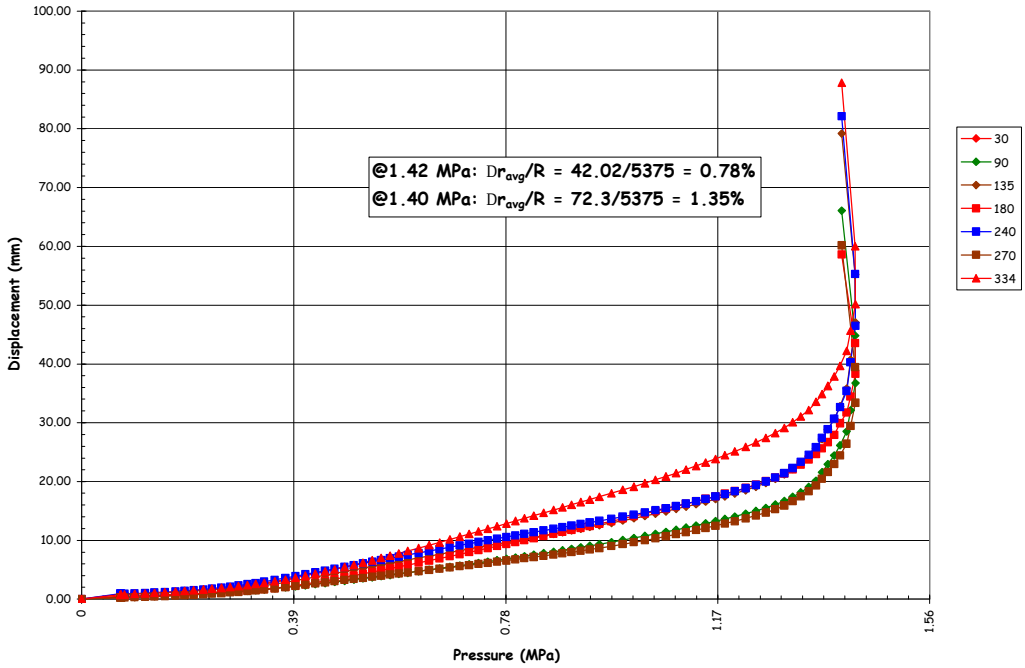

Figure 5.93 SFMT – Radial Displacement at Elev. 4680 (5)

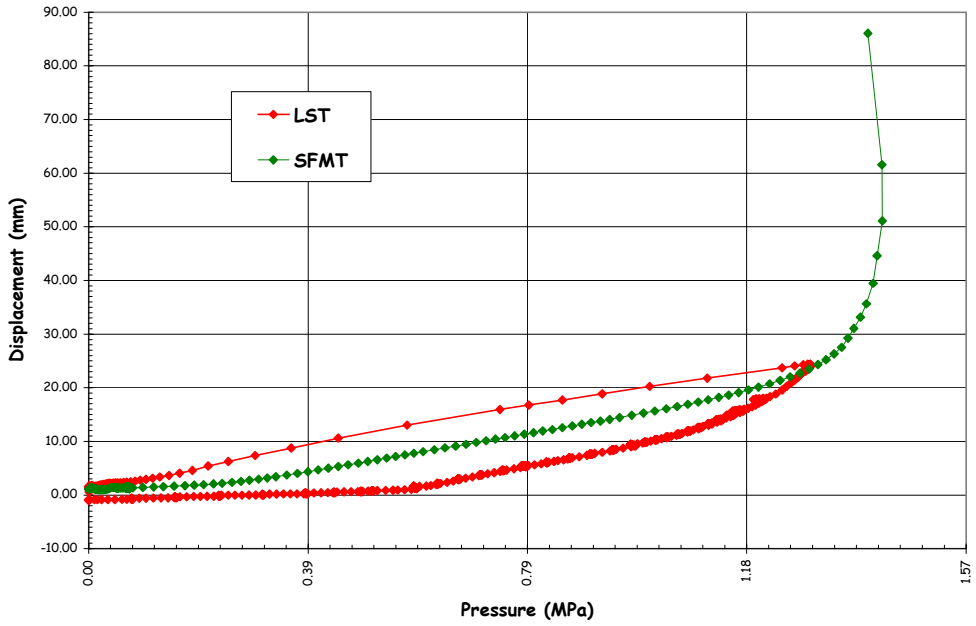

Figure 5.94 SFMT – Radial Displacement at Azimuth 135 degrees, Elev. 6200

identical to that measured during the SFMT. Similarly, the vertical displacements at the apex (offset again) are compared in Figure 5.95.

Since the SFMT was conducted as a continuous pressure test with no holds for gage stability of leak checks, there were no discontinuities in the response histories.

The peak displacements shown in the plots were the final readings obtained before the model ruptured and the gages were destroyed. The pressure values at and beyond the peak were recorded at the beginning of the data scan. Since each scan took approximately 30 seconds, the pressure may have increased (or decreased) during the scan. Note that a few data scans were completed after the peak pressure was reached. The post-peak values may indicate some 'softening' of the model. However, it is more likely that the plots reflect the drop in pressure due to the rapid expansion and increasing leakage just prior to rupture.

Figure 5.92 displays the displacements at Azimuth 324 degrees, which coincides with the centerline of the E/H. The largest radial displacement recorded during the SFMT, 88.56 mm, again occurred at this azimuth at elev. 6200, above the E/H. Computing the equivalent hoop strain due to pressure at this location from kinematics,

$$@P_{final} = 3.58P_d: \quad \frac{\Delta r}{R} = \frac{88.56}{5376} = 1.65\% \ .$$

At the peak pressure, $3.65P_d$, the displacement was 55.12 mm, yielding an equivalent hoop strain of 1.02%

Figure 5.93 compares the displacement response as a function of azimuth at elev. 4680, nominally the mid-height of the cylinder and the centerline of the E/H, A/L, and M/S penetrations. The response is not as uniform as was observed during the LST. Nonetheless, averaging the radial deformation due to pressure yields a nominal average hoop strain of 0.78% at the peak pressure $3.65P_d$. Similarly, the average hoop strain at $3.58P_d$, just prior to rupture, was 1.35%.

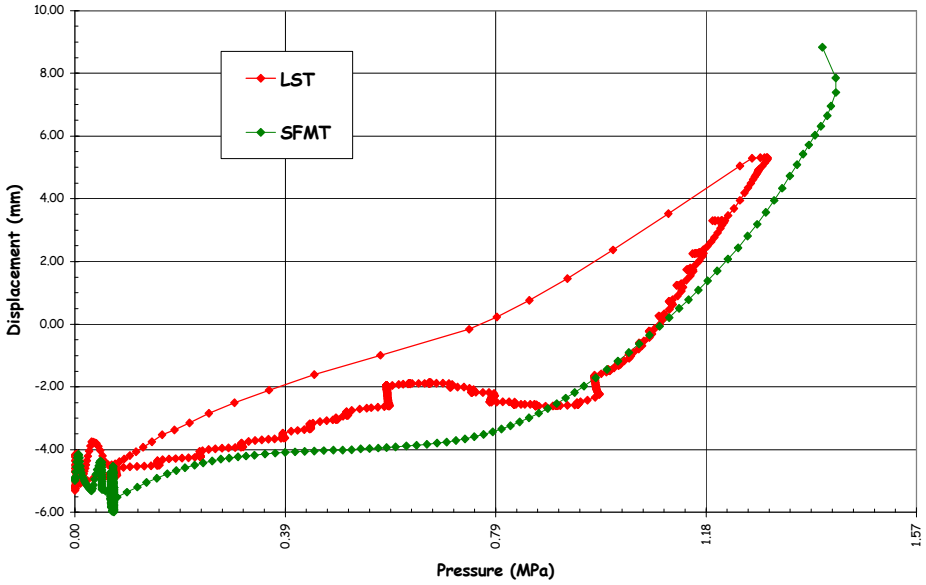

Figure 5.95 SFMT – Vertical Displacement at Apex

The vertical displacements are shown in Figure 5.96. The maximum vertical displacement at the springline was 10.84 mm at Azimuth 135 degrees, essentially the same as during the LST, and 5.94 mm at Azimuth 324 degrees, less than during the LST. The reason for the small displacement at 324 degrees is not immediately obvious; however, it might be the stiffening effect of the E/H embossment, although this was not observed during the LST. Nevertheless, it is clear that the vessel did not yield in the vertical direction and the vertical strains were still on the order of 0.1%.

Deformed profiles of the PCCV model, constructed from the displacement data in a similar manner as those constructed for the LST, are shown in Figures 5.97 through 5.100. For the SFMT, the initial position was again assumed to be defined by the as-built model survey data (Appendix C). However, since the gages were zeroed prior to the start of the SFMT, any deformations of the liner surface or the wall are not reflected in the data.

The as-built position of the PCCV model is plotted in the first portion of the figures, along with the deformed shapes due to the hydrostatic pressure (H_2O) and at approximately $1.0P_d$, $2.0\ P_d$, $2.5\ P_d$, $3.0\ P_d$, 3.5Pd, and $P_{max} = 3.63P_d$. The second portion of each figure provides a more refined breakdown between $3.0P_d$ and $3.63P_d$ and the profile at $P_{final} = 3.57P_d$, immediately prior to rupture of the vessel. These figures dramatically illustrate the large deformations that occur as the vessel yields, even though the pressure is dropping. The displacement nearly doubles as the pressure drops from $3.63P_d$ to $3.57P_d$.

A most provocative observation after considering the displacement data and the global response of the model is that the relatively small pressure increase between the LST and the SFMT, from $3.3P_d$ to $3.6P_d$ (approximately 10%), made the vessel go from a relatively benign and only slightly damaged step to total collapse. It is reasonable to speculate what the response of the model might have been if the liner had not torn and leaked at $2.5P_d$, arguably prematurely, and it had been possible to pressurize it to 3.6Pd pneumatically.

5.3.3.1.2 Liner Strains

Since the liner was damaged during the LST and large portions were removed for metallographic analysis, the response of the liner was not a critical objective during the SFMT. Nevertheless, 18 exterior gages (the interior ones were

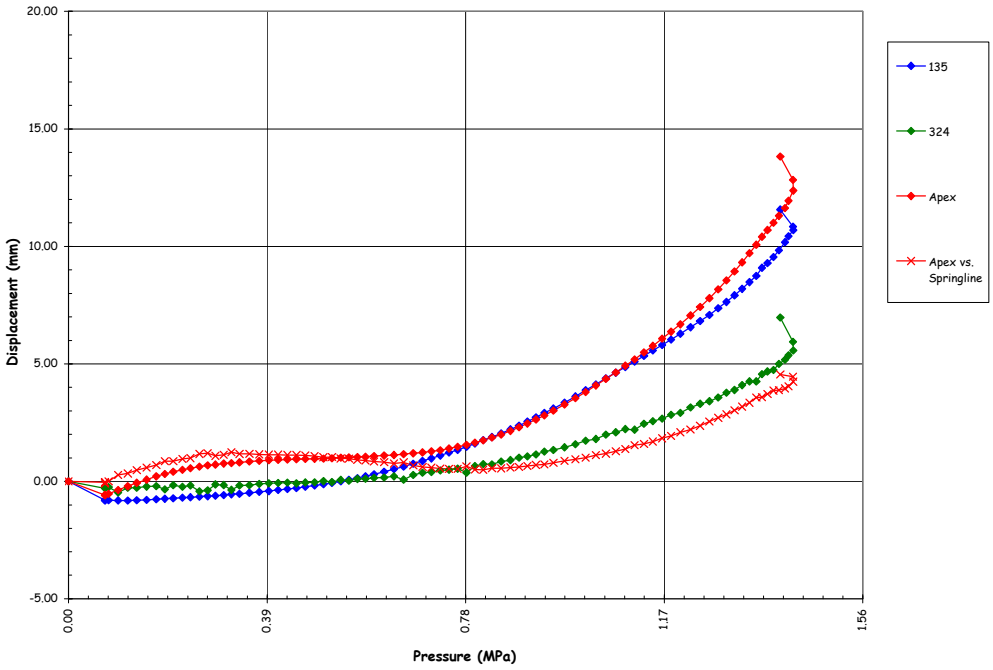

Figure 5.96 SFMT Vertical Displacements at Springline (El. 10750) and Apex

removed prior to installing the elastomeric liner) were monitored during the SFMT to provide some information on the liner response at higher pressures and for comparison with other instruments. Of the 18 strain gages selected, three failed

before filling the model with water. The remaining gages at the wall-base junction and the two external gages at D7 also appeared to have been damaged prior to the test, possibly by water leaking from the model. As a result, meaningful data was only obtained for three liner strain gages.

The strain histories for the surviving gages are plotted in Figure 5.101. These gages measured the hoop liner strain inside a rathole (see drawing D-SN-P-209, Appendix E) at Azimuth 0 degrees, elev. 7730 (A7) and Azimuth 135 degrees, elev. 4680 and 6200 (Z5 and Z6) at the mid-height of the cylinder. The maximum liner strains at Z5 (1.9%) and Z6 (1.5%) are consistent with the strains calculated from the displacements. At A7, nearest the location where the model ruptured, the hoop strains were consistently lower than those at Z5 and Z6, even going into compression, until the peak pressure was reached, when the strain increased rapidly to a maximum of 1.5% tension. While these were not free-field gages, they nevertheless gave some indication of the hoop strains in the liner.

5.3.3.1.3 Rebar and Concrete Strains

Eighty-two rebar and gage bar gages were selected for monitoring during the SFMT. Of these, four of the main rebar strain gages and all the gage bar strain gages appear to have failed before $0.5P_d$. The strain histories for all 31 surviving rebar gages are shown in Figures 5.102 to 5.104. The maximum free-field hoop rebar strain was 1.4% (RS-C-Z6-02). The maximum free-field meridional rebar strain was 0.3% (RS-M-D6-02). These values are consistent with the global strains based on displacement data. The rebar strains at the wall-base junction show the effect of bending but combined with the other meridional strains, confirm that the model was still essentially elastic in the vertical direction.

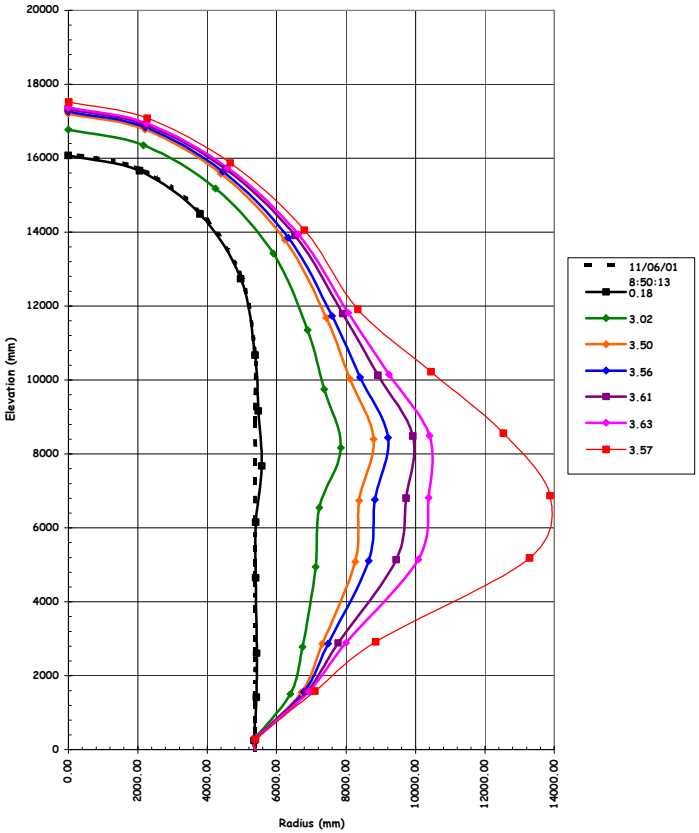

(a) $0P_d$ to$3.63P_d$

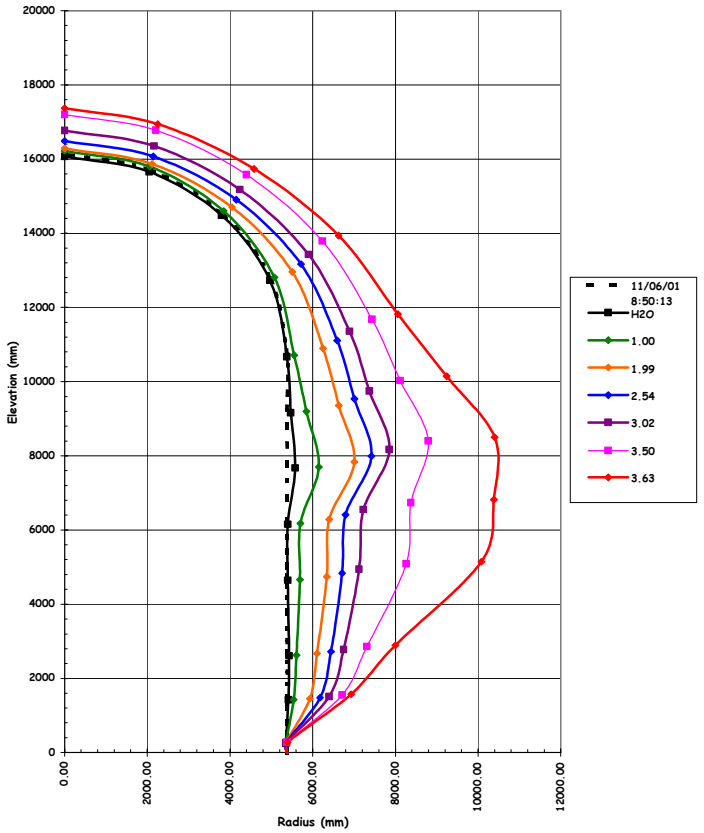

(b) $3.0P_d$ to$3.63P_d$

Figure 5.97 SFMT - Deformation at Azimuth135 Degrees (Z) × 100

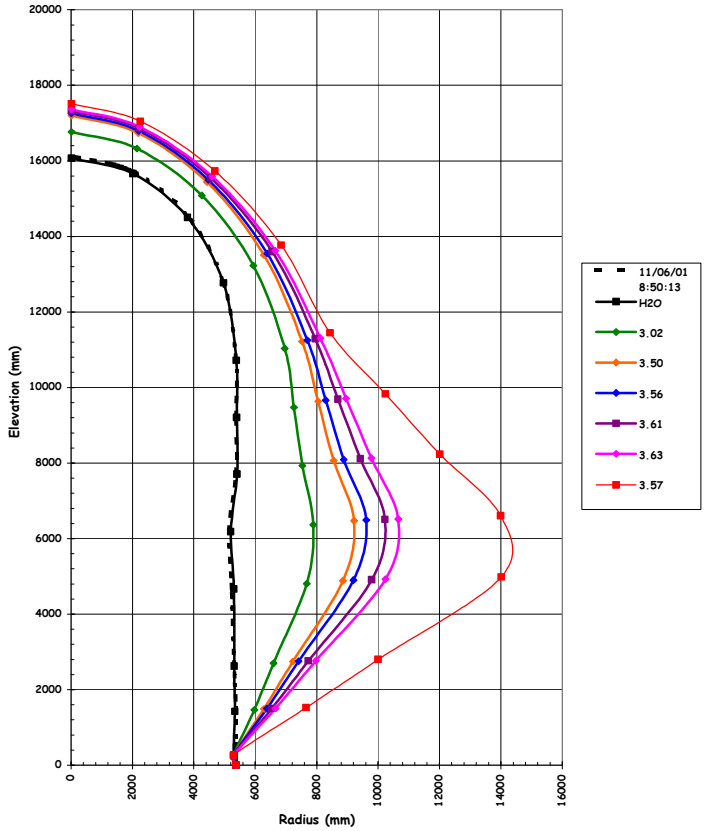

(a) $0P_d$ to$3.63P_d$

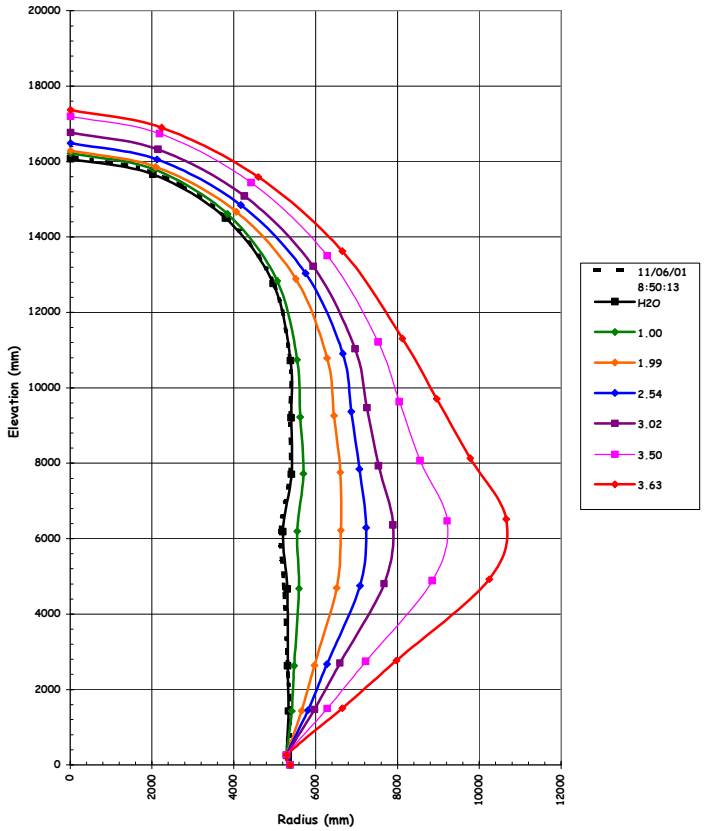

(b) $3.0P_d$ to$3.63P_d$

Figure 5.98 SFMT - Deformation at Azimuth 324 Degrees (L) × 100

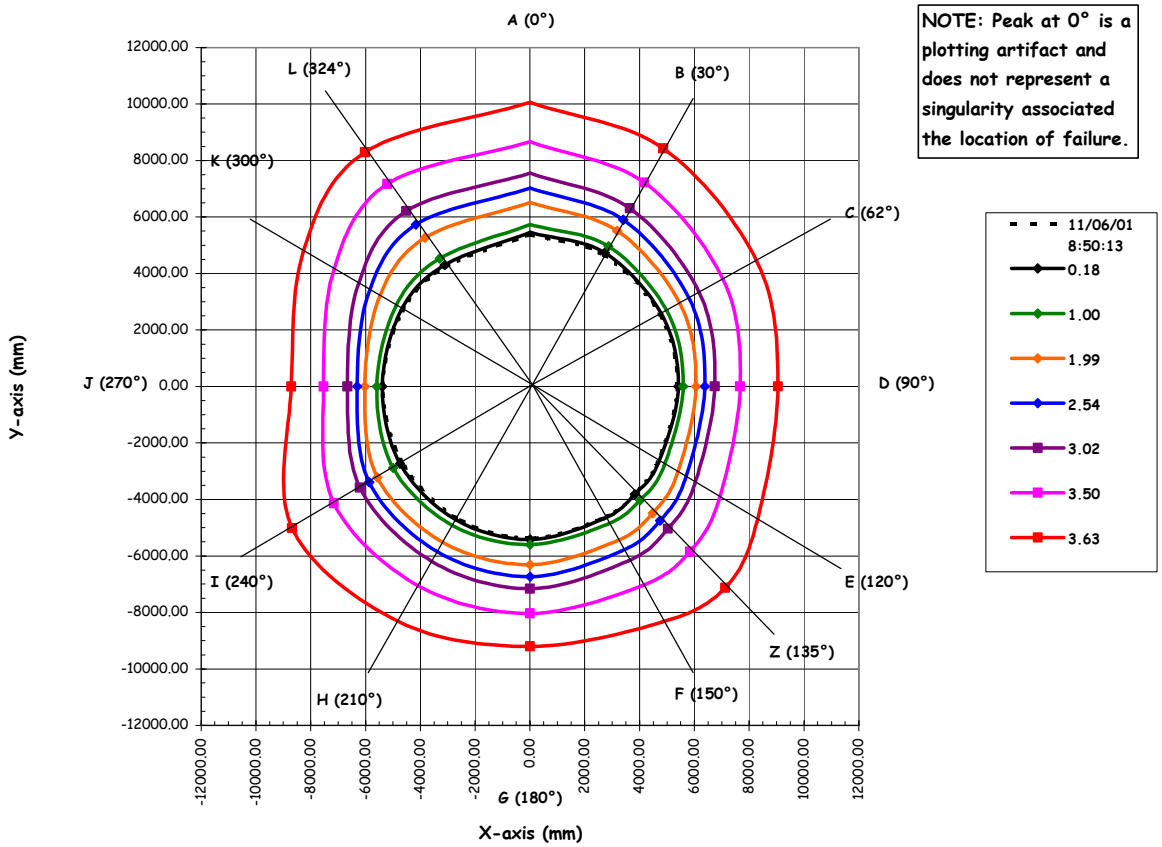

Figure 5.99 SFMT - Deformation at Elev. 4680 (5) × 100 - 0P_d to 3.63P_d

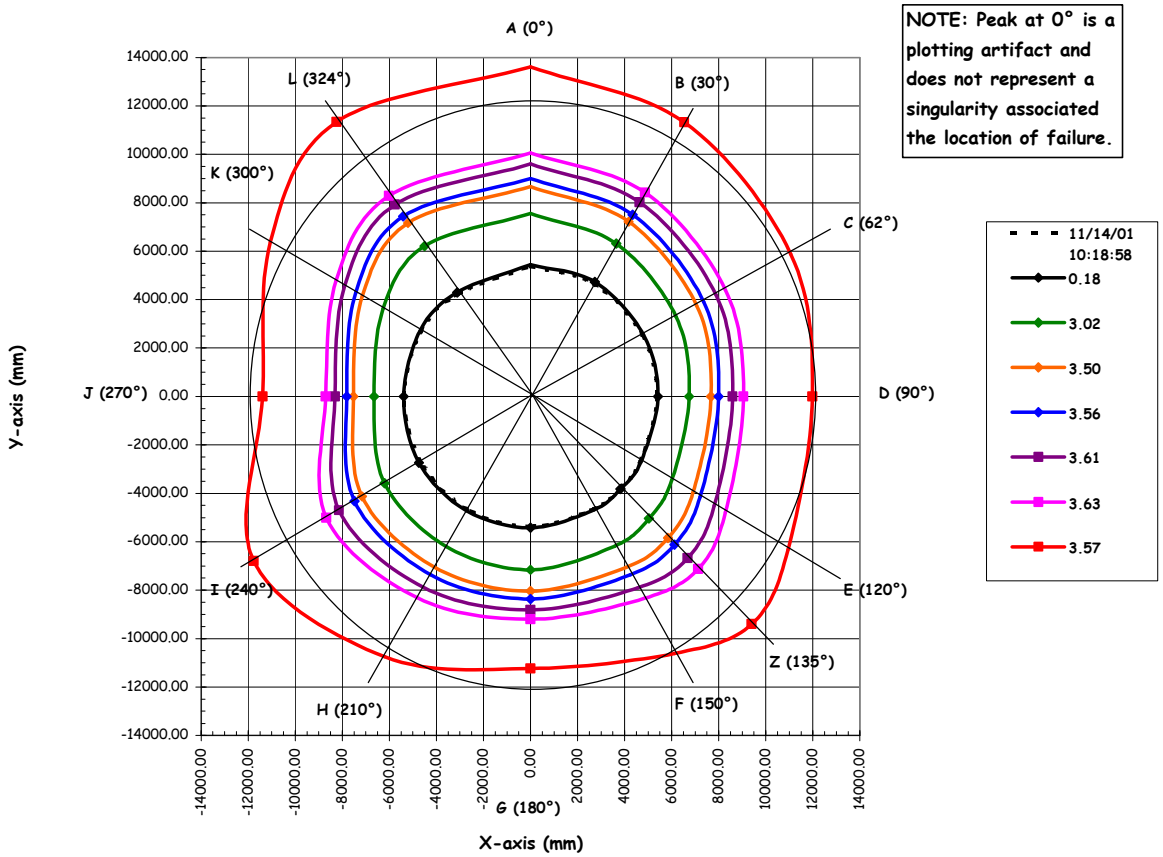

Figure 5.100 SFMT - Deformation at Elev. 4680 (5) × 100 – 3.0P_d to 3.63P_d

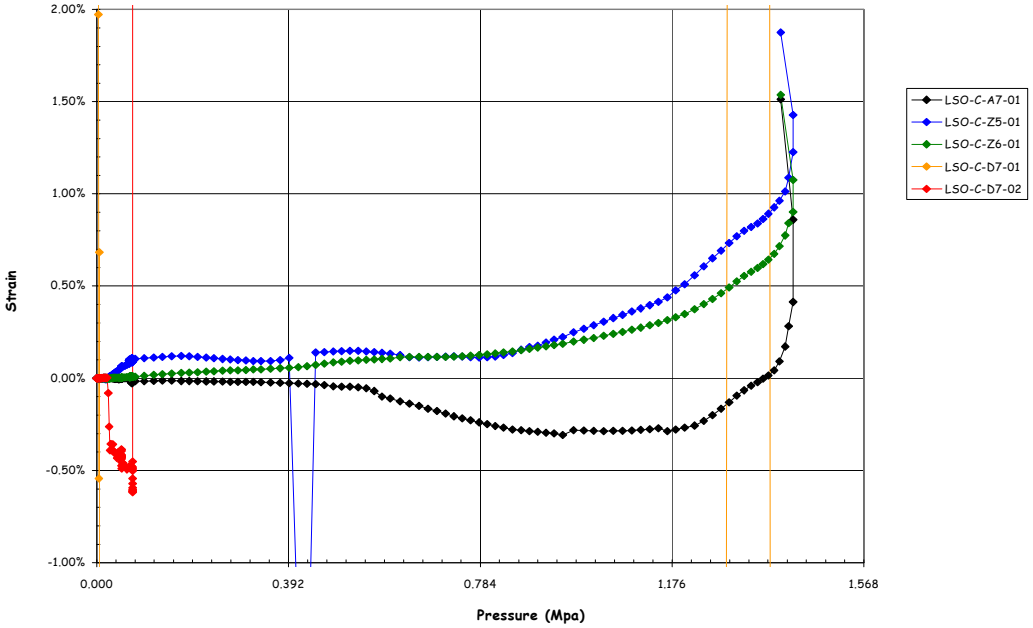

Figure 5.101 SFMT Exterior Liner Strains

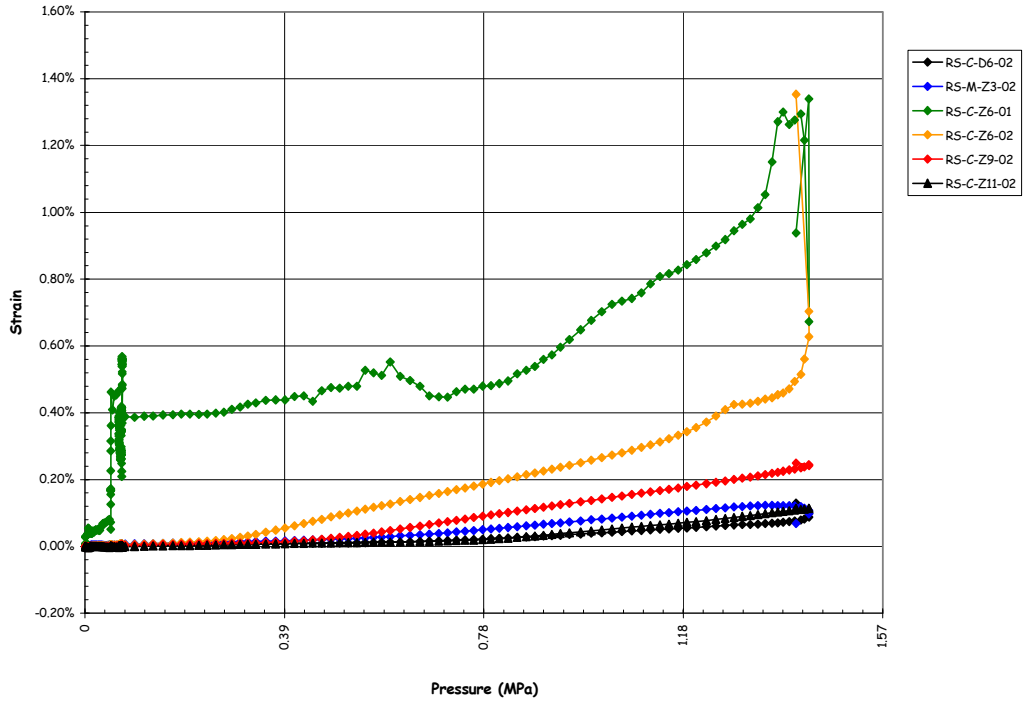

Figure 5.102 SFMT – Free-Field Hoop Rebar Strains

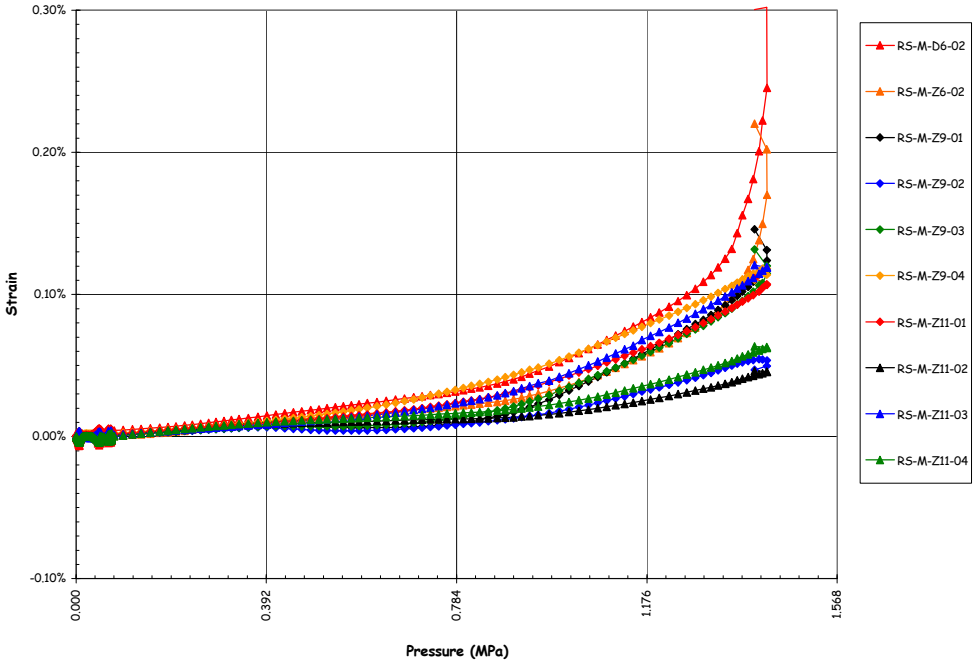

Figure 5.103 SFMT – Free-Field Meridional Rebar Strains

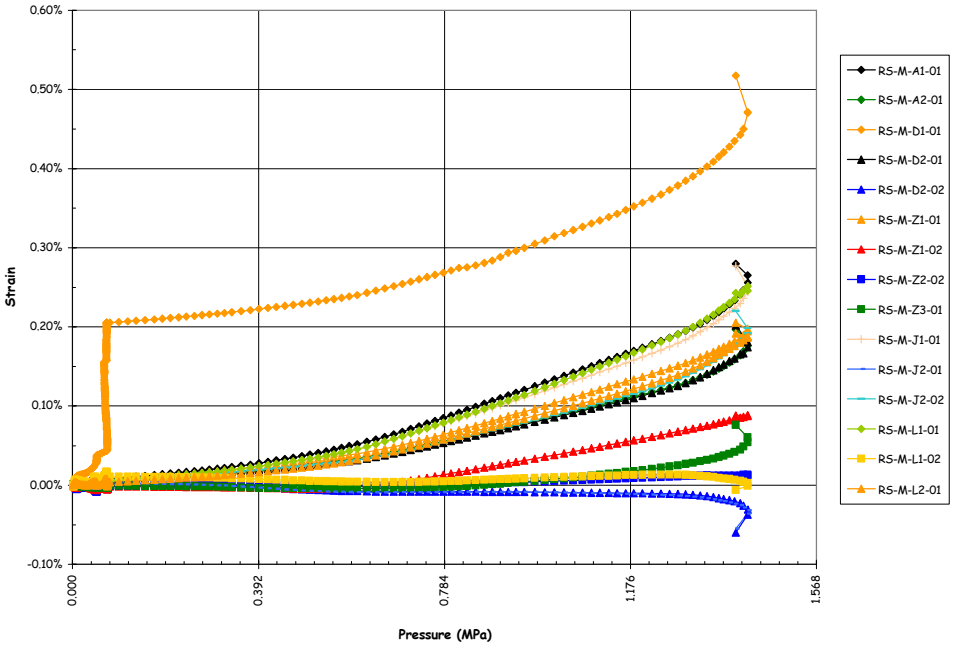

Figure 5.104 SFMT – Meridional Rebar Strains at Wall-Base Junction

Concrete strains, measured by the surviving SOFO fiber-optic gages, are plotted in Figure 5.105. The maximum hoop strain in the concrete, 1.1% (CE-C-Z6-01) at the mid-height of the cylinder, is a little lower than the displacement-based or rebar strains, but overall the concrete strains are consistent with the other measurements.

5.3.3.1.4 Tendon Forces and Strains

All the tendon load cells and strain gages that survived the LST were still functioning at the start of the SFMT and all were monitored during the test. Several load cells and tendon strain gages failed after filling the PCCV with water or early during the SFMT, presumably due to water leaks from the model damaging the gage or shorting out the wiring. The data for all the gages that were functioning at the start of the test are provided, however.

Figures 5.106 and 5.107 show the anchor forces for the instrumented tendons during the SFMT. These anchor forces are representative examples of all the tendon anchors. With the exception of one anchor on H53, the hoop tendon anchor forces increase to nearly 600 kN, which is close to the breaking strength of straight tendons in laboratory tests. It is reasonable to expect that the breaking strength of the curved tendons under field conditions would be lower than the laboratory breaking strength. Load cell TL-C-J6-01 on H53 exhibits an artificially high force near the beginning of the SFMT, most likely from moisture affecting the gage. However, the increased force due to pressure tracks very closely with the other load cells. The vertical tendon anchor forces do not show as large an increase, and the average maximum force only approaches 500 kN, well below the breaking strength. This is consistent with response during the LST and the observation that the vertical tendons did not fail prior to the rupture of the model.

Near the end of the test, sudden decreases in load were observed for several hoop tendon load cells and interpreted as individual strand wires breaking. After reaching the peak pressure, all the load cell readings dropped sharply as the tendons and the model ruptured.

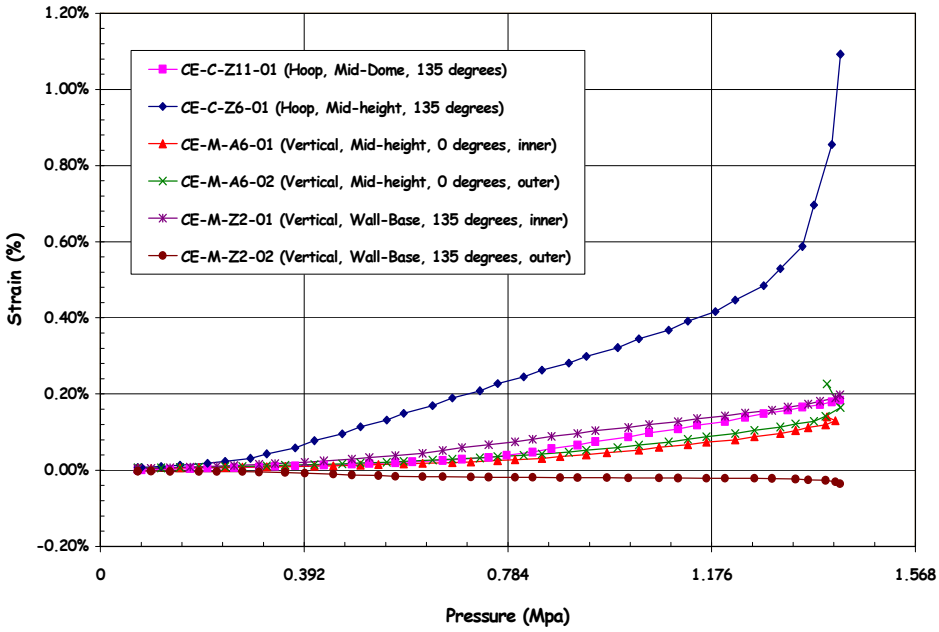

Figure 5.105 SFMT – Concrete (SOFO) Strains

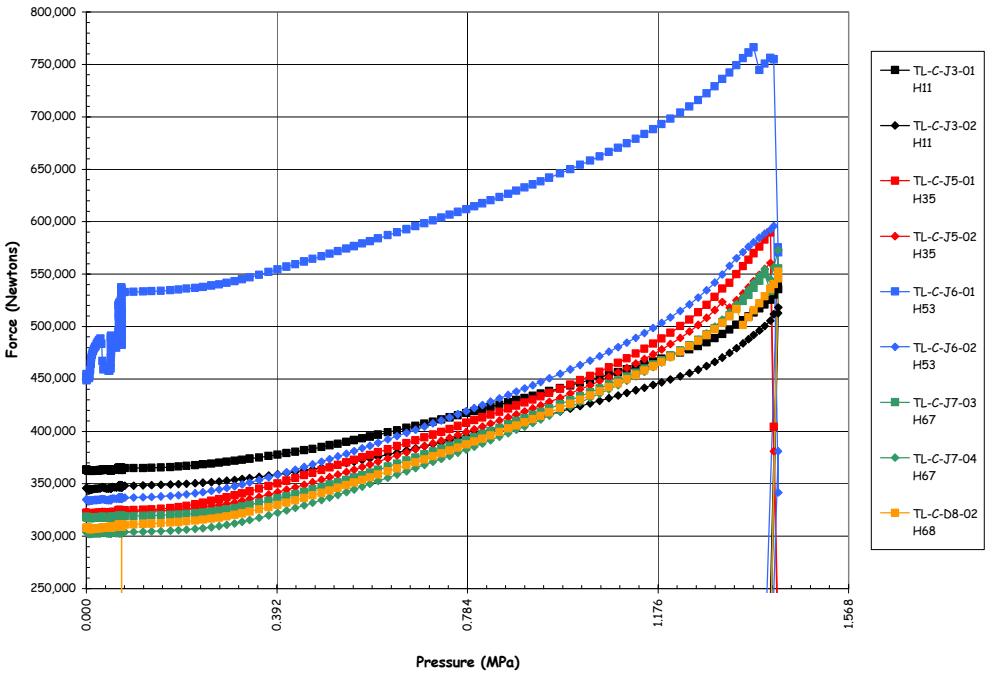

Figure 5.106 SFMT – Instrumented Hoop Tendon Anchor Forces

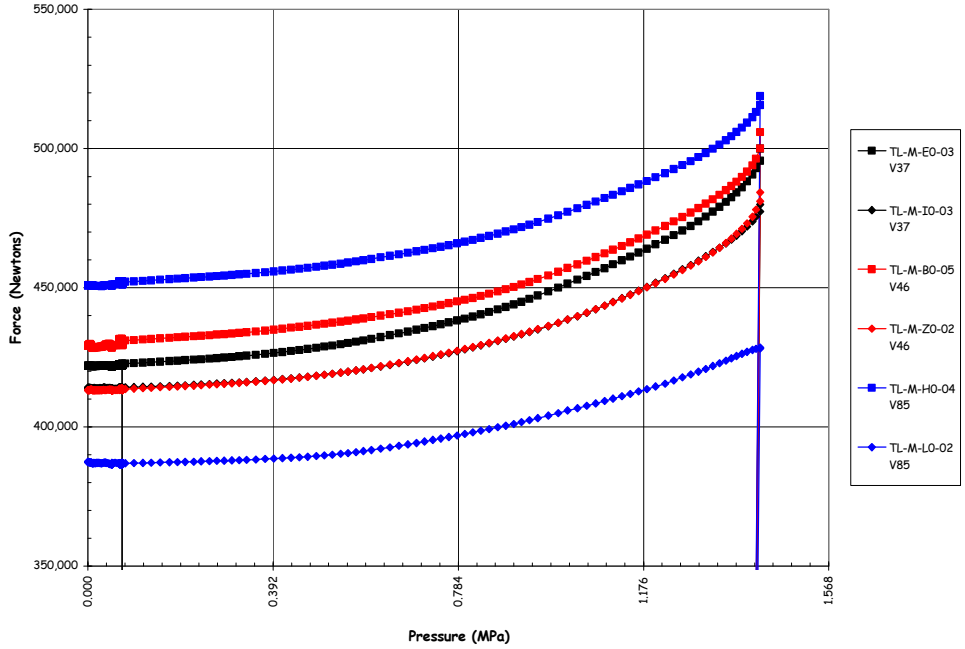

Figure 5.107 SFMT – Instrumented Vertical Tendon Anchor Forces

Tendon strains were also recorded using the surviving foil gages mounted on individual strand wires. Figures 5.108 and 5.109 show the strains for hoop tendons H53 and H68, and Figure 5.110 shows the strains for vertical tendon V46. These results are typical of the other instrumented tendons, although the magnitude of the strains vary. Since the strain gages were 're-zeroed' before the SFMT, only the strain due to pressure is plotted. The total tendon strain is the measured strain plus the residual prestressing strain, typically on the order of 0.4% for the hoop tendons and 0.6% for the vertical tendons. The hoop tendon strains at maximum pressure were therefore on the order of 1.0%, 0.4% due to prestressing plus 0.6% due to the maximum pressure of $3.65P_d$. Similarly, the maximum hoop tendon strain measure prior to rupture is on the order of 1.4% to 1.5%. There may be some local strain concentrations that were not captured by the strain gages, but this limiting tendon strain is significantly less than the ultimate strain obtained from laboratory tests of a straight tendon sample, typically on the order of 4% for the tendon and 7% for individual strains. Furthermore, none of the model tendons ruptured at the anchors where strain concentrations might be expected, but all ruptured where the deformation of the model was greatest, approximately azimuth 6 degrees.

Similarly, the strain in the vertical tendons at the maximum pressure are on the order of 0.1 to 0.2%, and the total strain is on the order of 0.7% to 0.8%. Both are well below the strain at which the hoop tendons were believed to have ruptured, reinforcing the belief that the vertical tendons did not fail prior to the rupture of the vessel.

The tendon force profiles, previously constructed for prestressing and the LST, were also constructed for the SFMT. Since the tendon strains were re-zeroed for the SFMT, it was assumed that the residual strain for each gage after the LST was the initial strain at the start of the SFMT. These residual strain values were added to the SFMT strain data and the force distribution profiles were constructed in the same manner as before. Figures 5.111 to 5.115 show the force profiles for the five instrumented hoop tendons.

One point deserves mentioning. The tendon anchor forces appear to drop off at or just beyond the peak pressure. This is an artifact of rupture occurring during a data scan. The pressure and strain values were recorded near the beginning of the scan, while the load cells were among the last instruments scanned. If rupture, which occurred in a few seconds, took place during the 30 second data scan, the DAS would associate the pressure before rupture with the load cell reading after rupture, giving the appearance that the tendon anchor forces dropped before the model ruptured.

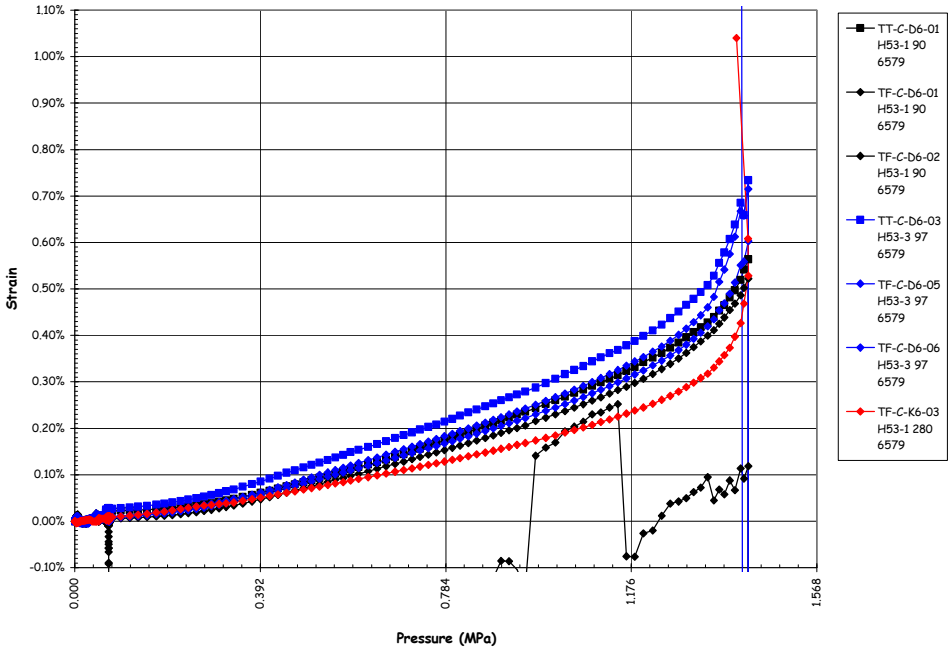

Figure 5.108 SFMT – Tendon H53 Strains

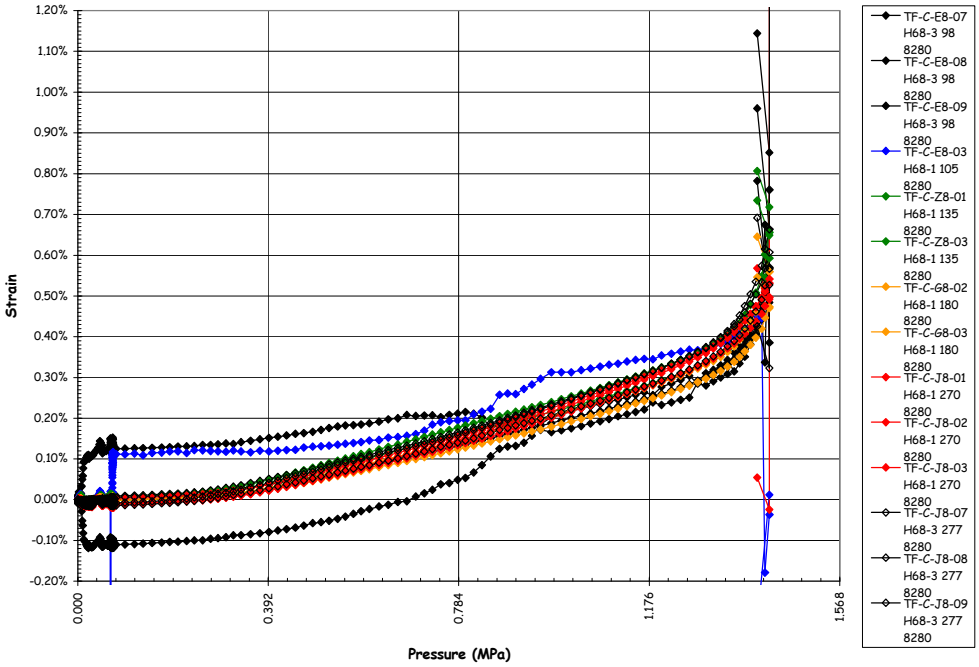

Figure 5.109 SFMT – Tendon H68 Strain

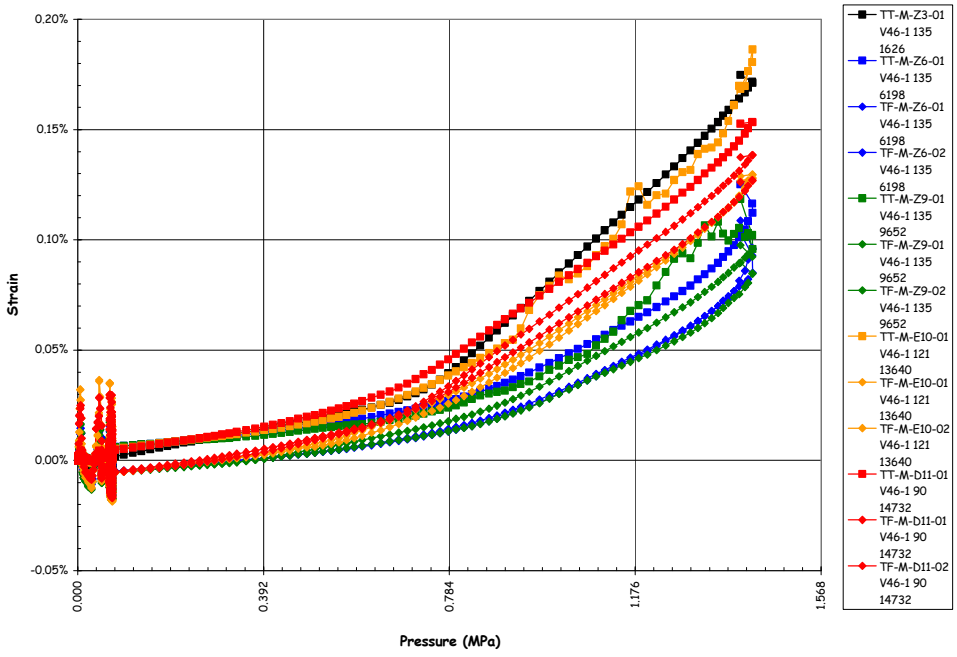

Figure 5.110 SFMT – Tendon V46 Strains

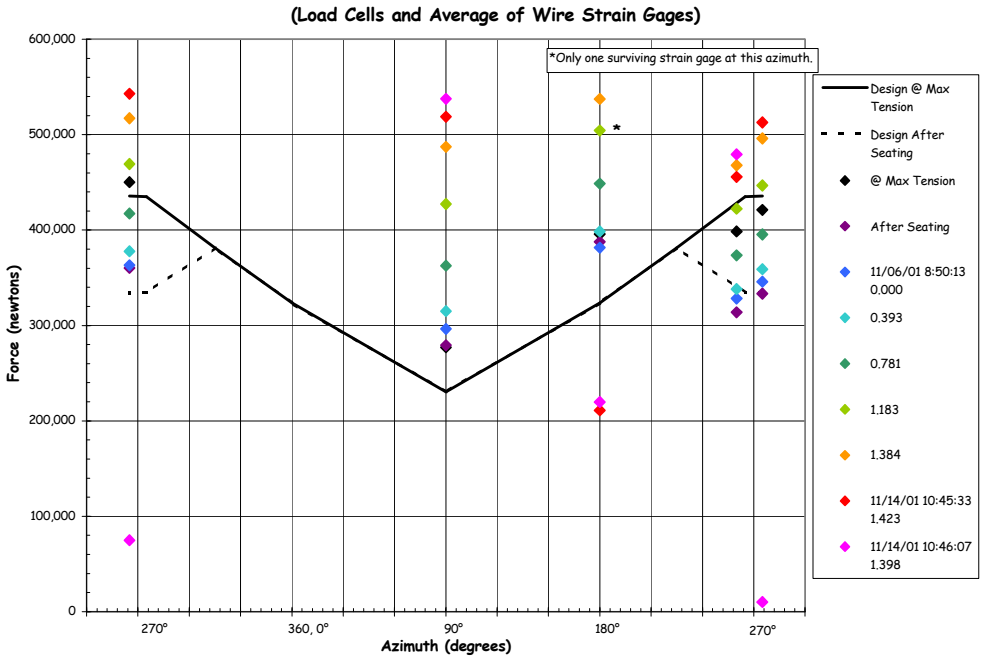

Figure 5.111 SFMT – Tendon H11 Force Distribution (Elev. 1854)

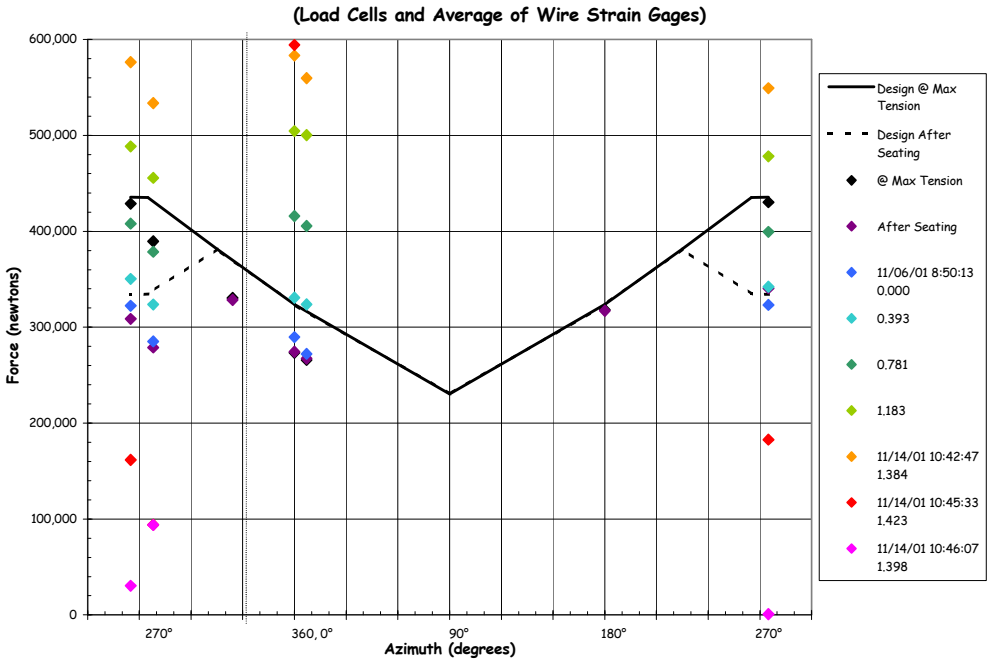

Figure 5.112 SFMT - Tendon H35 Force Distibution (Elev. 4572)

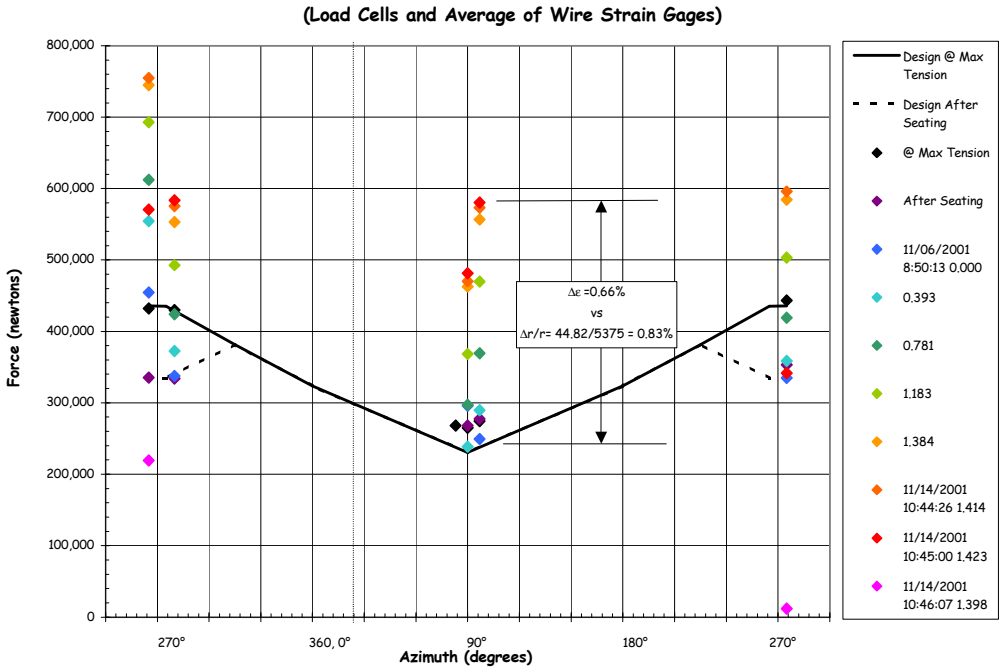

Figure 5.113 SFMT - Tendon H53 Force Distribution (Elev. 6579)

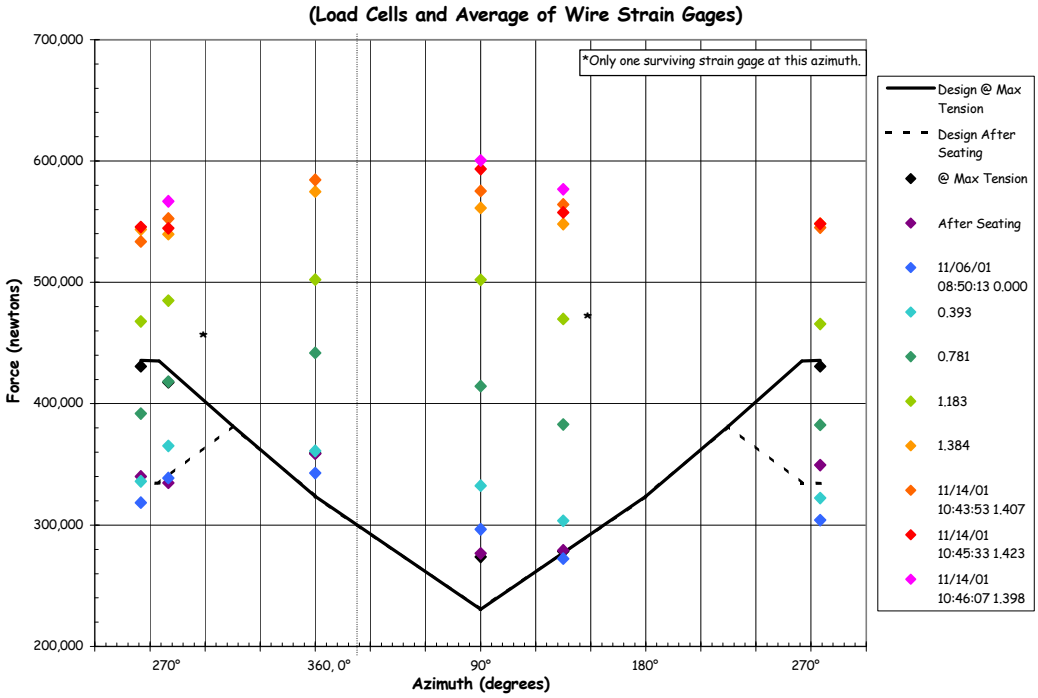

Figure 5.114 SFMT - Tendon H67 Force Distribution (Elev. 8153)

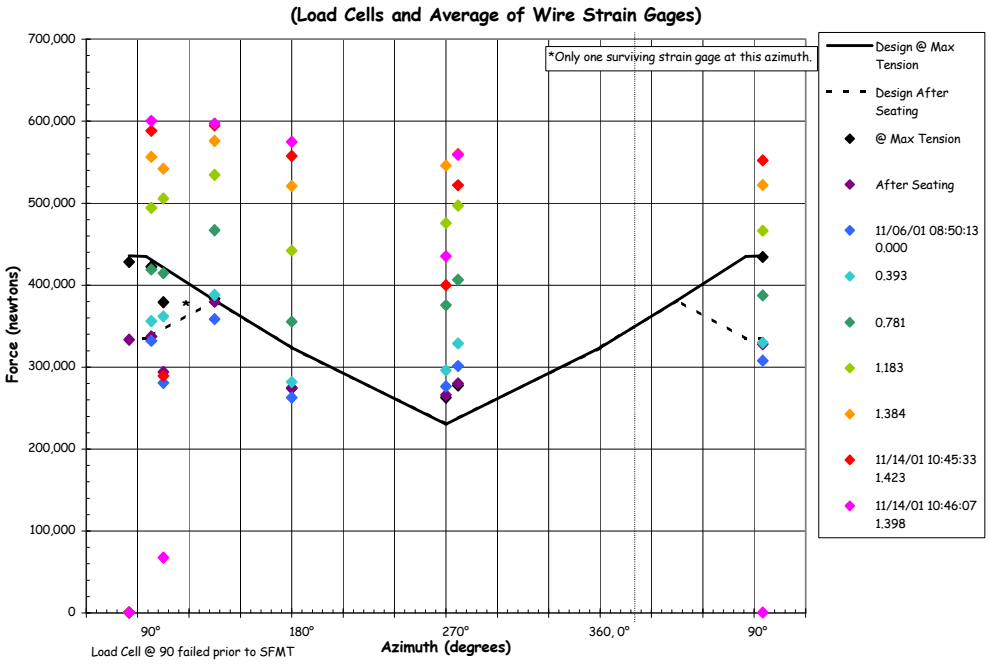

Figure 5.115 SFMT - Tendon H68 Force Distribution (Elev. 8280)

Again, the data is not adequate to assume the shape of the hoop tendon force profile between the surviving measurement positions, and only the force at the measurement locations are plotted, with no attempt to interpolate the strain between the measurement locations. As the pressure is increased, however, and generalized yielding of the model and the tendons occurs, all the plots indicate that the tendon force becomes more uniform along the length, approaching a limiting value of approximately 600 kN (135 kips). One unresolved issue is whether the tendon force equilibrates by slipping relative to the sheath or if the friction is high enough to effectively bond the tendon to the concrete.

An attempt was made to determine this by calculating the local, displacement-based strain in the wall and, assuming the tendon behaved as if bonded, adding it to the initial prestressing strains and computing the force profile from these strains. Figure 5.116 compares the force distribution obtained in this manner with the forces based on the tendon strain measurements for tendon H35 near elev. 4680 where the displacements were measured. The results compare favorably and seem to reinforce the idea that the tendons behave as if they were bonded after prestressing. While this is a compelling argument, it must also be admitted that these results are not entirely conclusive and further tests may be required to resolve this issue.

Figures 5.117 to 5.119 show the force profiles for the instrumented vertical tendons. Again, as was observed with the response during the LST, the force profile appears to become more uniform with pressure. Since the vertical tendons do not yield, tendons must slip relative to the sheath or concrete wall, even in the dome where the tendons are curved. This counters the observation made for the hoop tendons that the tendons behave as if they were bonded to the concrete. No explanation for this apparent inconsistency has been proposed, reiterating the need for further investigation of this behavior, including additional testing.

5.3.3.1.5 Acoustic Response

The acoustic monitoring system used during the LST was also employed for the SFMT, minus the interior sensors, which were removed to install elastomeric liner. Since the SFMT was not focused on detecting liner tearing/leaks, this was not a significant compromise. The focus of the acoustic system during the SFMT was to detect tendon wire breaks and any other events that might indicate structural damage. The acoustic monitoring system was put into operation at the same time the main DAS was started, prior to filling the vessel with water. (As noted in Section 5.2, it was also employed during the pneumatic leak check of the elastomeric liner.)

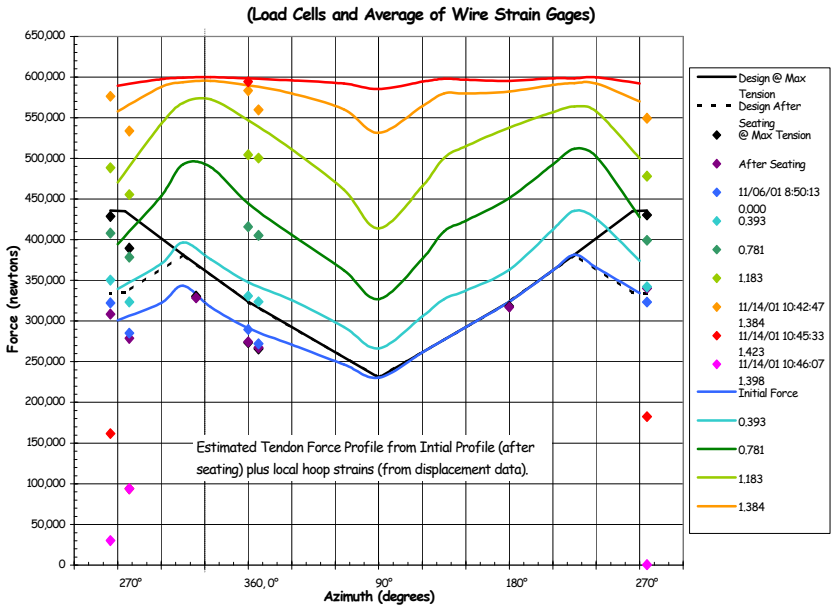

Figure 5.116 SFMT – Tendon H35 Computed and Measured Force Distribution

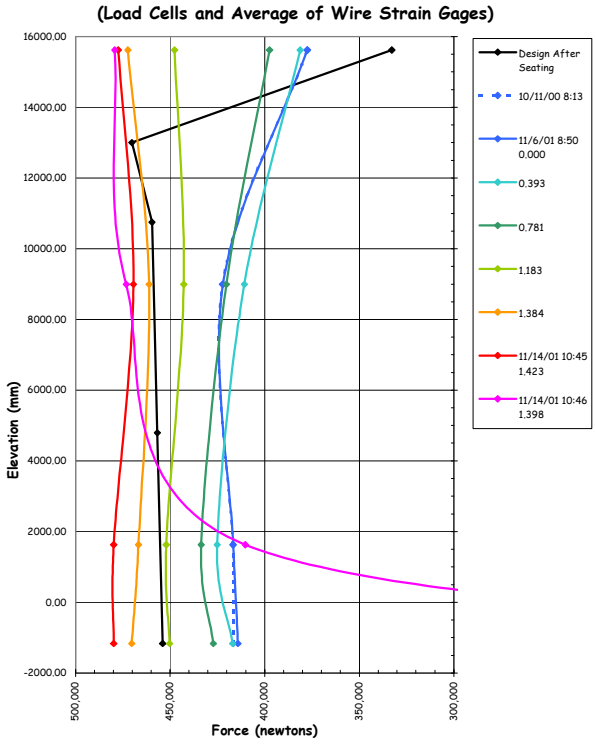

Figure 5.117 SFMT - Tendon V37 Force Distribution at Azimuth 240 Degrees

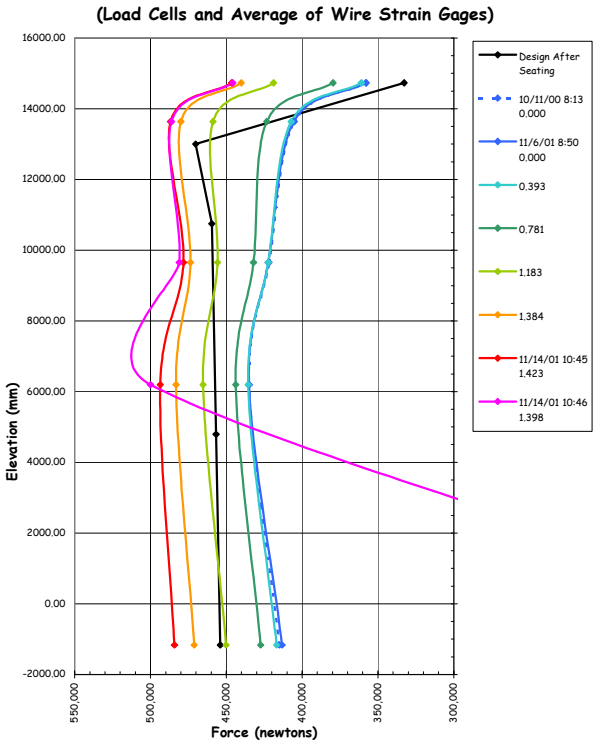

Figure 5.118 SFMT - Tendon V46 Force Distribution at Azimuth 135 Degrees

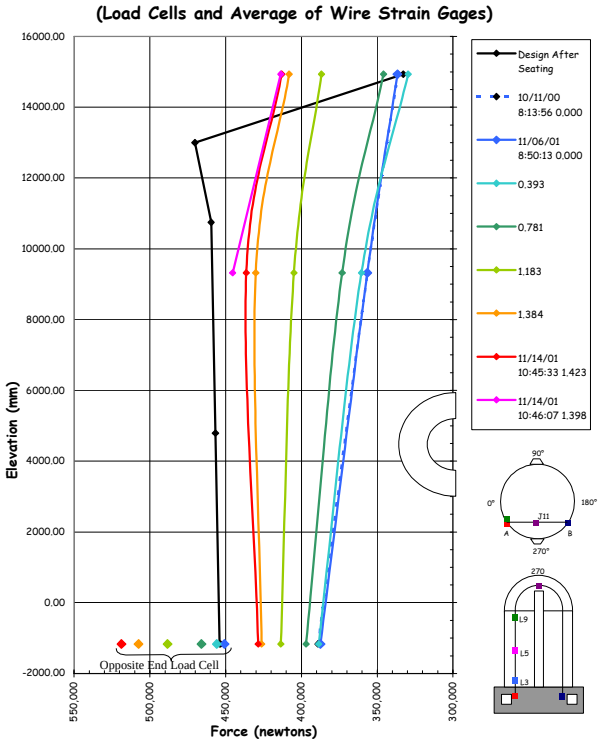

Figure 5.119 SFMT - Tendon V85 Force Distribution at Azimuth 325 Degrees

The post-SFMT reports from Pure Technologies are included in Appendix K. The acoustic event data is also included with the SFMT response data files in Appendix I (data CD). Along with a .wav file of the combined acoustic output during the final minute leading up to, and including, the rupture of the PCCV model. In addition to background noise associated with leaking, deformation, and microcracking of the model, the system identified distinct acoustic events which were categorized as concrete cracking, tendon gallery events, tendon pings, and tendon wire breaks.

Only 27 distinct concrete cracking events were recorded during the SFMT prior to rupture, continuing the trend observed during the LST, i.e., the bulk of the concrete cracking events occurred between 1.0 and $2.3P_d$. The tendon pings were confined to the vertical buttresses and the tendon gallery, as during the LST, suggesting the tendons and anchors continued to readjust or reseat themselves. Since all the tendon pings occurred during the final minutes of the SFMT (10:39:30 to 10 45:26), it may also suggest some slipping at the anchors.

The tendon gallery events were all limited to the tendon gallery between 10:43:37 and 10:46:03, implying something occurred with the vertical tendons. The acoustic characteristic of these events is different from the tendon pings and suggested a different mechanism. However, no physical explanation for these events was offered or identified during posttest inspection or demolition of the model.

Fifty-seven actual or probable wire break events were identified between 10:39:47 and rupture of the model at 10:46:12. The wire-break event locations are mapped in Figure 5.120.

Other than observing the discontinuities in the tendon load cell and strain time histories that might indicate a wire break, there were no other efforts to correlate the probable wire breaks identified by the acoustic system with the other test data. While it is arguable that the probable wire break events were actual wire breaks, at least a dozen or so were confirmed by the visual records. Figure 5.121 plots the time history of all the acoustic events along with the effective pressure time history. It is readily apparent that the frequency and magnitude of the wire break events increases just prior to rupture.

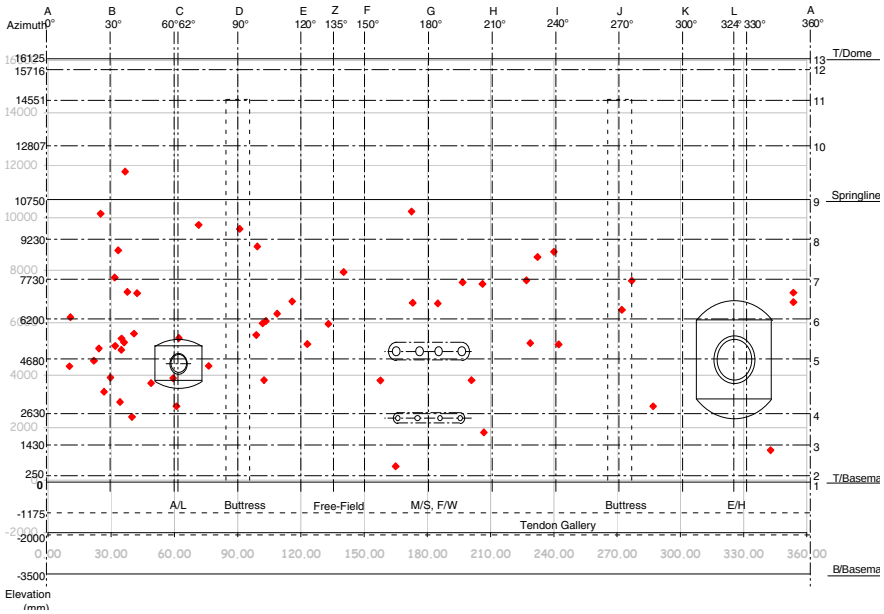

Figure 5.120 SFMT – Wire Break Map

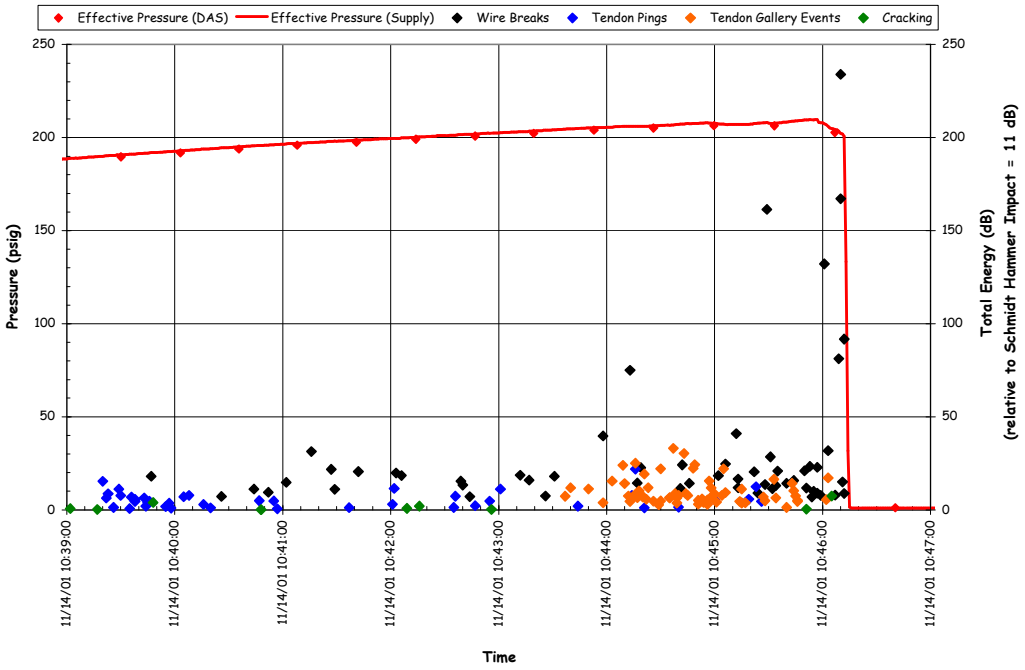

Figure 5.121 SFMT – Acoustic Event and Pressure Time History

5.3.3.1.6 Video

Due to the dynamic nature of the PCCV model rupture at the end of the SFMT, the video images were a valuable diagnostic resource for understanding the failure sequence. Four exterior digital video cameras at 0 degrees, 90 degrees, 180 degrees, and 270 degrees and two interior video cameras at the E/H and at the top of the dome monitored the model throughout the SFMT. Viewing the images in slow motion revealed that the model rupture began at the mid-height of the cylinder at approximately 6 degrees azimuth. The rupture propagated vertically in both directions until it reached a point approximately 2 m above the top of the basemat. The cylinder wall then began to open up, shearing itself from the basemat circumferentially in both directions, and meeting on the back side at 180 degrees. The vessel then 'telescoped' over the stem of the cylinder wall before coming to rest on the instrumentation frame.

The interior view of the E/H was distorted by the water and the resulting images were not useful. However, the camera in the dome showed the water surface dropping just prior to the rupture of the vessel, which was captured by all four external video cameras. A video file (.mpg) showing the PCCV model during the final minute of the SFMT and posttest images is included on the data CD in Appendix I. This video includes the acoustic system recording synchronized with the visual images. From close inspection of the video file, visible event times were documented in Table 5.6. The same event may have been observed at slightly different times depending on the camera viewing the event.

5.3.3.2 Posttest Inspection

Since the model was severely damaged and unstable, inspection after the SFMT was limited to an exterior survey. The exterior surface was photographed and the debris field was roughly mapped to document the model fragment locations.

The rupture lines are roughly mapped in Figure 5.122. This figure shows the approximate location of major vertical and horizontal rupture lines along with secondary tears at the E/H and adjacent to the main vertical rupture. These secondary tears are most likely associated with previous liner tears and/or cutouts.

The hoop rebar and tendons along the main rupture line were also inspected for evidence of any discontinuity or other defects that may have accounted for the location of rupture. The close-up photographs of the rebar and tendon strands in Figure 5.123 clearly show 'necking' of the bars and wires, indicating that they failed in a ductile manner with large local strains occurring before failure. These photographs are typical of all the tendons and bars at the rupture. The hoop

Table 5.6 SFMT Video Event Times

Time	0° Camera	90° Camera	180° Camera	270° Camera
hour:min:sec:1/30th sec (Video camera speed: 30 frames/second)				
10:45:55:28		H40 wedge ejected, strand broken		
10:45:56:01			H40 wedge ejected, strand broken(?)	
10:45:56:15		Something begins falling @ 100°, El. 5000 toward 5 o'clock		
10:45:56:26	Concrete spall above E/H			
10:45:57:00				Concrete spall (?) @ E/H
10:46:01:24		H42 wedges ejected, strand broken	H42 wedge ejected, strand broken	
10:46:03:10	Water stream starts @ 30°			
10:46:09:09		H64 strand broken/ejected		
10:46:09:12			H64 strand ejected	
10:46:11:21		Spurt of water(?) from H48 anchor		
10:46:11:26	H37 strand ejected			H37 strand ejected
10:46:12:00	Rupture initiated @ 6° (Collapse over in less than 2 seconds)			
10:46:12:01			H40 second strand ejected H37 strand ejected	Rupture
10:46:12:06			Rupture, multiple strands ejected	

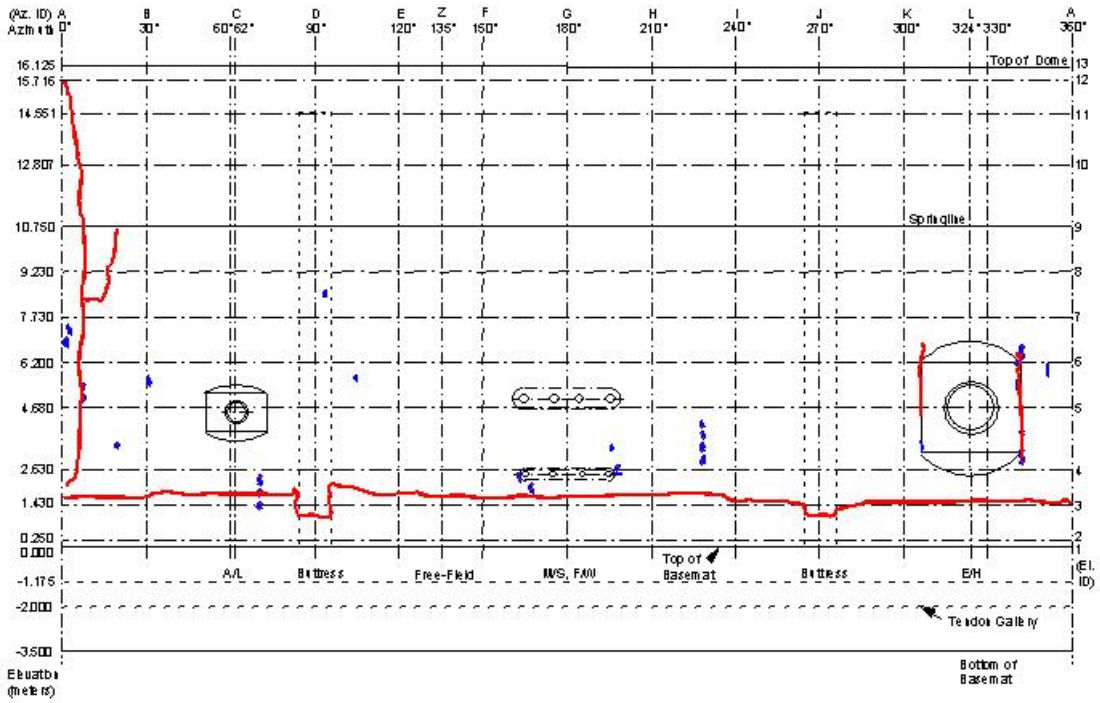

Figure 5.122 SFMT – Rupture Map

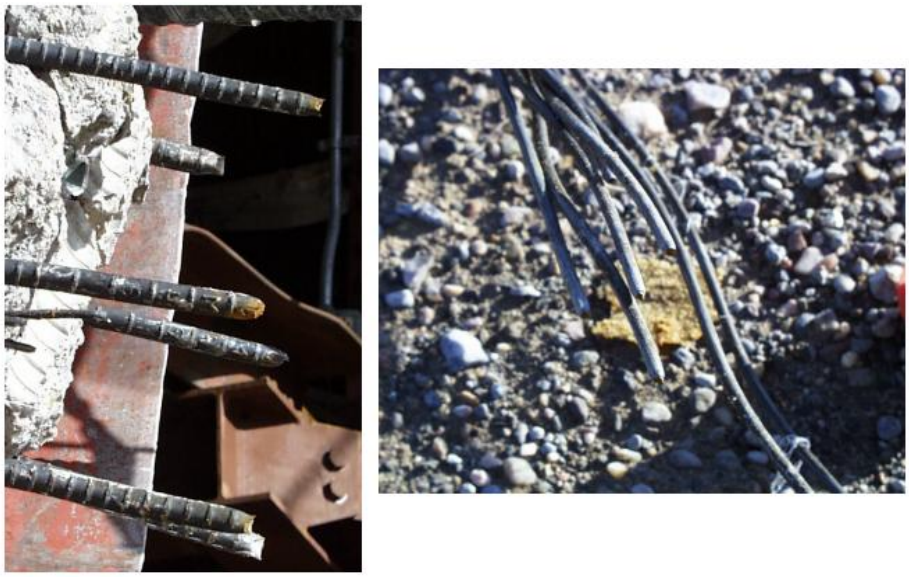

Figure 5.123 SFMT – Rebar and Tendon Strands at the Rupture Line

bars were spliced mechanically very near the rupture, but there was no evidence that any of the mechanical splices failed or that these in any way biased the location where failure began.

The position of the model after the SFMT was also noted. Figure 5.124 shows that the model displaced approximately 3" horizontally and tipped in the opposite direction of the rupture. Six tendons were completely ejected from the model and the final location of major pieces of debris were mapped on the site plan, as shown in Figure 5.125. The location of the debris was not only due to the initial rupture, but also by the flow of 350,000 gallons of water escaping from the model.

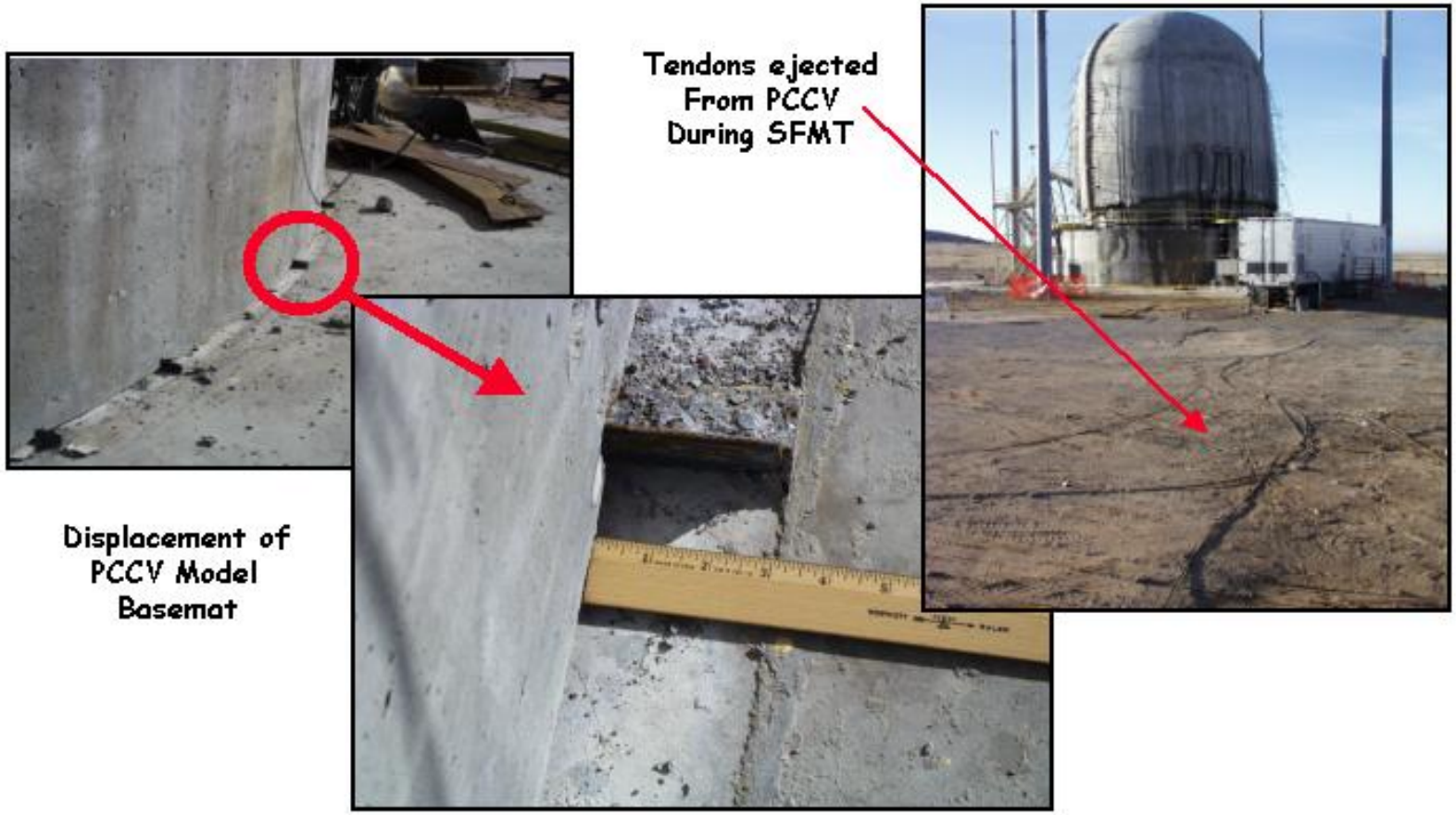

Figure 5.124 SFMT – Model Displacements

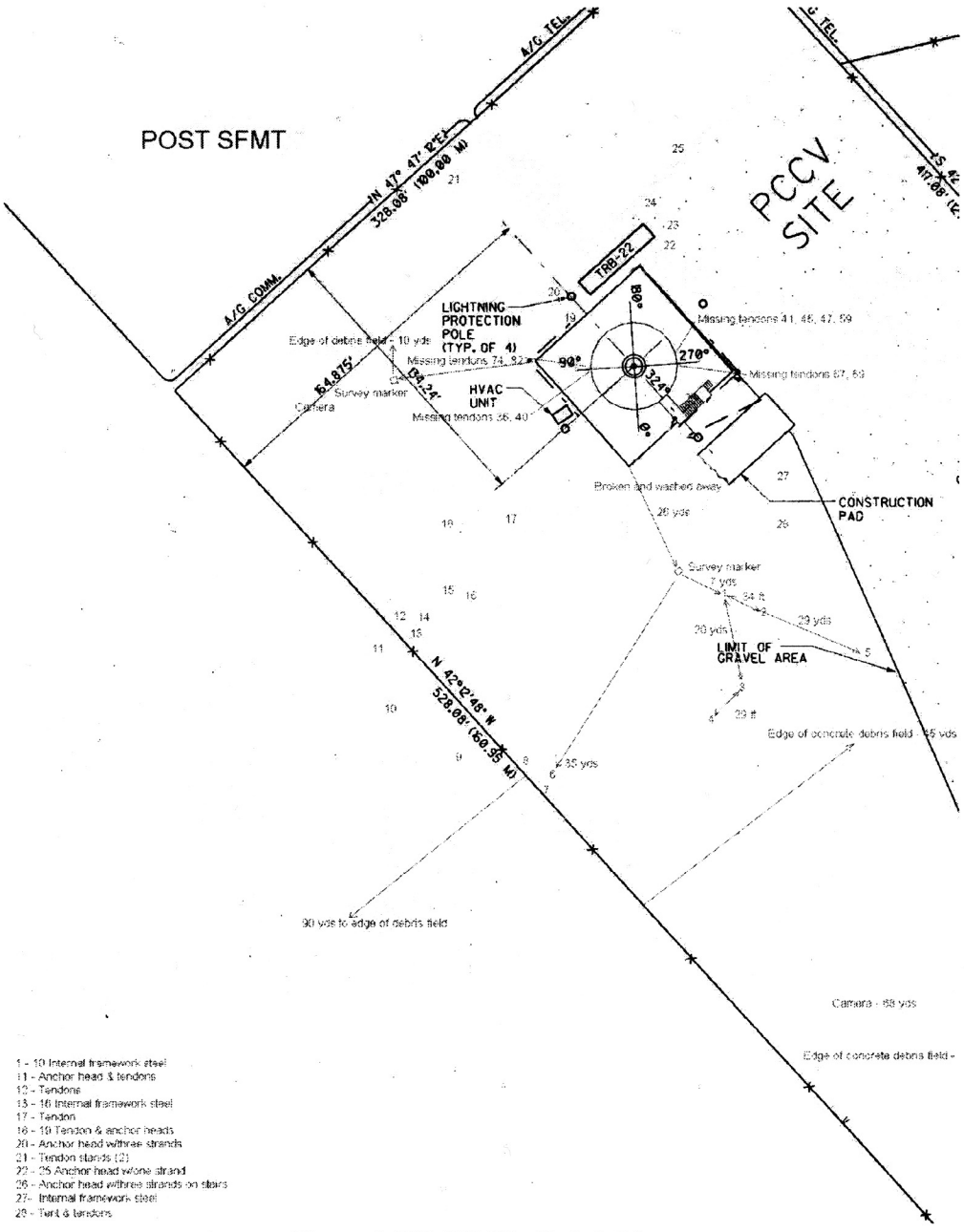

Figure 5.125 SFMT – Debris Map